A NUMERICAL STUDY OF FUNDAMENTAL SHOCK NOISE MECHANISMS

A Dissertation

Presented to the Faculty of the Graduate School

of Cornell University

in Partial Fulfillment of the Requirements for the Degree of

Doctor of Philosophy

by

Kristine R. Meadows

May 1995

A NUMERICAL STUDY OF FUNDAMENTAL SHOCK NOISE MECHANISMS

Kristine R. Meadows, Ph.D.

Cornell University 1995

The results of this thesis demonstrate that direct numerical simulation can predict sound generation in unsteady aerodynamic flows containing shock waves. Shock waves can be significant sources of sound in high speed jet flows, on helicopter blades, and in supersonic combustion inlets. Direct computation of sound permits the prediction of noise levels in the preliminary design stage and can be used as a tool to focus experimental studies, thereby reducing cost and increasing the probability of a successfully quiet product in less time.

Direct simulation of sound generation in shocked flows is challenging because of the disparity in amplitude between the acoustic waves and shocks. These challenges are met by the implementation of a high-order accurate Essentially Non-Oscillatory (ENO) scheme which maintains high accuracy in smooth regions of the flow to minimize numerical dissipation of the acoustic waves while maintaining sufficient numerical dissipation at the shock for stability.

This thesis reveals and investigates two mechanisms fundamental to sound generation by shocked flows: shock motion and shock deformation. Shock motion is modeled by the interaction of a sound wave with a shock. During the interaction,

the shock wave begins to move and the sound pressure is amplified as the wave passes through the shock. The numerical approach presented in this thesis is validated by the comparison of results obtained in a quasi-one dimensional simulation with linear theory. Analysis of the perturbation energy demonstrated for the first time that acoustic energy is generated by the interaction.

Shock deformation is investigated by the numerical simulation of a ring vortex interacting with a shock. This interaction models the passage of turbulent structures through the shock wave. The simulation demonstrates that both acoustic waves and contact surfaces are generated downstream during the interaction. Analysis demonstrates that the acoustic wave spreads cylindrically, that the sound intensity is highly directional, and that the sound pressure level increases significantly with increasing shock strength. The effect of shock strength on sound pressure level is consistent with experimental observations of shock noise, indicating that the interaction of a ring vortex with a shock wave correctly models a dominant mechanism of shock noise generation.

Biographical Sketch

Kristine Reuter Meadows received her Bachelor of Science in Mechanical Engineering and Mechanics from Old Dominion University in May, 1985, and was honored with awards from both the Mechanical Engineering Department and the School of Engineering for Academic Excellence.

After graduation, she worked in Advanced Submarine Design Concepts and Acoustics at Newport News Shipbuilding and Drydock Company where she designed an external countermeasure launcher system, specialized in sonar and array systems, and pursued graduate study in the evening.

In January 1988 she began her research career in aeroacoustics at NASA Langley Research Center, and began to pursue a Master's program in earnest. She completed the Master of Science in Engineering, with an emphasis in Aeroacoustics, from The George Washington University in May of 1990.

In August 1990, she began doctoral studies in Aerospace Engineering at Cornell University. She finished her course work in December of 1991, and returned to NASA Langley to conduct her research.

To date, Kristine Reuter Meadows has authored or co-authored twelve journal articles and conference papers in the field of acoustics. She has given an invited lecture on computational aeroacoustics.

It is good to have an end to a journey;

but it is the journey that matters, in the end.

- Ursula L. LeGuin

Acknowledgements

I would like to acknowledge NASA Langley Research Center for providing the opportunity for me to pursue doctoral studies at an outstanding institution. Special appreciation is extended to Dr. Jim Thomas, head of the Aerodynamics and Acoustics Methods Branch, and Jack Preisser, head of the Aeroacoustics Branch, for their support in this endeavor.

I am pleased to specifically acknowledge several exemplary individuals for their technical contributions to this research. Professor Dave Caughey supervised this research and provided innumerable suggestions and comments. His technical insights and willingness to supervise this work long distance are greatly appreciated. Dr. Jay Hardin served as my mentor at Langley and graciously provided technical advice in aeroacoustics, mathematics and time series analysis. Dr. Jack Seiner provided many insightful discussions on the topic of jet noise. Dr. Jay Casper acquainted me with his finite-volume implementation of the essentially non-oscillatory (ENO) scheme. Dr. Feri Farassat introduced me to generalized functions and reviewed the analysis herein. Professor Al George and Professor Sid Leibovich reviewed this thesis and served on my committee.

Table of Contents

List of Tables

List of Figures

Chapter 1

Introduction

The motivation behind this research is to establish a better understanding of the physical nature of sound generation in shocked flows. Knowledge gained by increased understanding of the primary mechanisms involved in shock noise generation has application to a variety of real aerodynamic problems. In helicopter and tilt-rotor applications, shock waves may form on the blade surfaces, and vortices from a preceding blade may interact with the shock resulting in impulsive noise. In supersonic engine inlets, combustion instabilities may result in shock oscillation leading to what is commonly known as "buzz". Even subsonic transport aircraft often operate at conditions where the flow over the wing is transonic, and unsteadiness in the flow over the wing can cause the shock to oscillate and generate noise.

The primary application in mind during the course of this research is the sound generation in supersonic jets. When jet engines operate at supercritical nozzle pressure ratios, shocks may form in the jet plume and turbulence interacting with the shock waves generates high amplitude, broad-band noise, typically known as

"broadband shock noise" or "shock-associated noise". The expected shock noise during the climb-to-cruise operating condition of a supersonic civil transport may ruin its chance of ever being put in production. Shock noise is an important design issue because of the effects on community noise, aircraft interior noise, and structural fatigue.

Research towards the understanding of noise generation in jet flows has been ongoing for over 40 years. Morley [1] in an investigation of sound intensity in the far field of turbulent jets, showed that the sound power is proportional to about the eighth power of the jet velocity. Lighthill [2] in his pioneering work on jet noise theory, provided a theoretical basis for the eighth power law noticed by Morley, and provided the basis for an understanding of other jet noise phenomena such as convective amplification. Lilley [5] provides a nice review of classical jet noise theory and the related experiments. There are two recent review papers specific to noise generation in supersonic jets which summarize significant contributions to the understanding of jet noise. The first, written from an experimentalist's perspective, is the review article by Seiner [3]. The most recent, written from a theoretician's perspective, is the article by Tam [4]. The complicated nature of the supersonic jet flow makes development of a comprehensive theory difficult, and therefore the theories currently available for the prediction of shock noise in jets are largely empirical in nature.

The approach taken in this research is to compute directly the sound generated by shock waves in supersonic jets. Advances in computer hardware resulting in more computational speed, affordable memory, and parallel architectures combined with advances in software resulting in more efficient, accurate algorithms and better

networking have made this type of approach currently feasible for relatively simple, two dimensional problems.

Direct computation of aerodynamically generated sound makes sense because sound is inherently a component of a fluid flow field. Therefore, the basic equations governing sound are the same as those governing fluid flow. For Newtonian fluid flows, these equations are the Navier Stokes equations, or, when viscous effects can be neglected, the Euler equations. As can be seen by Figure 1.1, the acoustic portion of a fluid flow field consists of small perturbations on an inviscid, compressible flow. The generation of sound waves, however, often involves viscous, nonlinear effects. Thus, an advantage of performing a direct simulation of the fully nonlinear equations, as opposed to using traditional acoustic methods which require that information along some surface is provided through another means, (e.g. experiment or a separate computation), is that both the sound generation and propagation are computed in the same analysis.

If current trends in increasing computational capacity continue, it will eventually be possible to simulate directly sound generation in complicated, three-dimensional, unsteady flows of practical interest, such as supersonic jet flow. However, direct computation is currently not feasible for routine study of supersonic jet flow because the flow contains far too many scales to be resolved in a reasonable computation. Therefore, a combined modeling-direct computation approach is taken in this research. First, the complicated flow field of a supersonic jet is broken down into simple "model" problems, chosen to isolate mechanisms which are likely to generate sound. The modeling of the supersonic jet flow is described in Chapter 2. Chapter 2 begins by a description of features characteristic of su-

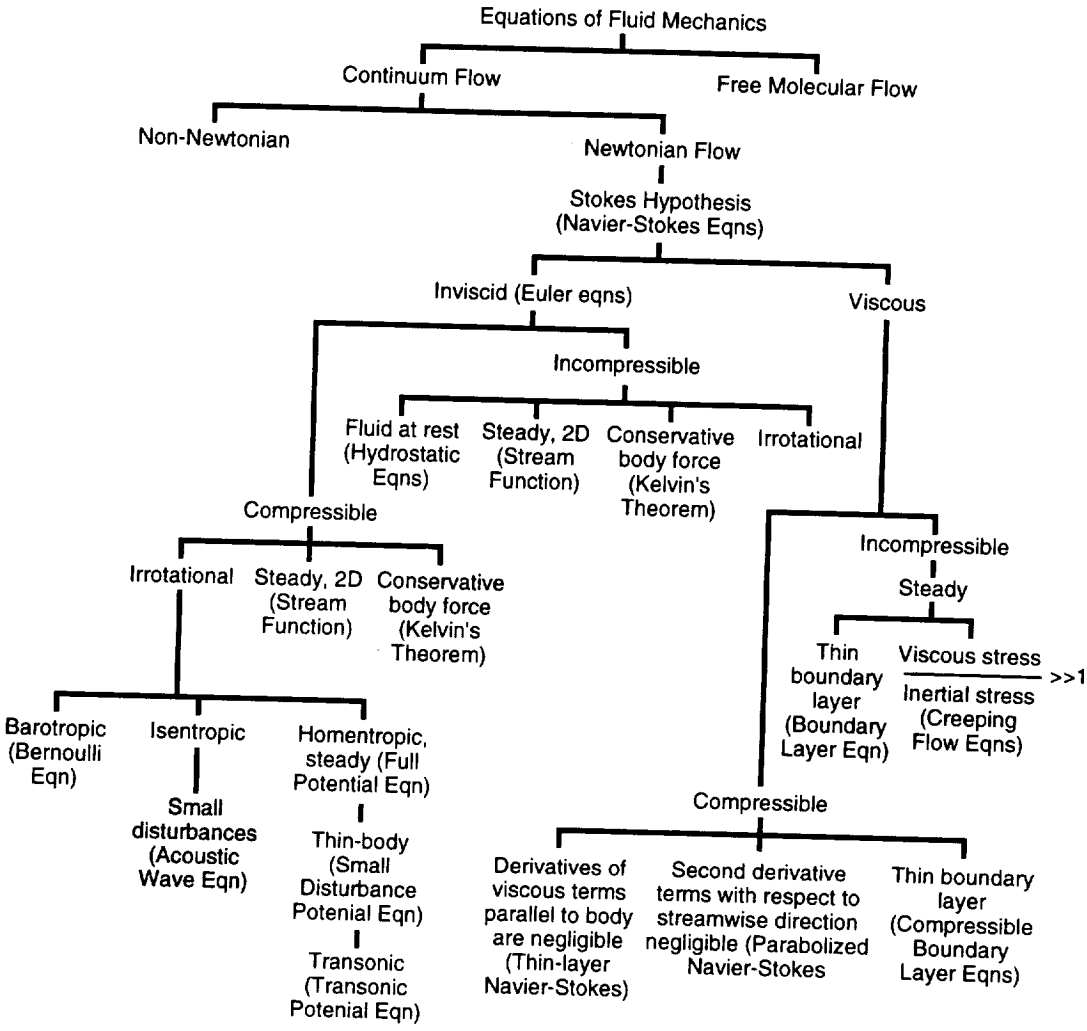

Figure 1.1: Some well-known equations of fluid mechanics. Note that the acoustic wave equation is a special case of the Navier Stokes equations.

personic jet noise and then proceeds to break the complicated flow down into several simpler problems which can currently be solved using reasonable computer resources. Chapter 2 also presents an analytical model for shock noise generation. In this analysis, Lighthill's equation is used to derive the monopole, dipole, and quadrupole source terms associated with an moving planar shock. The source terms are presented and then a Green's function method is used to compute the far field sound associated with each of the source terms. It is found that all of the source terms can potentially contribute significantly to the far field sound.

Chapter 3 addresses numerical issues and methods involved in the computation of flows with moving shocks. Computation of sound generation in shocked flows is challenging because high accuracy is required to maintain the acoustic portion of the solution, while dissipation is required at the shock to maintain stability. Most of the calculations presented in this thesis use a finite-volume implementation of an Essentially Non-Oscillatory (ENO) scheme which provides these important algorithmic features. Because this algorithm is the basis for most of the calculations of this research, and is not currently described in text-books, a brief description is included in this chapter.

Once candidate sound generating mechanisms are identified and modeled, and the numerical methods are in place, the flow for each model problem can be computed and the acoustics extracted from the calculation. The model problems which are addressed in this work are those associated with shock noise generation. Chapter 4 describes the results obtained by an investigation of the first model problem: sound wave-shock wave interaction. Computations of the interaction of a sound wave with a shock wave in a quasi-one dimensional nozzle are presented which

show significant amplification of the sound wave pressure amplitude as a result of the interaction. The increase in amplitude of the acoustic pressure is shown to be a function of the Mach number upstream of the shock. Comparisons with linear theory are made for the small-disturbance calculations which validate the code. Results are also provided for the higher-amplitude cases. In addition, an energy analysis is performed which shows that acoustic energy is generated during sound-shock interaction.

Chapter 5 presents results obtained by the investigation of the interaction of a vortex ring with a shock wave. This sound generating mechanism is more complicated than the plane sound-shock interaction case because the shock bends during the interaction, generating alternating compression-rarefaction-compression-rarefaction regions along the acoustic wave front. Flow parameters downstream of the shock are observed and from these observations the conclusion is drawn that both acoustic waves and contact surfaces result from the interaction. Analysis of the results shows that the acoustic wave spreads cylindrically, that the sound intensity is highly directional, and that the sound pressure level increases significantly with increasing shock strength. The effect of shock strength on sound pressure level is consistent with experimental observations of shock noise, indicating that the interaction of a ring vortex with a shock wave correctly models the physics of shock noise generation.

Chapter 6 summarizes the significant findings of this work.

Bibliography

[1] A.W. Morley, "Estimation of Aeroplane Noise Level: Some Empirical Laws With an Account of the Present Experiments on which They are Based," Aircraft Engineering, Vol. 11, no. 123, May 1939, pp.187-189.

[2] M.J. Lighthill, "On Sound Generated Aerodynamically: I. General Theory," Proceedings of the Royal Society of London, vol. 211, no. 1107, 1952, pp. 1-32.

[3] John M. Seiner, "Advances in High Speed Jet Aeroacoustics," AIAA paper AIAA- 84-2275, AIAA/NASA 9th Aeroacoustics Conference, 1984.

[4] Christopher K.W. Tam, "Supersonic Jet Noise," Annual Review of Fluid Mechanics, Vol. 27, 1995.

[5] G.M. Lilley, "Jet Noise Classical Theory and Experiments," Aeroacoustics of Flight Vehicles: Theory and Practice, Volume 1: Noise Sources, NASA Reference publication 1258, Volume 1, Harvey H. Hubbard, ed. pp. 211-285.

Chapter 2

Modeling of Sound Generating Mechanisms in a Supersonic Jet

2.1 Introduction

The inherently complicated nature of jet flows makes both theoretical analysis and direct numerical simulation impractical for realistic flow Mach and Reynolds numbers. The structure of the flow field of a supersonic jet is very complicated, consisting of regions of laminar flow, turbulent flow, and transitional flow. Within the jet there exist a myriad of structures of disparate scales, such as turbulent eddies and shock waves, which make analysis of the fluid dynamics practically impossible for general flows. Highly accurate numerical simulation of these flows is impractical because of the disparity of the scales required to be resolved in the computation.

In order to predict accurately the sound generated by complex jet flows, the essential elements of the jet fluid dynamics must be resolved in the computation.

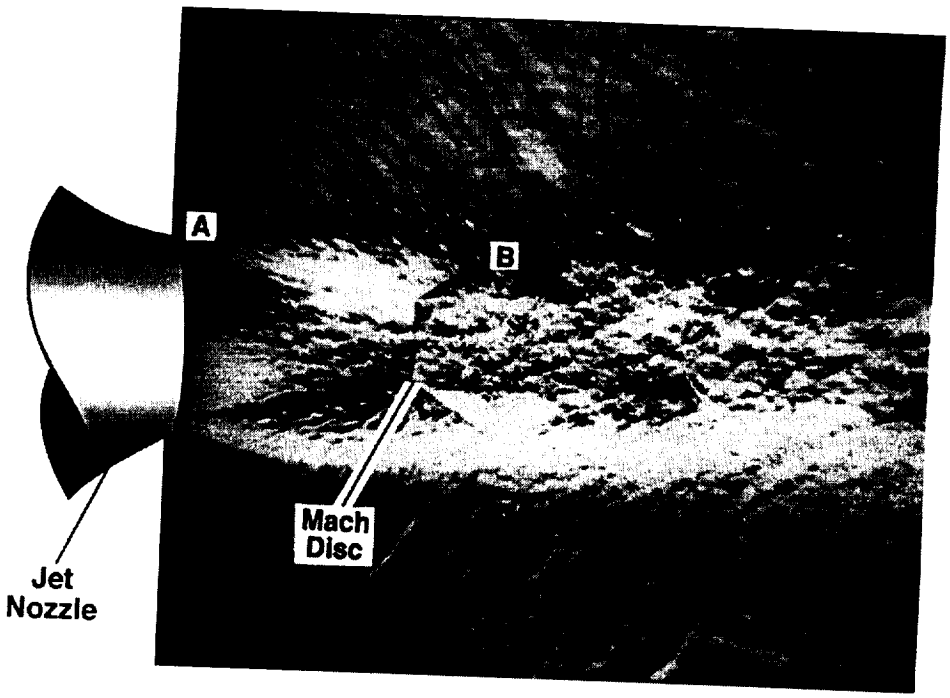

Figure 2.1: Schlieren photograph of an underexpanded jet.

Experimental studies of noise generation in supersonic jets have provided insight into what these essential elements may be. A result from an experimental investigation of sound generation in a supersonic axisymmetric jet is included in Figure 2.1. This photographic image, provided by Dr. J.M. Seiner of the Jet Noise Laboratory at NASA Langley Research Center [1], was produced by a horizontal spark schlieren of an underexpanded supersonic jet (ratio of exit pressure to ambient pressure is 3.05, and the jet design Mach number is 1.8) and confirms the complex nature of the jet flow. As the flow exits from the nozzle, it rapidly becomes turbulent. For the underexpanded case shown here, shock waves are also present in the flow, and a Mach disk is evident approximately one jet diameter downstream of the nozzle.

For the acoustician, the wave field outside the jet plume is of particular interest.

It is obvious that several types of waves are present, indicating that there are several types of sound generating mechanisms responsible.

Two types of wave fields are intense enough to be readily visualized on the schlieren photograph. The first appears to emanate from a region close to the nozzle exit near marker 'A' on the figure and radiate at approximately ± 30 degrees from the jet axis. These waves propagate to the far field as acoustic waves, and are thought to be generated by supersonically convecting eddies which occur when the jet flow is heated and in unheated flows when the plume Mach number approaches two [2]. The eddies create a form of sound known as "eddy Mach wave radiation", which generally dominates the noise spectrum in directions of its dominant directivity. The primary directivity can be determined by computing the angle complementary to the Mach angle. (The Mach angle is determined from the eddy convection velocity: $\mu = \sin^{-1} \frac{1}{M}$).

The second type of wave outside the jet plume appears to emanate from the terminal locations of the shock waves in the mixing layer. One such wave field is readily seen emanating from a region in the proximity of marker 'B' in the figure. This wave field appears to be more omni-directional than the eddy Mach wave radiation, because the wave fronts appear to spread spherically from the point of generation. This second type of acoustic wave is believed to be generated by the passage of turbulence through the shock waves and is referred to as "broadband shock noise" or "shock noise". The broad-band nature of this type of noise is illustrated in Figure 2.2.

Figure 2.2 shows the spectrum of a typical underexpanded supersonic jet at 150 degrees from the jet axis. The spectrum is characterized by three types of

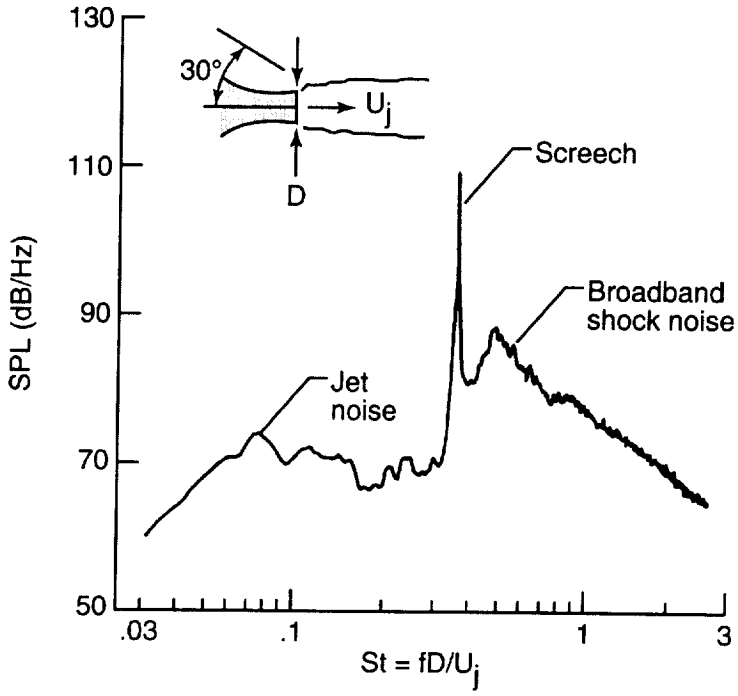

Figure 2.2: Spectrum of a typical supersonic underexpanded jet.

phenomena which are highlighted in the figure. The figure shows that these three components of noise tend to fall into distinct frequency bands. At low Strouhal number (a dimensionless frequency formed by the product of the frequency and jet diameter divided by the fully expanded jet velocity) jet noise dominates. Jet noise is generated by turbulent mixing within the jet. The peak in jet noise, at a Strouhal number of about 0.1, is believed to be generated by the large scale structures within the shear layer and is typically referred to as eddy Mach wave radiation. Both large and small scales within the jet generate mixing noise. The mixing of the fine scales produces the background level of jet noise.

The peak of the spectrum is known as jet screech. Screech typically falls between the jet noise and the broadband shock noise in the spectrum. The accepted

explanation for screech was originally proposed by Powell [3], who suggested that screech is generated when the turbulence interacting with shock waves in the flow develops a self-sustained aeroacoustic feed-back loop. The resonant phenomenon which generates a high amplitude sound at a particular frequency and its harmonics, is maintained by the shedding of a disturbance at the nozzle exit by the passing of sound past the nozzle lip. Although Powell's explanation of the screech phenomenon is useful in explaining general features of the phenomenon, there are features of jet screech which are still not understood [2].

The high Strouhal portion of the spectrum of Figure 2.2 is called broadband shock noise. Broadband shock noise is present in all shocked jet flows, and is due to the interaction of convecting disturbances with the shock waves in the jet plume. The broadband nature of this noise is due to the many scales of turbulent eddies in the flow. Experiments (e.g., [2], [5]) show that most of the broadband shock noise is directed slightly upstream.

Although jet engines are designed to be shock-free at design operating conditions, jet engines are often operated at off-design conditions. Thus, screech and broadband shock noise can contribute significantly to the sound being generated.

2.2 Models

Because jet flows are too complicated to be practically analyzed or directly simulated, the approach taken in this research is to identify elements essential to sound generation in supersonic jets, and analyze models of these mechanisms for insight into the sound generation processes. The models presented here are probably not the only models necessary for an in-depth understanding of sound generated by

supersonic jets. However, it is assumed that understanding isolated mechanisms will provide insight for reduction of noise levels within a real jet flow.

The basis for the models is the experimental evidence described in the first section of this chapter. Experimental data indicate that noise is generated by different types of mechanisms within the jet. To gain insight into the fundamental mechanisms associated with sound generation, the complex flow of a supersonic jet is modeled as illustrated in Figure 2.3. The first class of sound generating mechanisms in the supersonic jet arises from the interaction of flow disturbances with the shock waves. The elements which model the sound being generated by the interaction of flow disturbances with shock waves are illustrated on the left side of the figure: (1) the interaction of a vortex with a shock wave, and (2) the interaction of a plane sound wave with a shock. Because this research focuses on the noise generated by shocked flows, these two elements will be pursued in detail in Chapters 4 and 5.

Additional models of sound generating mechanisms which are not directly related to the presence of shock waves are illustrated on the right side of the figure. The model presented in the upper right of the figure is flow past a wavy wall. This models the component of sound generated by large scale structures within the jet plume. Clearly, one would expect Mach waves to be generated by flow past a wavy wall, and in the model, these Mach waves are analogous to the eddy Mach wave radiation from supersonic jets. The model presented in the lower right of Figure 2.3 is presented to model the interaction of turbulent structures within the jet, which is believed to be responsible for the background noise ("jet noise") of supersonic jet flows.

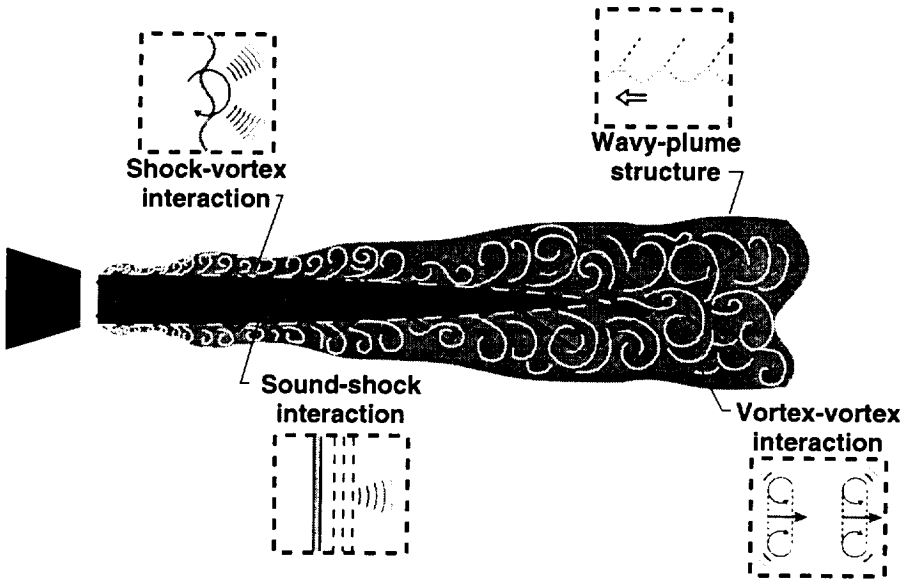

Figure 2.3: Fundamental sound generating mechanisms of supersonic jet flow.

2.3 Sound Generation by Shock Motion: Evaluation of Lighthill's Source Term and Far Field Sound

This section presents an analysis of the sound generation by shock motion in the context of Lighthill's acoustic analogy [6].

2.3.1 Background

Lighthill combined the equations governing the conservation of mass and momentum into the form of an inhomogeneous wave equation. A brief derivation of Lighthill's equation follows.

The physical law governing the conservation of mass written in indicial form is:

$$\frac{\partial \rho}{\partial t} + \frac{\partial (\rho u_j)}{\partial x_j} = Q \qquad j = 1, 2, 3 \tag{2.1}$$

where ρ is the fluid density, u_j is the $j-th$ component of velocity, t is time, x_i is the coordinate in the $i-th$ direction, and Q is the mass per unit time per unit volume injected into the fluid.

The conservation of momentum equations are written:

$$\rho\frac{\partial u_i}{\partial t}+\rho u_i\frac{\partial u_j}{\partial x_j}=-\frac{\partial P_{ij}}{\partial x_j}+F_i \quad i,j=1,2,3 \tag{2.2}$$

where F_i is an externally applied force, the stress tensor $P_{ij}=p\delta_{ij}-\sigma_{ij}$ where δ_{ij} is the Kroneker delta, and σ_{ij} is the viscous stress tensor, $\sigma_{ij}=2\mu e_{ij}-\lambda e_{kk}\delta_{ij}$, where $e_{ij}=\frac{1}{2}(\frac{\partial u_i}{\partial x_j}+\frac{\partial u_j}{\partial x_i})$, and μ and λ are the dynamic viscosity and second coefficient of viscosity, respectively.

Taking the inner product of u_i with Eqn. 2.1 and adding it to Eqn. 2.2, one obtains:

$$\frac{\partial \rho u_i}{\partial t}+\frac{\partial(\rho u_i u_j)}{\partial x_j}+\frac{\partial P_{ij}}{\partial x_j}=F_i+u_iQ \tag{2.3}$$

Differentiating Eqn. 2.1 with time, subtracting the divergence of Eqn. 2.3, and adding and subtracting $c_\infty^2\nabla^2\rho$, one obtains Lighthill's equation:

$$\frac{\partial^2\rho}{\partial t^2}-c_\infty^2\nabla^2\rho=\frac{\partial Q}{\partial t}-\frac{\partial(F_i+u_iQ)}{\partial x_i}+\frac{\partial^2 T_{ij}}{\partial x_i\partial x_j} \tag{2.4}$$

where the Lighthill stress tensor is defined:

$$T_{ij}=\rho u_i u_j-\sigma_{ij}+p\delta_{ij}-c_\infty^2\rho\delta_{ij} \tag{2.5}$$

The terms on the right hand side of 2.4 are the acoustic source terms. These terms represent sound generated by unsteady mass addition ($\frac{\partial Q}{\partial t}$), unsteady forces

$(\frac{\partial(F_i+u_iQ)}{\partial x_i})$, nonlinear viscous effects, turbulence, and nonlinear propagation $(\rho u_i u_j)$, and non-isentropic effects such as shock waves and heat addition $((p-\rho c_\infty^2)\delta_{ij})$. Effects of viscosity on the sound generation are represented by σ_{ij}.

2.3.2 Source Terms

Here, Lighthill's equation will be used to analyze the sound generated by shock oscillation. To simplify the analysis, dissipation effects are neglected, and only the velocity component normal to the shock, u, is considered. Since there are no applied forces or unsteady mass addition, the Lighthill source term simplifies to

$$T_{11} = \rho uu + p - \rho c_\infty^2 \tag{2.6}$$

The source term of the Lighthill equation requires that the second partial derivative of T_{11} be taken with respect to x. It is beneficial to use generalized functions because ordinary derivatives do not exist across the shock. The definition of a generalized derivative in one dimension is [8]:

$$\frac{\bar{\partial} f(x)}{\partial x} = \frac{\partial f(x)}{\partial x} + \Delta f \delta(x - x_s) \tag{2.7}$$

where $\frac{\bar{\partial}}{\partial x}$ represents the generalized derivative operator, $\frac{\partial}{\partial x}$ is the ordinary derivative, and Δf represents the jump in the function f at the discontinuity located at $x = x_s$.

Applying 2.7 twice to obtain $\frac{\partial^2 T_{11}}{\partial x^2}$,

$$\begin{aligned}
\frac{\bar{\partial} T_{11}}{\partial x} &= \frac{\partial T_{11}}{\partial x} + \Delta T_{11}\delta(x - x_s) \\
\frac{\bar{\partial}^2 T_{11}}{\partial x^2} &= \frac{\partial^2 T_{11}}{\partial x^2} + \frac{\partial}{\partial x}(\Delta T_{11}\delta(x - x_s)) + \Delta(\frac{\partial T_{11}}{\partial x})\delta(x - x_s)
\end{aligned} \tag{2.8}$$

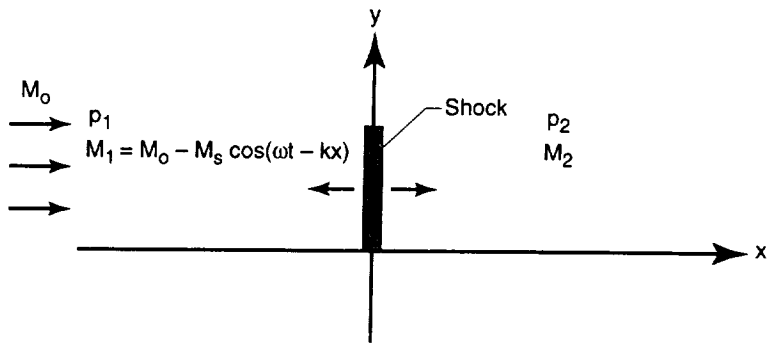

Figure 2.4: Schematic of shock oscillation used in the determination of Lighthill's source term.

Thus, the Lighthill source term for sound generated by a moving shock has components which resemble shearing stresses (quadrupole), unsteady forces (dipole), and mass addition (monopole), as represented by the first, second and third terms on the right and side of Equation 2.8, respectively.

In classical acoustics, where sound generation is considered in an ambient medium, the sound pressure associated with monopoles, dipoles and quadrupoles is proportional to the second, third, and fourth power of the source Mach number, respectively. Therefore, the monopole source dominates at low Mach numbers, and the quadrupole source dominates at high Mach numbers. However, for sound generation at transonic speeds, each component may contribute significantly to the sound generation. It is a purpose of this section to analytically determine which term dominates the shock noise generation.

To determine the behavior of the monopole, dipole and quadrupole terms as functions of Mach number, consider a planar shock, set in motion by an upstream disturbance in Mach number, as illustrated in Figure 2.4. The Mach number

upstream of the shock is

$$M_1 = M_0 - M_s \cos(\omega t - kx) \tag{2.9}$$

where M_0 is the undisturbed upstream Mach number, M_s is the maximum amplitude of the disturbance Mach number, ω is the frequency of the disturbance, and k is its wavenumber.

Disturbances in pressure, density, and sound speed upstream of the shock are neglected because these quantities are proportional to the square of the upstream disturbance Mach number.

Monopole Source Term

The monopole term on the right hand side of Equation 2.8 is

$$\Delta(\frac{\partial T_{11}}{\partial x})\delta(x - x_s) \tag{2.10}$$

Considering for now only $\Delta(\frac{\partial T_{11}}{\partial x})$,

$$\begin{aligned}
\Delta(\frac{\partial T_{11}}{\partial x}) &= \left.\frac{\partial T_{11}}{\partial x}\right|_2 - \left.\frac{\partial T_{11}}{\partial x}\right|_1 \\
&= \frac{\partial}{\partial x}[\rho_2 c_2^2 M_2^2 + p_2 - \rho_2 c_\infty^2] - \frac{\partial}{\partial x}[\rho_1 c_1^2 M_1^2 + p_1 - \rho_1 c_\infty^2] \\
&\approx (c_2^2 M_2^2 - c_\infty^2)\frac{\partial \rho_2}{\partial x} + 2\rho_2 c_2 M_2 \frac{\partial (c_2 M_2)}{\partial x} + \frac{\partial p_2}{\partial x} - 2\rho_1 c_1^2 M_1 \frac{\partial M_1}{\partial x}
\end{aligned} \tag{2.11}$$

since ρ_1, p_1, and c_1 are, to first order, constant.

To evaluate Equation 2.11 in terms of the upstream density, sound speed and Mach number, the well-known shock jump relations (see, e.g. [7]) are used. These relations are presented below for completeness. The second equality refers to the case of an ideal gas with the ratio of specific heats, $\gamma = 1.4$.

$$\frac{p_2}{p_1} = \frac{2\gamma M_1^2 - (\gamma - 1)}{(\gamma + 1)} = \frac{7M_1^2 - 1}{6} \tag{2.12}$$

$$\frac{\rho_2}{\rho_1} = \frac{(\gamma + 1)M_1^2}{(\gamma - 1)M_1^2 + 2} = \frac{6M_1^2}{M_1^2 + 5} \tag{2.13}$$

$$\frac{u_2}{u_1} = \frac{(\gamma - 1)M_1^2 + 2}{(\gamma + 1)M_1^2} = \frac{M_1^2 + 5}{6M_1^2} \tag{2.14}$$

To compute the Lighthill monopole source term, the derivatives of the downstream pressure, density, and velocity are required. Taking the first derivative with respect to x, for the case of $\gamma = 1.4$, one obtains:

$$\begin{aligned} \frac{\partial p_2}{\partial x} &= \frac{7}{3} p_1 M_1 \frac{\partial M_1}{\partial x} \\ &= \frac{5}{3} \rho_1 c_1^2 M_1 \frac{\partial M_1}{\partial x} \end{aligned} \tag{2.15}$$

$$\frac{\partial (c_2 M_2)}{\partial x} = \frac{c_1}{6} \frac{k(M_1^2 - 5)}{M_1^2} \frac{\partial M_1}{\partial x} \tag{2.16}$$

$$\frac{\partial \rho_2}{\partial x} = 60 \rho_1 \frac{M_1}{(5 + M_1^2)^2} \frac{\partial M_1}{\partial x} \tag{2.17}$$

where $\frac{\partial M_1}{\partial x} = -M_s k \sin(\omega t - kx)$.

Substituting in Equations 2.12, 2.13, and 2.14 into 2.11, and working through the algebra one obtains:

$$\Delta(\frac{\partial T_{11}}{\partial x}) = -60 \rho_1 c_\infty^2 \frac{M_1}{(M_1^2 + 5)^2} \frac{\partial M_1}{\partial x}$$

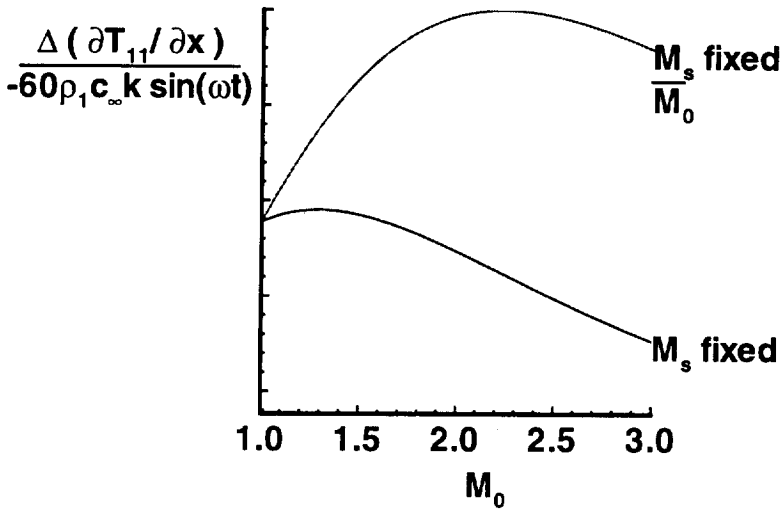

Figure 2.5: Normalized monopole component of the Lighthill source term sound generated by a sinusoidally oscillating shock.

$$= -60\rho_1 c_\infty^2 \frac{M_1 M_s k}{(M_1^2+5)^2} \sin(\omega t - kx) \tag{2.18}$$

Substituting $M_1 = M_0 - M_s \cos(\omega t - kx)$, and keeping only terms of order M_s, one obtains:

$$60\rho_1 c_\infty^2 \frac{M_0 M_s k}{(M_0^2+5)^2} \sin(\omega t - kx) \tag{2.19}$$

Equation 2.19, normalized by $60\rho_1 c_\infty^2 k \sin(\omega t - kx)$, is plotted as a function of M_0 (for constant wavenumber) in Figure 2.5.

Two cases are shown. The upper curve in the figure represents the source term when the ratio of perturbation Mach number to upstream Mach number, $\frac{M}{M_0}$ is held fixed. The lower curve represents the source term for a fixed perturbation Mach number, M_s. Clearly, the Lighthill monopole source term reaches a maximum value. To determine the exact location at which it maximizes, the first derivative

of Equation 2.18 with respect to M_0 is determined and set equal to zero. The value of M_0 for which this derivative is zero, holding M fixed, is found to be $M_0 = \sqrt{\frac{5}{3}} \approx 1.29$. The value of M_1 for which $\frac{\partial}{\partial M_0}\Delta(\frac{\partial T_{11}}{\partial x})$ is zero, holding $\frac{M}{M_0}$ fixed, is found to be $M_0 = \sqrt{5} \approx 2.24$.

Thus, the monopole source term reaches a maximum when, for constant shock velocity amplitude, and constant disturbance wavenumber, $M_0 = \sqrt{\frac{5}{3}}$. When the ratio of the shock velocity amplitude to the pre-shock Mach number is held constant, the source term maximizes at $M_0 = \sqrt{5}$ for a fixed wavenumber.

For an acoustic disturbance, the wavenumber varies with upstream Mach number,

$$\begin{aligned} k &= \frac{\omega}{c_1(1+M_1)} \\ &= \frac{\omega}{c_1(1+M_0)} + \frac{\cos(kx-\omega t)}{(1+M_0)^2}M_s + O(M_s)^2 \end{aligned} \tag{2.20}$$

The wavenumber may be approximated by $k = \frac{\omega}{c_1(1+M_0)}$ and substituted into Equation 2.19 while maintaining a truncation error of order $(M_s)^2$. Furthermore, if the sound speed approaching infinity is taken to be the stagnation sound speed, the relationship between c_1 and c_∞ is:

$$\begin{aligned} c_1 &= c_\infty\sqrt{\frac{5}{5+M_1^2}} \\ &= c_\infty\sqrt{\frac{5}{5+M_0^2}}\left(1+\frac{M_0\cos(\omega t-kx)}{(5+M_0^2)}M_s\right) + O(M_s^2) \end{aligned} \tag{2.21}$$

Thus, the monopole source term for $k = k(M_0)$ is

$$\frac{-60\rho_1 c_\infty \omega M_0 M_s \sin(\omega t - kx)}{\sqrt{5}(M_0^2+5)^{3/2}(1+M_0)} \tag{2.22}$$

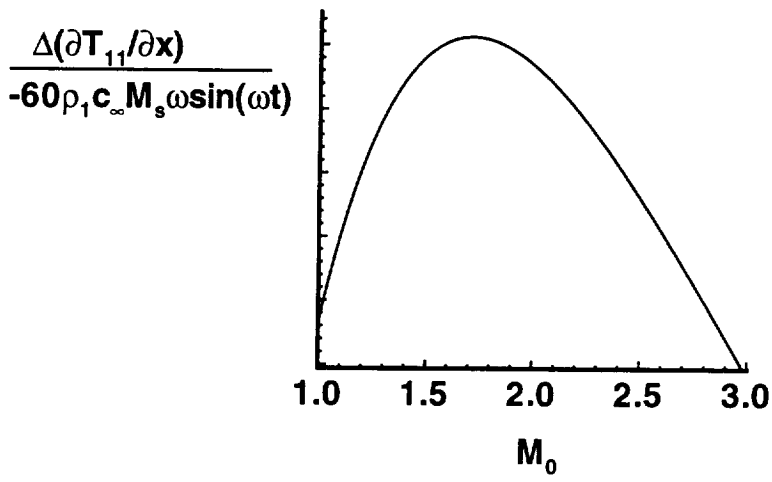

Figure 2.6: Normalized strength of monopole component of the Lighthill source term for a sinusoidally oscillating shock. Wavenumber k is a function of upstream Mach number and sound speed.

Equation 2.22 normalized by $-60\rho_1 c_\infty \omega M_s \sin(\omega t - kx)$ is plotted in Figure 2.6.

Dipole Term

Consider now the dipole term of Equation 2.8. This term can be written:

$$\frac{\partial}{\partial x}\left[\Delta T_{11}\delta(x - x_s)\right] = \Delta T_{11}\delta'(x - x_s) \tag{2.23}$$

since the jump across the shock is not a function of x. Thus, the jump in T_{11} is of interest.

$$\Delta T_{11} = \rho_2 u_2^2 + p_2 - \rho_2 c_\infty^2 - [\rho_1 u_1^2 + p_1 - \rho_1 c_\infty^2] \tag{2.24}$$

But, from the unsteady jump relations (see Appendix A for derivation),

$$\rho_2(u_2 - u_s) \;=\; \rho_1(u_1 - u_s)$$

$$\rho_2 u_2(u_2 - u_s) + p_2 \;=\; \rho_1 u_1(u_1 - u_s) + p_1 \tag{2.25}$$

one can solve for the change in pressure across the shock:

$$p_2 - p_1 = \rho_1(u_1 - u_s)(u_1 - u_2) \tag{2.26}$$

Substituting 2.26 into 2.24, and neglecting higher order terms in u_s, one obtains:

$$\Delta T_{11} \approx -(\rho_2 - \rho_1)c_\infty^2 \tag{2.27}$$

Therefore, upon substitution of 2.13 into 2.27, and simplification, the following expression for the dipole source term is obtained:

$$\Delta T_{11} = -5\rho_1 c_\infty^2 \left(\frac{M_1^2 - 1}{M_1^2 + 5}\right) \tag{2.28}$$

Substituting $M_1 = M_0 - M_s \cos(\omega t - kx)$ into Equation 2.28 and neglecting terms of order M_s^2 and higher, one obtains:

$$\Delta T_{11} = \frac{-5\rho_1 c_\infty^2}{(M_0^2 + 5)}\left[(M_0^2 - 1) - \frac{12 M_s M_0 \cos(\omega t - kx)}{M_0^2 + 5}\right] \tag{2.29}$$

It is interesting that unlike the monopole term, the dipole term contains both zero-th and first order terms in M_s. Another difference between the monopole and dipole terms is that the wavenumber affects both the amplitude and phase of the monopole term, while it affects only the phase of the dipole term. It is also interesting that the monopole term and the first order component of the dipole term are identical except for the phase and the multiplicative factor of the wavenumber.

As illustrated in Figure 2.7, there are no local extrema for the dipole source term when the flow is supersonic. This can be verified analytically by taking the derivative of Equation 2.28 with respect to M_0 as for the monopole case.

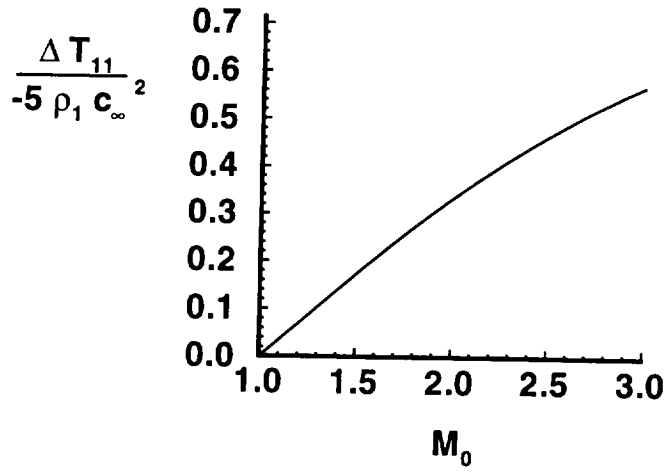

Figure 2.7: Normalized strength of dipole component of the Lighthill source term for a sinusoidally oscillating shock.

Quadrupole Term

Finally, consider the quadrupole component of Eqn. 2.8. The quadrupole term requires that the second ordinary derivative of the Lighthill stress tensor component T_{11} with respect to x be evaluated. Thus,

$$\begin{aligned} \frac{\partial^2 T_{11}}{\partial x^2} &= \frac{\partial}{\partial x}[2\rho u \frac{\partial u}{\partial x} + u^2 \frac{\partial \rho}{\partial x} + \frac{\partial p}{\partial x} - c_\infty^2 \frac{\partial \rho}{\partial x}] \\ &= 2\rho u \frac{\partial^2 u}{\partial x^2} + 4u \frac{\partial u}{\partial x}\frac{\partial \rho}{\partial x} + 2\rho(\frac{\partial u}{\partial x})^2 + (u^2 - c_\infty^2)\frac{\partial^2 \rho}{\partial x^2} + \frac{\partial^2 p}{\partial x^2} \end{aligned} \quad (2.30)$$

The evaluation of Eqn. 2.30 upstream of the shock is simple, since the derivatives in p , ρ, and c are high-order, and hence, neglected. The evaluation of Eqn. 2.30 upstream is:

$$\left.\frac{\partial^2 T_{11}}{\partial x^2}\right|_1 = 2\rho_1 c_1^2 \left[\left(\frac{\partial M_1}{\partial x}\right)^2 + M_1 \frac{\partial^2 M_1}{\partial x^2}\right] \quad (2.31)$$

Substituting $M_1 = M_0 - M_s \cos(\omega t - kx)$ and neglecting higher order terms in M_s, this expression reduces to

$$\left.\frac{\partial^2 T_{11}}{\partial x^2}\right|_1 = 10\,\rho_1\, c_\infty^2 k^2\, \frac{M_0 M_s \cos(\omega t - kx)}{(5 + M_0^2)} \tag{2.32}$$

For an acoustic upstream disturbance for which the wavenumber is a function of Mach number, this becomes:

$$\left.\frac{\partial^2 T_{11}}{\partial x^2}\right|_1 = 2\,\rho_1\, \omega^2\, \frac{M_0 M_s \cos(\omega t - kx)}{(5 + M_0^2)(1 + M_0)^2} \tag{2.33}$$

The evaluation of the quadrupole term downstream of the shock is more complicated since the second derivatives with respect to x of ρ_2, u_2, and p_2 are required. The second derivatives of the variables in Eqns. 2.12, 2.13, and 2.14 are:

$$\frac{\partial^2 \rho_2}{\partial x^2} = \frac{60\rho_1}{\left(5 + {M_1}^2\right)^3}\left((5 - 3M_1^2)\left(\frac{\partial M_1}{\partial x}\right)^2 + (5\,M_1 + {M_1}^3)\frac{\partial^2 M_1}{\partial x^2}\right) \tag{2.34}$$

$$\frac{\partial^2 p_2}{\partial x^2} = \frac{5}{3}{c_1}^2 \rho_1 \left(\left(\frac{\partial M_1}{\partial x}\right)^2 + M_1\, \frac{\partial^2 M_1}{\partial x^2}\right) \tag{2.35}$$

$$\frac{\partial^2 u_2}{\partial x^2} = \frac{c_1}{6M_1^3}\left(10\left(\frac{\partial M_1}{\partial x}\right)^2 - (5\,M_1 - {M_1}^3)\frac{\partial^2 M_1}{\partial x^2}\right) \tag{2.36}$$

where $\frac{\partial M_1}{\partial x} = -kM_s \sin(\omega t - kx)$, and $\frac{\partial^2 M_1}{\partial x^2} = k^2 M_s \cos(\omega t - kx)$.

Substituting Eqns. 2.35, 2.34, and 2.36 into Eqn. 2.30 and algebraic manipulation provides:

$$\begin{aligned}\left.\frac{\partial^2 T_{11}}{\partial x^2}\right|_2 &= 2\,\rho_1\, c_1^2 \left[\left(\frac{\partial M_1}{\partial x}\right)^2 + M_1\, \frac{\partial^2 M_1}{\partial x^2}\right] \\ &+ 12\rho_1 c_\infty^2 \left[\frac{{M_1}^4 + 20M_1^2 - 25}{\left(5 + {M_1}^2\right)^3}\right]\left(\frac{\partial M_1}{\partial x}\right)^2\end{aligned}$$

$$+ \quad 12\rho_1 c_\infty^2 \left[\frac{-5M_1}{\left(5+{M_1}^2\right)^2}\right] \frac{\partial^2 M_1}{\partial x^2} \tag{2.37}$$

Substituting $M_1 = M_0 - M_s \cos(\omega t - kx)$ and neglecting higher-order terms, one obtains:

$$10\rho_1 c_\infty^2 k^2 \frac{M_0 M_s}{(5+M_0^2)^2}(M_0^2-1)\cos(\omega t - kx) \tag{2.38}$$

It is interesting to note that the quadrupole source term contains only first order terms (and higher) in M_s and goes to zero as $M_0 \to 1$.

Substituting in Eqn. 2.20 for $k = k(M_0)$, the quadrupole term becomes:

$$10\rho_1 \omega^2 \frac{M_0 M_s}{(5+M_0^2)(1+M_0)}(M_0-1)\cos(\omega t - kx) \tag{2.39}$$

It is interesting to note that the quadrupole source term goes to zero as $M_0 \to 1$, and that the quadrupole and dipole source terms have the same phase.

2.4 Evaluation of Acoustic Pressure

The previous section provides expressions for the monopole, dipole and quadrupole source terms of Lighthill's equation for shock motion in one dimension. In order to make statements regarding the relative importance of these components to the far field sound, a Green's function approach is used to solve for the far field acoustic pressure. The primary assumptions in this analysis are that only the first order terms in perturbation Mach number M_s are necessary to determine the relative importance of the monopole, dipole and quadrupole terms, that the observer is located in the far field, and that the shock is a finite disk in a plug flow, as illustrated in Figure 2.8. The flow outside the plug is ambient and is characterized by the density ρ_∞ and the sound speed c_∞. For the analysis presented here,

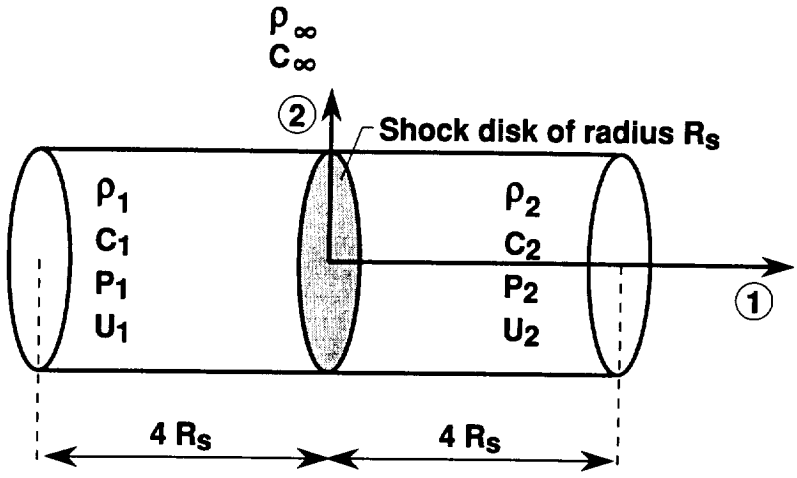

Figure 2.8: Schematic of shock disk in plug flow. Flow variables are functions of position along the axial coordinate. The shock is located at the center of the volume.

contributions of the interface between the plug flow and ambient medium to the far field sound are neglected.

2.4.1 Monopole

In order to evaluate the far field sound resultant from the monopole source, a cylindrical coordinate system is set up with the origin at the shock disk center, as illustrated in Figure 2.9. The position of the source point along the disk is denoted by $\vec{y}$ and the position to the observer is denoted by $\vec{x}$. The magnitude of the vector connecting the source and observer points $\vec{R} = \vec{x} - \vec{y}$ is denoted R, which is determined by geometrical arguments to be:

$$R = \sqrt{r_0^2 + \sigma^2 - 2r_0\sigma \sin\theta \cos(\phi - \chi)} \tag{2.40}$$

Making the far field approximation $\frac{\sigma^2}{r_0^2} \to 0$ and employing the binomial expan-

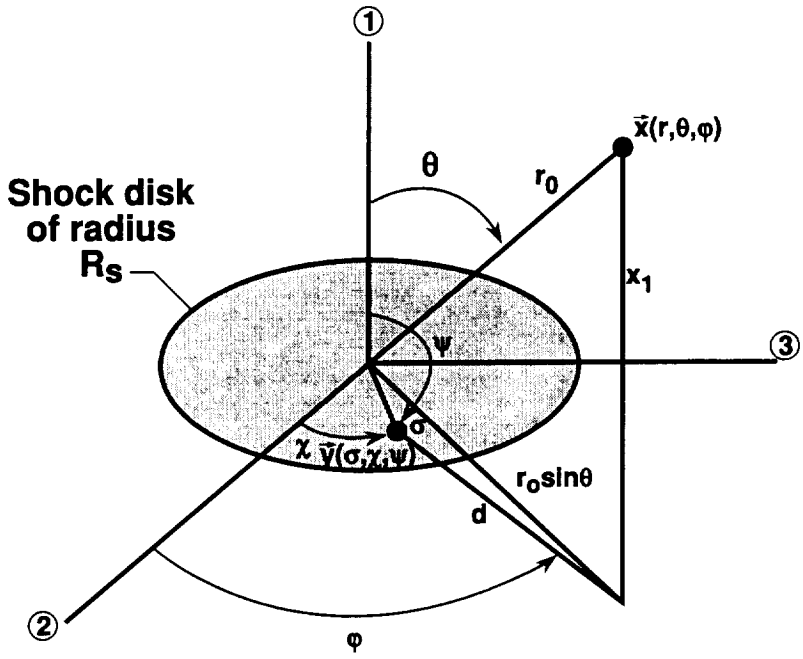

Figure 2.9: Coordinate system used in evaluation of surface integrals.

sion, this simplifies to:

$$R \approx r_0[1 - \frac{\sigma}{r_0} \sin\theta \cos(\phi - \chi)] \tag{2.41}$$

where, as illustrated in Figure 2.9, r_0 is the distance from the observer to the center of the shock, σ is the radial coordinate to the source point, θ is the angle from the jet axis to the observer, ϕ is the observer angle about the axis of symmetry, and χ is the angle to the source point in the plane of the shock disk. Applying the Green's function approach to solve for the far field acoustic pressure resulting from the monopole component of the Lighthill source term, the source term is multiplied by the free space Green's function and integrated over the source volume V and time τ:

$$p_M(\vec{x},t) = \frac{-1}{4\pi}\int_V\int_\tau 60\rho_1 c_\infty^2 \frac{M_0 M_s k}{(M_0^2+5)^2}\sin(\omega\tau - ky_1)\delta(y_1 - y_{1s})\frac{\delta(\tau - t + R/c_\infty)}{R}dV\,d\tau \tag{2.42}$$

where $y_{1s} = 0$ is the shock position, and $dV = dy_1\sigma d\sigma d\chi$ is the incremental volume. Making the far field assumption such that $\frac{1}{R} \approx \frac{1}{r_0}$, and integrating over y_1,

$$p_M(\vec{x},t) = \frac{-1}{4\pi r_0}\int_{A_s}\int_\tau 60\rho_1 c_\infty^2 \frac{M_0 M_s k}{(M_0^2+5)^2}\sin(\omega\tau - ky_{1s})\delta(\tau - t - R/c_\infty)dA_s\,d\tau \tag{2.43}$$

where A_s is the shock area. Integrating over source time τ,

$$\begin{aligned} p_M(\vec{x},t) &= \frac{-1}{4\pi r_0}\int_{A_s} 60\rho_1 c_\infty^2 \frac{M_0 M_s k}{(M_0^2+5)^2}\sin(\omega t - R/c\infty - ky_{1s})dA_s \\ &= \frac{-60\rho_1 c_\infty^2}{4\pi r_0}\frac{M_0 M_s k}{(M_0^2+5)^2} \\ &\quad \int_0^{R_s}\int_0^{2\pi}\sin(\omega t - (r_0 - \frac{\sigma\sin\theta\cos(\phi-\chi)}{c_\infty - ky_{1s}})\sigma d\sigma d\chi \end{aligned} \tag{2.44}$$

Integrating with the aid of expressions 3.719-2 and 3.715-13 in [9], the analytical expression for the monopole source pressure is:

$$p_M(x,t) = \frac{-30\rho_1 c_\infty^3 k M_0 M_s}{(M_0^2+5)^2 r_0}\frac{R_s}{\omega\sin\theta}J_1\left(R_s\sin\theta\frac{\omega}{c_\infty}\right)\sin(\omega t - \frac{\omega r_0}{c_\infty}) \tag{2.45}$$

where J_1 is the first order Bessel function of the first kind.

2.4.2 Dipole

Again using the Green's function approach to solve for the pressure due to the dipole component of the Lighthill source term:

$$p_D(\vec{x},t) = \frac{1}{4\pi}\int_V\int_\tau \frac{-5\rho_1 c_\infty^2(M_0^2-1)}{(M_0^2+5)^2}\delta'(y_1 - y_{1s})\frac{\delta(\tau - t + \frac{R}{c_\infty})}{R}$$

$$+ \quad \frac{60\rho_1 c_\infty^2 M_s M_0}{(M_0^2+5)^2}\cos(\omega\tau - ky_1)\delta'(y_1 - y_{1s})\frac{\delta(\tau - t + \frac{R}{c_\infty})}{R}dVd\tau \tag{2.46}$$

Making the far field approximation $\frac{1}{R} \approx \frac{1}{r_0}$, integrating the first term over τ, and using the fact that [8]:

$$\int f(y_1)\delta'(y_1 - y_{1s})dy_1 = -\left[\frac{df}{dy_1}\right]_{y_{1s}} \tag{2.47}$$

the integral of the first term goes to zero. Making the far field approximation and integrating the second term over τ:

$$p_D(\vec{x},t) = \frac{1}{r_0}\int_V \frac{60\rho_1 c_\infty^2 M_s M_0}{(M_0^2+5)^2}\cos(\omega(t - R/c_\infty) - ky_1)\delta'(y_1 - y_{1s})dV \tag{2.48}$$

Integrating over y_1 using Eqn. 2.47:

$$\begin{aligned} p_D(\vec{x},t) &= \frac{1}{r_0}\frac{60\rho_1 c_\infty^2 M_s M_0}{(M_0^2+5)^2}\int_{A_s} -\frac{d}{dy_1}\left[\cos(\omega(t - R/c_\infty) - ky_1)\right]|_{y_1=0}dA_s \\ &= \frac{1}{r_0}\frac{60\rho_1 c_\infty^2 M_s M_0}{(M_0^2+5)^2}\int_{A_s} \sin(\omega(t - R/c_\infty) - ky_1)\left[-k - \frac{\omega}{c_\infty}\frac{\partial R}{\partial y_1}\right]dA_s \end{aligned} \tag{2.49}$$

where $\frac{\partial R}{\partial y_1} = -\cos\theta$, and $dA_s = \sigma d\sigma d\chi$. Integrating over the shock area, the expression for the dipole source contribution to the far field sound is:

$$p_D(\vec{x},t) = \frac{-30\rho_1 c_\infty^3 M_s M_0}{(M_0^2+5)^2 r_0}(k - \frac{\omega}{c_\infty}\cos\theta)\sin(\omega(t - r_0/c_\infty)\frac{R_s}{\omega\sin\theta}J_1\left(\frac{R_s\omega\sin\theta}{c_\infty}\right) \tag{2.50}$$

It is interesting to note that

$$p_D(\vec{x},t) = p_M(\vec{x},t)\quad\left(1 - \frac{\omega\cos\theta}{c_\infty k}\right) \tag{2.51}$$

2.4.3 Quadrupole

Using the Green's function approach to determine the contribution of the downstream part of the quadrupole source term to the far field sound,

$$p_Q(\vec{x},t) = \int_V \int_\tau 10\rho_1 c_\infty^2 k^2 \frac{M_0 M_s (M_0^2-1)}{(M_0^2+5)^2} \frac{\delta(\tau - t + \frac{R}{c_\infty})}{R} \cos(\omega\tau - k y_1) dV d\tau \tag{2.52}$$

where $R = \sqrt{r_0^2 + y_1^2 + \sigma^2 - 2r_0 y_1 \cos\theta - 2r_0\sigma \sin\theta\cos\chi}$. Making the far field approximation that $\frac{\sigma^2}{r_0^2} \approx 0$ and $\frac{y_1^2}{r_0^2} \approx 0$, and using the binomial expansion, $R \approx r_0[1 - \frac{y_1}{r_0}\cos\theta - \frac{\sigma}{r_0}\sin\theta\cos\chi]$. Note that in integrating the quadrupole term, the integral is over the entire source volume, since there are no delta functions which limit the integral to the surface. This provides a challenge for this model because integrating over an infinite volume does not correspond to physical jet flows. Therefore, for the purposes of this analysis, the volume term is limited to a length $-4R_s \leq y_1 \leq 4R_s$ along the axial coordinate. This range is selected to approximately correspond to average shock spacing in supersonic nozzles [10]. Therefore, for integration of the downstream quadrupole term, the integration limits are $0 \leq y_1 \leq 4R_s$. Attempts at obtaining an analytical expression for this integral were unsuccessful. Therefore, numerical integration is used to evaluate the quadrupole term.

To simplify the comparisons and isolate the sound generated downstream on the sound field, only the region downstream of the shock is considered in the volume integration. For the purposes of determining the relative importance of the monopole, dipole, and quadrupole terms it is also assumed that the source is compact, i.e., the wavelength of the sound is large compared to the source size. The use of the compact assumption allows an analytical expression for the quadrupole

term to be obtained, since R in the argument of the cosine term in Equation 2.52 reduces to r_0.

Employing the compact source assumption, the analytical expressions for the monopole, dipole, and quadrupole terms are found to be:

$$p_M(\vec{x},t) = \frac{-15\rho_1 c_\infty^2 k A_s M_0 M_s}{(M_0^2+5)^2 r_0 \pi} \sin(\omega t - \frac{\omega r_0}{c_\infty}) \tag{2.53}$$

$$p_D(\vec{x},t) = p_M(\vec{x},t)\left[1 - \frac{\omega \cos\theta}{c_\infty k}\right] \tag{2.54}$$

$$p_Q(\vec{x},t) = \frac{-5\rho_1 c_\infty^2 k A_s M_0 M_s}{(M_0^2+5)^2 r_0 \pi}(M_0^2-1)\sin[kR_s]\cos[\omega t - \frac{\omega r_0}{c_\infty} - kR_s] \tag{2.55}$$

Figure 2.10 shows the normalized acoustic root-mean-square pressure of the monopole, dipole, and quadrupole terms for a particular case with an observer located 100 shock disk radii ($r_0 = 100$) away from the mean shock position at an angle of $\theta = \frac{\pi}{4}$ from the jet axis. For ease of comparison, the root-mean-square pressure is normalized by the constant multiplicative factor of the monopole, dipole, and quadrupole pressure terms, namely:

$$\frac{15\rho_1 c_\infty^2 k A_s M_0 M_s}{\pi r_0 (M_0^2+5)^2} \tag{2.56}$$

and the flow variables are normalized with respect to the sound speed c_∞, the shock disk radius R_s, and the upstream density ρ_1. For these comparisons, the wavenumber, k, varies with the mean flow Mach number as prescribed in Eqn. 2.20. There are several features worth noting on this figure. First, the quadrupole term increases with mean flow Mach number more rapidly with increasing frequency.

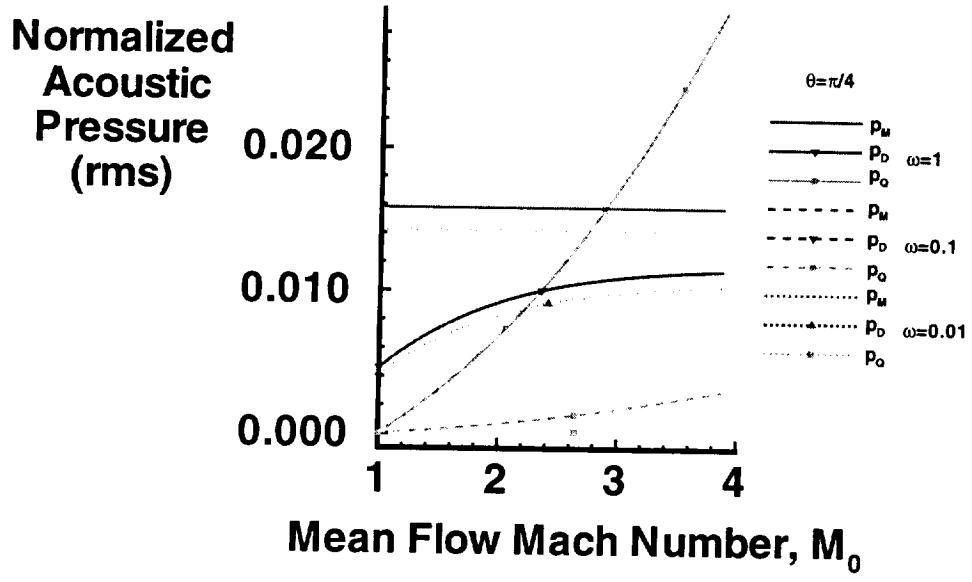

Figure 2.10: Root-mean-square far field pressure of the monopole, dipole, and quadrupole terms in the Lighthill analysis of shock noise. Results for three frequencies are shown.

The dipole terms increase with mean flow Mach number. The variation in the monopole terms is an order of magnitude smaller than the variation in the dipole terms. Although difficult to see on this scale, the monopole terms peak and then decrease with increasing Mach number. The monopole terms dominate for the low frequencies over the entire Mach number range, and for the high frequency case at low Mach For the case $\omega = 1$, the quadrupole term begins to dominate at about $M_0 = 2.8$. At low frequencies (for which the source is highly compact), the contribution of the quadrupole terms is negligible over the Mach number range considered in the analysis. The wavelength of the sound is

$$\lambda = \frac{2\pi c_\infty \sqrt{5}(1 + M_0)}{\omega\sqrt{5 + M_0^2}} \tag{2.57}$$

Thus, low frequencies correspond to highly compact sources. For example, for $\omega = 1$, the wavelength over the range of $1 \leq M_0 \leq 3$ is $11.5 \leq \lambda \leq 15$. The range of wavelengths are not much larger than the source size ($4R_s = 4$), and the compact assumption begins to break down. On the other hand, the range of wavelength for a source frequency of $\omega = 0.1$ is $115 \leq \lambda \leq 150$, and the compact assumption is valid.

Figure 2.11 shows the effect of observer position on the root-mean-square pressure of the monopole, dipole, and quadrupole terms. The results shown are for an observer located at 100 shock disk radii away from the mean shock position, at angles of $\theta = 0$, $\frac{\pi}{4}$, and $\frac{\pi}{2}$ from the jet axis. The monopole and quadrupole terms are unaffected by the change in observer position; P_M at all observer positions shown is seen to change only modestly about a value of approximately 0.016, and p_Q is seen to increase with mean flow Mach number from 0 at $M_0 = 1$ to approximately

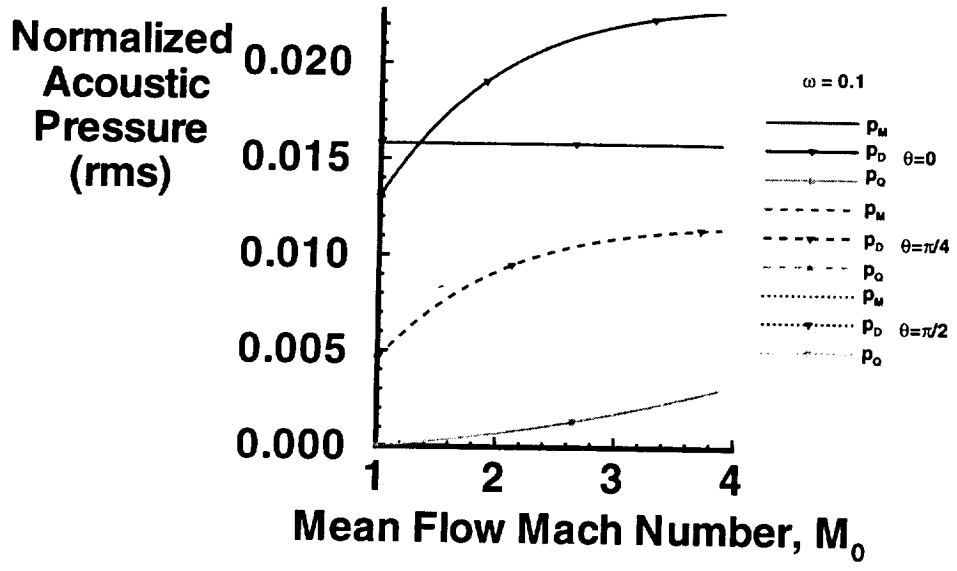

Figure 2.11: Root-mean-square far field pressure of the monopole, dipole, and quadrupole terms in the Lighthill analysis of shock noise. Results for three observer angles are shown.

0.003 at $M_0 = 3.8$. The dipole component is affected by the observer position. The dipole term is stronger at observer angles closely aligned to the jet axis, which is consistent with directivity patterns typical of dipoles. In addition, the dipole term reduces to the monopole term at an observer position of $\theta = \pi/2$.

2.5 Conclusions

Detailed analysis and direct numerical simulation of the sound generated by realistic supersonic jet flows are currently impractical. One way to gain insight into the sound generating mechanisms of such a complicated flow structure is to model the elements considered to be essential to the sound-generation process. Four essential elements were presented: Flow past a wavy wall, vortex-vortex interaction, sound-shock interaction and vortex-shock interaction. Because the focus of this work is on noise generation in shocked flows, the last two of these elements flows will be studied numerically in Chapters 4 and 5.

This chapter presented an analysis of the Lighthill source terms associated with a model of an oscillating shock. The results presented for the acoustic pressure are accurate to first order in the perturbation Mach number, and are valid only for an observer in the far field. The figures presented are valid for situations in which the source is compact. The analysis shows that the monopole, dipole, and quadrupole terms are all potentially important in shock noise generation. The term which dominates in a particular situation depends upon the observer position, frequency, and mean flow Mach number. For the cases tested here, the monopole term dominates for low frequencies over the entire range of Mach numbers studied. Both the monopole and dipole terms are significantly larger than the quadrupole

term at low frequency. At high frequencies, the quadrupole term dominates at high Mach number.

Bibliography

[1] John M. Seiner, horizontal spark schlieren of an underexpanded axisymmetric nozzle. Published in [2].

[2] John M. Seiner, "Advances in High Speed Jet Aeroacoustics," AIAA paper AIAA- 84-2275, AIAA/NASA 9th Aeroacoustics Conference, 1984.

[3] A. Powell, "On the Mechanism of Choked jet Noise," Proceedings of the Physic al Society, B, Vol. 66, pp 1039-1056, 1953.

[4] Christopher K.W. Tam, "Supersonic Jet Noise," Annual Review of Fluid Mechanics, Vol. 27, 1995.

[5] T.D. Norum and J.M. Seiner, "Broadband Shock Noise from Supersonic Jets," AIAA Journal, Vol. 20, pp.68-73, 1982.

[6] Lighthill, M.J., "On sound generated aerodynamically. I. General Theory," Proceedings of the Royal Society, A 222, pp.1-32, 1954.

[7] Ames Research Staff, "Equations, Tables, and Charts for Compressible Flow" NACA Report 1135, 1953.

[8] Farassat, F., Lecture Notes. See also his recently published paper: "Introduction to Generalized Functions with Applications in Aerodynamics and Aeroacoustics," NASA Technical Paper 3428, 1994.

[9] I.S. Gradstehyn and I.M. Ryzhik, Table of Integrals, Series, and Products, Corrected and Enlarged Edition, Academic Press, Inc., New York, pp. 402-405, 1965.

[10] J.M.Seiner and T.D. Norum, "Aerodynamic Aspects of Shock Containing Jet Plumes," AIAA-80-0965, presented at AIAA 6th Aeroacoustics Conference, Hartford, CT, 1980.

Chapter 3

Numerical Methods and Issues

3.1 Introduction

This chapter addresses numerical issues concerning the computation of sound generation in shocked flows. The direct simulation of sound generation in shocked flows is challenging because high accuracy is required to resolve the acoustic portion of the solution, while dissipation is required to maintain stability at the shock. Because shock generated sound places high demands on the algorithm, care must be exercised in the selection of the scheme used in the simulations. Two algorithms are used in the results presented in this thesis. The first is the popular MacCormack scheme which is second order accurate in time and in space. It is used as a baseline in scheme comparisons because of its computational efficiency and simplicity. MacCormack's scheme is relatively inexpensive, but Gibb's oscillations can occur in the vicinity of the moving shock, even with added artificial dissipation. MacCormack's scheme, as it is implemented in this work, is described in Section

3.2.1. The Essentially Non-Oscillatory scheme is used in most of the calculations presented in this thesis. This class of schemes is relatively new, and is not yet described in text books. It was chosen because it allows for high-order accuracy in smooth regions of the flow while minimizing oscillations around discontinuities in the solution by the use of adaptive stenciling. Second, third, fourth, and fifth order accurate implementations of the ENO scheme were used during the course of this research. The scheme is described in Section 3.2.2.

Section 3.3 deals with numerical issues regarding the calculation of shocked flows. The Gibbs' phenomenon produced by attempting to resolve a discontinuity on a finite mesh is well known, and is not described in this thesis. There is an additional oscillatory phenomenon which manifests itself when the shock wave is moving slowly relative to the mesh. This additional phenomenon has only recently been observed and described [2], and has only very recently been quantified for high-order schemes [3]. Much of the content of this section has been published by the author in [3], but is included here for completeness, with permission from the publisher.

It is well known that a high degree of accuracy is required to perform acoustic calculations. High accuracy can be obtained by using many cells (or grid points) in a low-order accurate scheme, or by using fewer cells (or grid points) in a higher-order accurate scheme. A method of determining which approach is most economical is outlined in Section 3.4. The result shows that the most economical approach depends on the degree of accuracy required. For acoustic calculations where the degree of accuracy required is on the order of 10^{-7}, the 3rd order ENO scheme proves to be most economical. Hence, this is the scheme used in most of

the calculations of Chapters 4 and 5..

Finally, Section 3.5 presents information regarding the extraction of acoustic phenomena from aerodynamic flows. The separation of acoustics from aerodynamics cannot be performed in the near field, and thus the properties of acoustic waves in the far field are given. The implications of these properties on setting up and running a calculation for sound generation are then described. Some methods of analyzing the acoustics are provided.

3.2 Algorithms

3.2.1 MacCormack's Scheme

The classical MacCormack's scheme is employed in this research because it is efficient and has been used extensively in computational aeroacoustics. (e.g. [17], [19], [18]). MacCormack's scheme is described in many textbooks (e.g. [21], [22]), but for completeness the algorithm is briefly outlined here.

Consider the system of hyperbolic equations:

$$\frac{\partial U}{\partial t} + \frac{\partial F}{\partial x} = 0 \tag{3.1}$$

where U is a vector of J components and F is a J component flux function of U. A simple example of such a system of equations is the Euler equations. MacCormack's scheme approximates the solution to Eqn. 3.1 by a two step predictor-corrector technique. For each component of the U vector, the predictor step is:

$$\bar{U}_j^{n+1} = U_j^n - \frac{\Delta t}{\Delta x}(F_{j+1}^n - F_j^n) \tag{3.2}$$

and the corrector step is:

$$U_j^{n+1} = \frac{1}{2}[U_j^n + \bar{U}_j^{n+1} - \frac{\Delta t}{\Delta x}(\bar{F}_j^n - \bar{F}_{j-1}^n) \tag{3.3}$$

where the superscript n represents the n^{th} time level, the subscript j represents the j^{th} cell, and $\bar{F}$ represents the flux function F evaluated at the predictor value $\bar{U}$.

MacCormack's scheme is second order accurate in space and in time. Analysis of the stability of MacCormack's scheme, with discussion about the amplification and dispersion factors can be found in textbooks such as [21] and [22].

MacCormack's scheme as presented in Eqns. 3.2 and 3.3 experiences difficulty maintaining stability when applied to shocked flows. Therefore, additional artificial dissipation is required. In this algorithm, artificial viscosity of the Jameson type [20] is added to the right hand side of the predictor step. The corrected numerical flux is defined by

$$F_{j+1}^n - F_j^n - F^{AV} \tag{3.4}$$

where

$$F^{AV} = \epsilon_{i+1/2}^{(2)}(U_{i+1} - U_i) - \epsilon_{i+1/2}^{(4)}(U_{i+2} - 3U_{i+1} + 3U_i - U_{i-1}) \tag{3.5}$$

and

$$\begin{aligned} \epsilon_{i+1/2}^{(2)} &= K^{(2)}(|u| + c)_i max[\nu_i, \nu_{i+1}] \\ \epsilon_{i+1/2}^{(4)} &= max[0, K^{(4)}(|u| + c)_i - \epsilon_{i+1/2}^{(2)}] \end{aligned} \tag{3.6}$$

where

$$\nu_i = \frac{|p_{i+1} - 2p_i + p_{i-1}|}{p_{i+1} + 2p_i + p_{i-1}} \tag{3.7}$$

where p is the pressure, u is the flow velocity, and c is the sound speed. In the calculations presented here, the coefficients are defined $K^{(2)} = \frac{1}{4}$ and $K^{(4)} = \frac{1}{256}$.

The pressure term in $\epsilon^{(2)}$ is generally of second order in smooth regions of flow, the $\epsilon^{(4)}$ term dominates, and the artificial dissipation is fourth order. Near discontinuities, however, the pressure term reduces to zeroth order, the $\epsilon^{(2)}$ term dominates, and the artificial dissipation is second order.

3.2.2 ENO Scheme

The class of ENO schemes is relatively new [7], and is chosen because high accuracy is achieved in smooth portions of the flow, while spurious oscillations around flow discontinuities such as shocks are bounded. A brief discussion of the properties of ENO schemes is given below, but interested readers are referred to the references [7] and [8] for details.

An ENO solution operator E_h is r^{th} order accurate in the sense of local truncation error

$$E_h U^n = U^{n+1} + O(h^{r+1}) \tag{3.8}$$

where $U(x)$ is the sufficiently smooth exact solution, and h is the cell spacing. The distinguishing property of ENO schemes is that spurious oscillations near discontinuities in U are bounded. For the one-dimensional scalar case, this can be written:

$$TV(E_h U) = TV(U) + O(h^{1+q}) \tag{3.9}$$

for some $q > 0$, where $TV(U)$ is the total variation of U as a function of x, defined as $TV(U) = \sum_i |U_{i+1} - U_i|$ for a discrete solution to a scalar conservation law.

Bounding oscillations near discontinuities is accomplished in ENO schemes

through the use of an adaptive stencil. Because the stencil used for discretizing the differential equations adapts to the solution, schemes based on the ENO property may be thought of as adaptive filters or non-linear algorithms.

ENO schemes minimize numerical oscillations around discontinuities by using data from the smoothest part of the flow. At each cell, a searching algorithm determines which portion of the surrounding flow is smoothest. The stencil spanning this portion of the flow is then used to construct a higher order accurate, conservative interpolation to determine the variables at the cell interfaces.

In this particular finite-volume implementation, the interpolation operator is applied to the cell averaged characteristic variables, and the accuracy in space and in time is third order. Time integration is accomplished by the use of a third order, three stage Runga-Kutta scheme discussed by Shu [8]. The algorithm is applied to the conservation law form of the equations so that shocks are captured in the computations and no shock fitting is required to enforce the Rankine-Hugoniot jump relations across shocks which appear in the solution.

3.2.3 Stencil Biasing Parameters

ENO schemes can achieve high-order accuracy in smooth regions and capture shocks without oscillations by the use of adaptive stenciling. As the ENO schemes were originally presented in [7], the stencil shifts freely due to any detection of a numerical gradient. The direction of the stencil shift is determined by the magnitudes of the neighboring divided differences. The stencil shifts away from the larger differences. However, a loss of accuracy can occur when this freely adaptive algorithm is used [10] [9]. Shu [11] has suggested that the stencil be biased towards a preferred stencil, the one that makes the scheme stable in the sense of

linear stability analysis. The stencil is allowed to shift only when one neighboring difference is larger than the other by some factor. This factor will be referred to as the "bias" parameter.

This biasing can be accomplished by implementing a factor in the search stencil. To explain how biasing is used to affect the stencil, let Δ_i^k denote the operator that yields the $k-th$ forward difference on a stencil of $k+1$ cells with a left-most index i, which is defined recursively by:

$$\begin{aligned} \Delta_i^1 \bar{u} &= \bar{u}_{i+1} - \bar{u}_i \\ \Delta_i^k \bar{u} &= \Delta_{i+1}^{k-1} \bar{u} - \Delta_i^{k-1} \bar{u}, \quad k = 2, 3, ... \end{aligned} \tag{3.10}$$

The algorithm begins by setting $j^1(i) = i$. This one-cell stencil results in a piecewise constant reconstruction that is spatially first order accurate. In order to choose $j^{k+1}(i), k = 1, ...r-1$, the two stencils considered as candidates are those obtained by annexing a cell to the left or right of the previously determined cell. The stencil which is selected is the one in which the $k-th$ difference is smaller in magnitude:

$$j^{k+1}(i) = \begin{cases} j^k(i) - 1, & \text{if } \sigma_L |\Delta_L^k \bar{u}| < \sigma_R |\Delta_R^k \bar{u}| \\ j^k(i), & \text{otherwise.} \end{cases}$$

where $\Delta_L^k \bar{u}$ and $\Delta_R^k \bar{u}$ are the k-th differences obtained by annexing the cell to the left or right of the previously determined stencil, respectively, $(\sigma_L, \sigma_R) = (1, \bar{\sigma})$ or $(\bar{\sigma}, 1)$ for biasing to the left or right, respectively, with $\bar{\sigma} > 1$.

Even when a bias parameter is used, there may be a loss of accuracy when all the numerical gradients in a region are small, but some are orders of magnitude larger than others. Atkins [12] has suggested the use of another parameter, which serves as a threshold, to force the shift to the preferred stencil whenever neighboring

differences are small, regardless of their relative magnitudes. This parameter will be referred to as the "threshold" parameter.

The threshold parameter is implemented as

$$\text{if} |\Delta_L^k \bar{u}| < \epsilon \quad \text{and} |\Delta_R^k \bar{u}| < \epsilon \quad \text{then} \quad j^{k+1}(i) = j_S^{k+1}(i) \tag{3.11}$$

where ϵ is a small parameter and $j_S^k(i)$ identifies the stencil obtained by annexing the $k-th$ cell in the linearly stable direction.

Research regarding the appropriate stencil biasing parameters is on-going [16]. However, the results presented in this thesis used the definitions cited in the articles of [12] and [11].

3.2.4 ENO Flux Computation

ENO schemes of Godonov type rely upon the solution of the Riemann problem to calculate numerical fluxes. Two methods of computing the fluxes across the cell interfaces are evaluated in this thesis. The first is due to Roe [13], and the second is due to Osher [14].

Consider a system of hyperbolic equations,

$$\frac{\partial U}{\partial t} + \frac{\partial F}{\partial x} = 0 \tag{3.12}$$

where U is a vector of J components, and F is a J component differentiable function of U.

Roe's approximate Riemann solver determines the change in flux by finding a mean Jacobian matrix $\tilde{A}$ which satisfies:

$$\Delta F = \tilde{A} \Delta U \tag{3.13}$$

where Δ represents the difference between any two states in solution space. The matrix $\tilde{A}$ is required to have a complete set of right eigenvectors and reduce to the exact Jacobian when the states to the left and the right are equal: $\tilde{A}(U,U) = \frac{\partial F}{\partial U}(U)$. If $\tilde{\lambda}_{(j)}$, $\tilde{r}^{(j)}$, and δw_j are the jth eigenvalue, right eigenvector and inner product of the jth left eigenvector with ΔU, respectively, the Eqn. 3.13 can be written:

$$\Delta F = \sum_{j=1}^{J} \tilde{r}^{(j)} \tilde{\lambda}_{(j)} \delta w_j \tag{3.14}$$

The flux at the cell interface is written:

$$f = \frac{1}{2}(F_L + F_R) - \frac{1}{2} \sum_j |\tilde{\lambda}_{(j)}| \delta w_j \tilde{r}^{(j)} \tag{3.15}$$

where F_L and F_R are the values of the fluxes to the left and right of the interface, respectively. Roe gives the expressions for $\tilde{\lambda}$, $\tilde{r}$ and δw_j for the Euler equations in [13].

Osher's approximate Riemann solver computes fluxes in state space rather than physical space. The flux difference between the left and right states is written:

$$\Delta F = \int_{U_L}^{U_R} \frac{\partial F}{\partial U} dU \tag{3.16}$$

where the integral is evaluated along an arbitrary path Γ in state space.

The flux at the cell interface is given by:

$$f = \frac{1}{2}(F_L + F_R) - \frac{1}{2} \sum_j \int_{\Gamma(j)} |\lambda_{(j)}| r^{(j)} dU \tag{3.17}$$

The evaluation of the integral in Eqn. 3.17 requires knowledge of the states along each subpath $\Gamma(j)$ and any sonic states that occur. Osher and Solomon [14] solve for these states explicitly for the Euler equations.

3.3 Numerical Error Generated by a Slowly Moving Shock in a Duct

3.3.1 Introduction

The numerical treatment of unsteady shocks is challenging. In addition to the usual concerns of stability and accuracy, there are conflicting requirements regarding the calculation of the shock region. On one hand, it is desirable to resolve the shock crisply by minimizing the smearing effect of artificial dissipation at the shock. On the other hand, some artificial dissipation is required at the shock to minimize or eliminate the oscillations which occur when attempting to resolve a discontinuity on a finite mesh. The Gibbs phenomenon produced by attempting to resolve a discontinuity on a finite mesh is well known, has been discussed widely in relation to steady shock calculations, and will not be addressed here. There is an additional oscillatory phenomenon which can manifest itself in the computation of slowly moving shocks. This additional oscillation resulting from the unsteady nature of slowly moving shocks has only recently been discussed in the literature [1] [2] [4], and is investigated here to determine the nature of the spurious oscillations and the effect that these spurious numerical oscillations have on computing sound.

In order to simplify the analysis and better isolate difficulties in the numerical calculations, only one dimensional and quasi-one dimensional flows will be treated here. Thus, vorticity waves will not appear and emphasis will be on predicting the acoustic and entropy waves. The model problem to be investigated is a shock moving at a constant velocity in a one-dimensional flow field.

Spurious oscillations in unsteady computations of slowly moving shocks have been described by Woodward and Collela [1], who observed the oscillations in com-

putations of high-pressure ratio ($p_2/p_1 > 10^5$) shocks. These oscillations appear when the speed of the shock, relative to the mesh, is small compared to the maximum flow speed at the shock. Woodward and Collela suggested that additional numerical dissipation be added to the scheme at the shock, and explained that the reason for this spurious numerical behavior is that the shock transition layer alternates between being thick and thin as it passes through the mesh. Roberts [2] has noted that the oscillation phenomenon is not observed in discontinuous solutions of *scalar* equations. Roberts explains the oscillation in terms of the discrete shock structure and shows that among first order flux difference splitting schemes, Osher's approximate Riemann solver provides the smallest oscillations because the unsteady nature of the numerical shock structure in state space most closely approximates the true shock structure. Roberts observed the spurious oscillation phenomenon in calculations for shock pressure ratios as low as 1.2 in calculations using first order flux-difference splitting schemes. Lindquist and Giles [4] observed spurious oscillations in computations using a Jameson style Runge-Kutta scheme with blended second- and fourth-difference artificial dissipation and also with a van-Leer flux vector splitting algorithm for shock pressure ratios $1.5 < p_2/p_1 < 2.1$. They described the oscillations in terms of the changing shock shape as the shock traverses the computational mesh, and found, as did Woodward and Collela, that the spurious oscillations could be reduced by smearing the shock over more computational cells.

Spurious oscillations have been observed during the course of this research in computations using the classical MacCormack scheme, a recently developed high-order accurate Essentially Non-Oscillatory (ENO) scheme, and a recent imple-

mentation of Jameson's Runge-Kutta scheme which employs a symmetric Total Variation Diminishing (TVD) matrix dissipation. Because the interest here is to compute sound generated by shocks and shock-fluid interactions, artificial dissipation is not explicitly increased over the solution domain because of the deleterious effect on the generation and propagation of sound in the solution. This has created some difficulties because the spurious oscillations are preserved in the high-order accurate flow computations.

ENO schemes of Godunov type rely upon the solution of the Riemann problem for the calculation of numerical fluxes. The effect that two Riemann solvers have on the spurious oscillations will be described in this thesis. In addition, because ENO schemes use an adaptive stencil to reduce spurious oscillations, modifications of this adaptive procedure will be examined. Finally, the effects of shock pressure ratio, Courant number, grid spacing, and shock speed on the amplitude and frequency of the spurious numerical oscillations will be described.

3.3.2 Analysis: Exact Solution

The governing equations for the inviscid, compressible flow in a constant area duct are assumed to be the one-dimensional Euler equations,

$$\frac{\partial U}{\partial t} + \frac{\partial F}{\partial x} = 0 \tag{3.18}$$

where U is the vector of conserved variables $[\rho,\ \rho u,\ \rho e]^T$, and F is the flux vector, $[\rho u,\ \rho u^2 + p,\ (\rho e + p)u]^T$. Standard notation is used; ρ is density, u is velocity, e is total energy per unit mass, and p is pressure.

Consider these equations along the duct length $0 \leq x \leq L$ for $t > 0$, with the

initial condition:

$$U(x,0) = \begin{cases} U_1 & x < x_s \\ U_2 & x > x_s \end{cases} \tag{3.19}$$

where the constant states 1 and 2 represent the flow upstream and downstream of a shock, respectively, and x_s is the shock position.

If these equations are integrated along the duct, one obtains:

$$\frac{d}{dt}\int_0^L U dx + F(U(L,t)) - F(U(0,t)) = 0 \tag{3.20}$$

One solution is the trivial case, $U_1 = U_2$. The non-trivial solution to this equation with the initial condition 3.19 is a flow field with a shock moving at constant velocity, u_s, which satisfies

$$F(U_2) - F(U_1) = u_s(U_2 - U_1) \tag{3.21}$$

Eqn. 3.21 follows directly from Eqn. 3.20 for constant area states on either side of the shock. The solution $U_1 = U_2$ also satisfies Eqn. 3.21.

3.3.3 Results

The unsteady, compressible, inviscid flow in the duct is solved by numerical integration of the one dimensional Euler equations. All variables in the supersonic flow field at the inflow boundary are prescribed. The static pressure at the downstream (subsonic) boundary is prescribed. Variables are normalized by the duct length, stagnation pressure and stagnation sound speed. Control over the shock velocity is obtained by making a transformation $u = u - u_s$, where u_s is the prescribed shock velocity, so that a positive shock velocity moves the shock to the left of the computational domain.

Computations have been performed over a range of shock pressure ratios and shock speeds, but in the interest of brevity, only one typical calculation is shown

here. The calculations were performed on a 512-cell grid at a Courant number of 1. Unless noted otherwise, calculations are performed using Roe's flux solver and both the bias parameter and threshold parameter are 'on', meaning that the stencil is biased towards the preferred one, and a threshold limit is set. The values of the biasing parameters used in these calculations, referring to Equations 3.2.3 and 3.11, are $\bar{\sigma} = 2$ and $\epsilon = 10^{-3}$. Figure 3.1 illustrates the spurious oscillations observed with the 3rd order ENO scheme for a case in which the pressure ratio across the shock is 10.333 and the shock is moving to the left at a speed of 0.05. Figure 3.1 shows the pressure and entropy distributions in the duct after the shock has moved 15 percent of the duct length. Entropy is measured by the quantity $s = \frac{p}{\rho^\gamma}$. Although there were no oscillations at the shock in the initial shock position, once the shock begins to move, spurious waves develop in the flow solution. The oscillation is seen primarily in the entropy wave; the pressure wave is relatively unaffected.

The spurious error is due to the discrete motion of the shock moving through the mesh. When the shock is located at a cell interface, it is extremely thin. As it moves through the cell interior, it smears out, weakens in strength, and entropy and pressure waves convect downstream. If the "shock passing frequency" is defined as the frequency associated with the shock passing through a cell,

$$f_{shock} = \frac{u_s}{\Delta x} \tag{3.22}$$

where Δx is the grid spacing, and u_s is the shock speed relative to the grid, the wavelengths associated with the pressure and entropy waves, λ_p and λ_s, are determined by

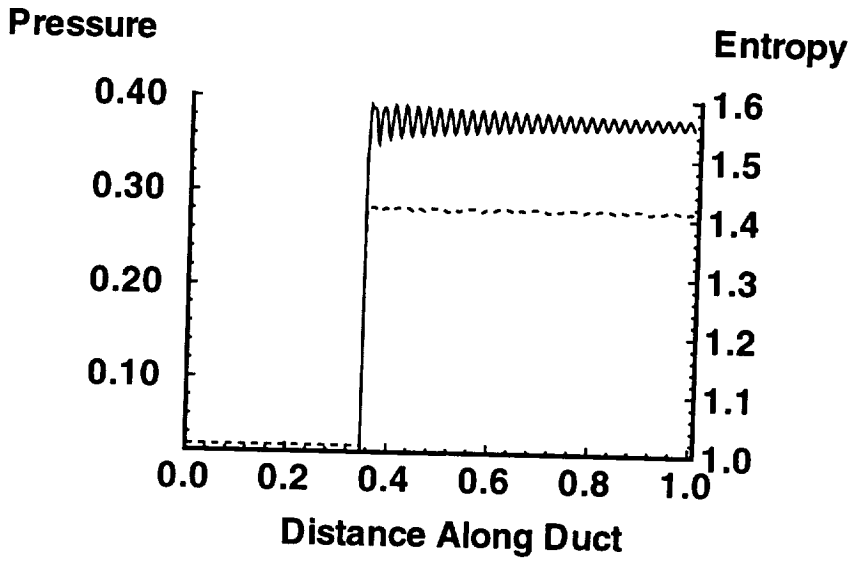

Figure 3.1: Pressure and Entropy as Functions of Distance along Duct. Shock Speed = .05; Shock Pressure Ratio = 10.33. Dashed line represents pressure. Solid line represents entropy.

$$\lambda_p = \frac{(u_2 + a_2)}{f_{shock}} = \frac{(u_2 + a_2)\Delta x}{u_s} \tag{3.23}$$

$$\lambda_s = \frac{u_2}{f_{shock}} = \frac{u_2 \Delta x}{u_s} \tag{3.24}$$

where u_2 and a_2 are the downstream velocity, relative to the shock, and sound speed, respectively. When adequately resolved on the mesh, the spurious pressure and entropy waves measured in the numerical computations compare well with the wavelengths λ_p and λ_s described by the above equations. For example, the wavelength λ_s of the entropy wave in Figure 3.1 is computed: $\lambda_s \approx .550 * .00195/0.05 \approx .021$. Inspection of Figure 3.1 verifies this result.

A series of calculations, for the same $p_2/p_1 = 10.333$ shock strength, illustrates

the effect of shock speed on the behavior of the spurious oscillations. These calculations were performed on a 512-cell grid at a Courant number of 1.0. Figure 3.2 shows the entropy distributions in the tube after the shock has moved to the left for a normalized time of 3.0 for shock speeds of 0.02, 0.05 and 0.15. For clarity, the entropy distributions are offset by a constant value of 0.1. The entropy upstream of the shock is 1.0. The wavelengths of the perturbations downstream of the shock are consistent with Equation 3.24. The long wavelength disturbances at the lowest shock speeds are only slightly damped downstream of the shock, while the short wavelength disturbances at high shock speeds are damped very quickly by the dissipation in the scheme. This, of course, explains why these disturbances are not seen when the shock speed through the mesh is comparable to the flow speed.

Figure 3.3 shows the pressure distributions in the tube after the shock has moved to the left for a normalized time of 3.0 for shock speeds of 0.02, 0.05 and 0.15. For clarity, the pressure distributions are offset by a constant value of 0.05. The pressure upstream of the shock is approximately 0.027. Small perturbations are visible in the pressure distribution downstream of the shock, and the wavelengths of these perturbations are consistent with Equation 3.23. The long wavelength disturbances at the lowest shock speeds are only slightly damped downstream of the shock, while the short wavelength disturbances at high shock speeds are damped very quickly by the dissipation in the scheme.

Effect of Shock Speed

Figure 3.4 summarizes the effect of the shock velocity relative to the grid on the maximum amplitude of the spurious entropy. The ratio of the magnitude of maximum zero-to-peak entropy error amplitude to the jump in entropy across the shock

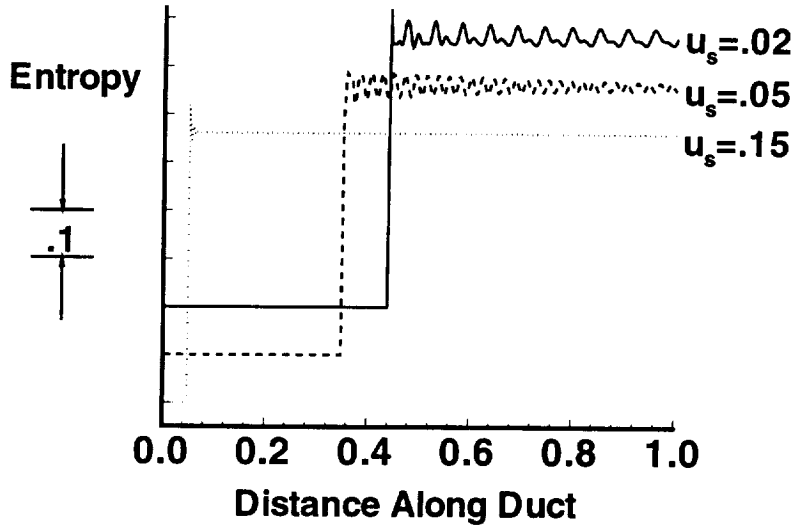

Figure 3.2: Entropy as a Function of Distance along Duct and Shock Speed. Shock Speeds = .02, .05, 0.15; Shock Pressure Ratio = 10.33.

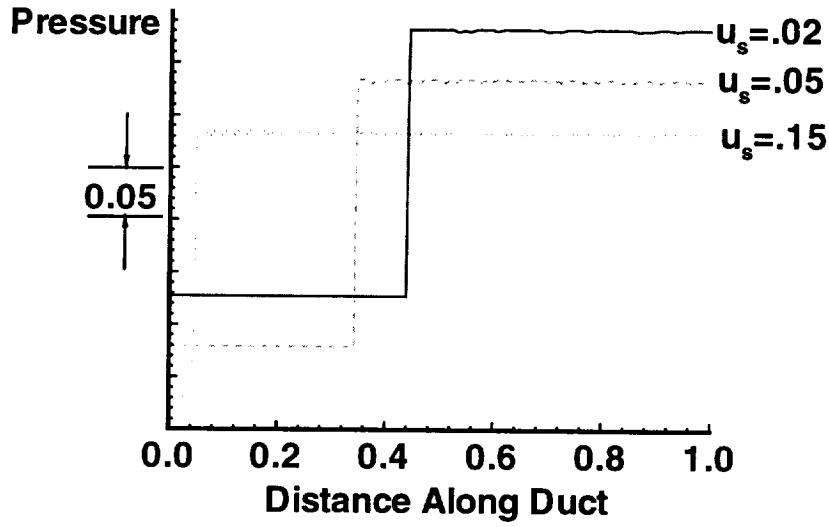

Figure 3.3: Pressure as a Function of Distance along Duct and Shock Speed. Shock Speeds = .02, .05, 0.15; Shock Pressure Ratio = 10.33.

is plotted as a function of the ratio of the shock velocity (normalized by upstream stagnation sound speed) to upstream Mach number. These calculations were performed for a shock moving to the right at shock speeds from 0 to 5.0 on a 256 cell mesh. The spurious entropy amplitude is machine zero when the shock is stationary relative to the grid, increases to a maximum when $.005 < \frac{u_s}{M} < 0.1$, and decreases as the ratio of $\frac{u_s}{M}$ increases further.

Figure 3.5 summarizes the effect of the shock velocity relative to the grid on the maximum amplitude of the spurious pressure. The ratio of the magnitude of maximum zero-to-peak pressure error amplitude to the shock strength is plotted as a function of the ratio of the shock velocity (normalized by upstream stagnation sound speed) to upstream Mach number. These calculations were performed for a shock moving to the right at shock speeds from 0 to 5.0 on a 256 cell mesh. The results show that the maximum pressure amplitude is relatively independent of the shock speed, and that the maximum error in the downstream pressure relative to the shock strength is less than 0.15 percent for all of the cases studied.

Figure 3.6 shows the zero-to-peak pressure error at a location approximately 50 cells downstream of the shock. This figure shows that for faster moving shocks, the amplitude of the pressure error is more rapidly damped. This is consistent with the observations made regarding Figure 3.3, which relates the wavelength of the spurious pressure with the shock speed.

Because the amplitude of the error introduced by a slowly moving shock is manifest primarily in entropy, further discussion will focus on this flow variable.

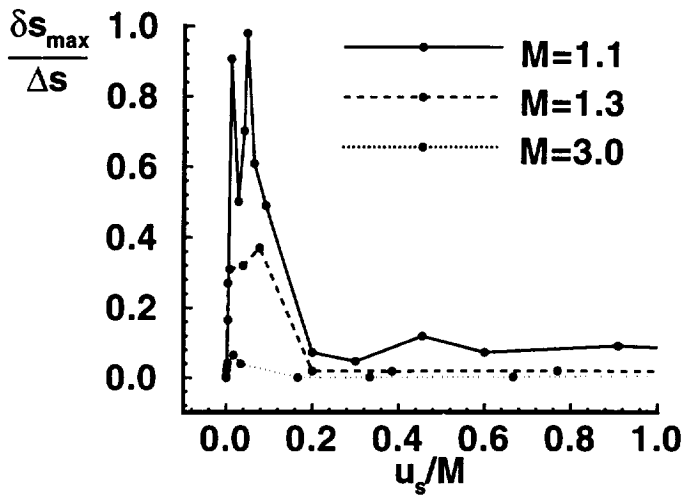

Figure 3.4: Effect of Shock Velocity on Spurious Entropy. Three shock strengths are shown.

Effect of Shock Strength

Figure 3.4 also illustrates that the magnitude of the maximum spurious entropy amplitude is a function of shock pressure ratio. As the shock strength increases, the magnitude of entropy error, relative to the static entropy jump, decreases. In the weak shock case, $M = 1.1$, the spurious oscillations are close to 100% of the static jump in entropy over a range of shock speeds. This is because for the weak shock cases, the entropy jump across the shock is very small.

The absolute levels of maximum entropy error are actually orders of magnitude higher for the higher Mach number flows. For example, at $\frac{u_t}{M} = 0.04$, the absolute levels of maximum entropy error are $\delta s_{max} = 0.00033$, 0.0039, and .097 for Mach numbers $M = 1.1$, 1.3, and 3.0, respectively.

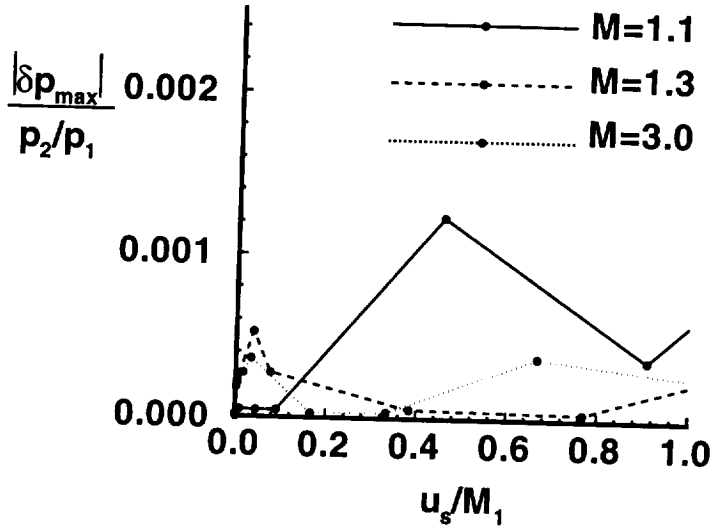

Figure 3.5: Effect of Shock Velocity on Spurious Pressure. Three shock strengths are shown.

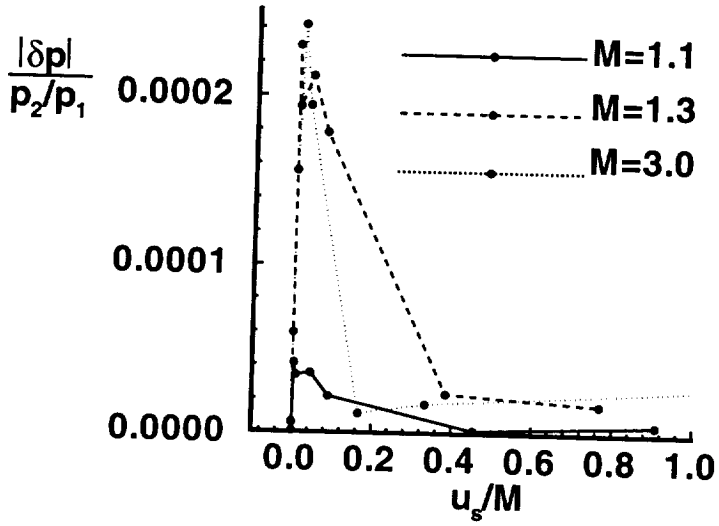

Figure 3.6: Effect of Shock Velocity on Spurious Pressure. The error is measured approximately 50 cells downstream of the shock. Three shock strengths are shown.

Effect of Courant Number

A sequence of calculations was performed with Courant numbers between 0.1 and 1.0 (the stability limit) to determine the effect of Courant number on the spurious entropy. Neither the amplitude nor the wavelength of the spurious oscillations is found to be sensitive to the Courant number. This is consistent with the results reported by Roberts for flux-difference splitting schemes [2].

Effect of Stencil Biasing Parameters

In this section the effects of the stencil biasing parameters on the spurious entropy are investigated. To illustrate the effects of these parameters on the algorithm, Figure 3.7 shows a space-time diagram of the stencil used in the ENO algorithm for four combinations of stencil biasing parameters: (a) threshold on, bias on, (b) threshold off, bias on, (c) threshold off, bias off, and (d) threshold on, bias off. For clarity, the space time diagrams are limited to the region near the shock, and the total number of cells in the computations was reduced to 256. The shock is initially located at $x = .5$ and moves with a velocity of .01 to the left. The upstream Mach number is 1.3. For cases (a) and (d), the threshold is on, and a centered stencil is used for the majority of the computational space. The centered stencil is the linearly stable stencil in this case. Cells on either side of the shock use downwind or upwind stencils as appropriate. For cases (b) and (c), the threshold parameter is off, and there is a great deal more stencil shifting in the smooth regions of the flow. It is interesting to note that the stencils in these two figures follow entropy and acoustic wave paths downstream of the shock. The stencil traces for these wave paths have slopes corresponding to acoustic and convecting wave speeds.

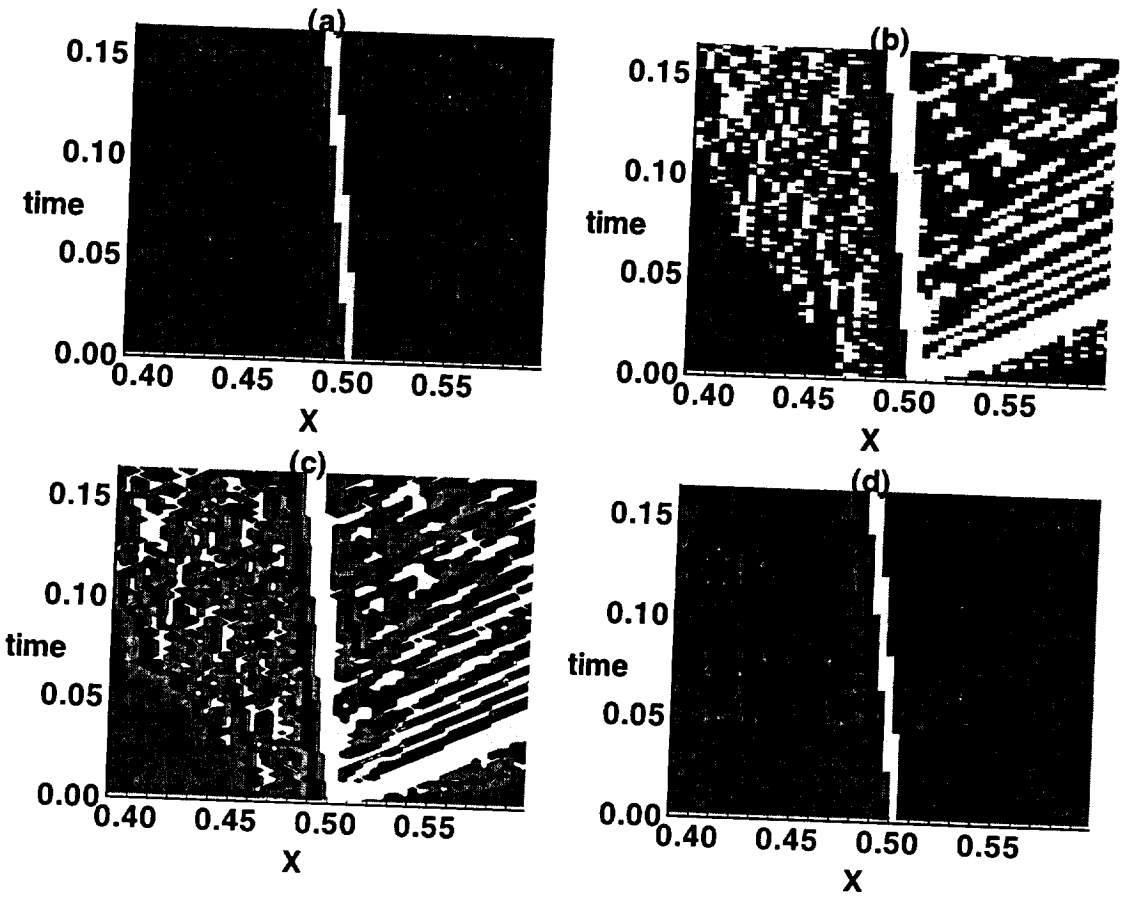

Figure 3.7: Effect of Stencil Biasing Parameter and Threshold Parameter on Stencil. White represents a downwind stencil; Black represents an upwind stencil; Gray represents a centered stencil. Case(a): Biasing on, Threshold on; Case(b): Biasing on, Threshold off; Case(c): Biasing off, Threshold off; Case(d) Biasing off, Threshold on. 256 Cells.

Effect of Mesh Spacing

The effect of the mesh spacing is illustrated by comparing Figures 3.8 and 3.9. The results presented in Figures 3.8 and 3.9 are for a shock (upstream Mach number is 1.3) moving to the left at a speed of $u_s = 0.01$. The difference in the results occurs because of the difference in discretization. A 256 cell mesh is used to obtain the results of Figure 3.8, but a 1024 cell mesh is used to obtain the results of Figure 3.9. The entropy distributions in Figures 3.9 and 3.8 are offset by a constant of .0075 and the numerical values of entropy are removed from the vertical axis for clarity. The difference between tick marks is .005. Refining the mesh reduces the magnitude of entropy oscillation, and shows the effect of the biasing parameters more distinctly. Each combination of biasing parameters has a unique spurious entropy pattern. Case (a) is highly oscillatory, with multiple frequencies per wavelength of the oscillation. Case (b) has the smallest amplitude of entropy peaks. Case (c) has the fewest peaks per period of spurious oscillation, but the amplitude of the largest peak is high. Case (d) has large entropy peaks as well as multiple frequencies per oscillation. Although all of the results show significant entropy error, the results obtained by biasing the stencil and turning the threshold off (case (b)) provide the lowest amplitude of entropy error.

Another effect of the mesh spacing is the reduction in the wavelength of the spurious entropy. In Figure 3.8, the wavelength of spurious entropy computed by Eqn. 3.24 is $\lambda_s \approx .34$. Refining the mesh in Figure 3.9 reduces this wavelength to $\lambda_s \approx .086$. The number of points per wavelength of the spurious entropy wave is the same for both computations, since $\frac{u_2}{u_s}$ is constant.

Figure 3.10 is included to show the effect of the Osher flux solver on the spurious

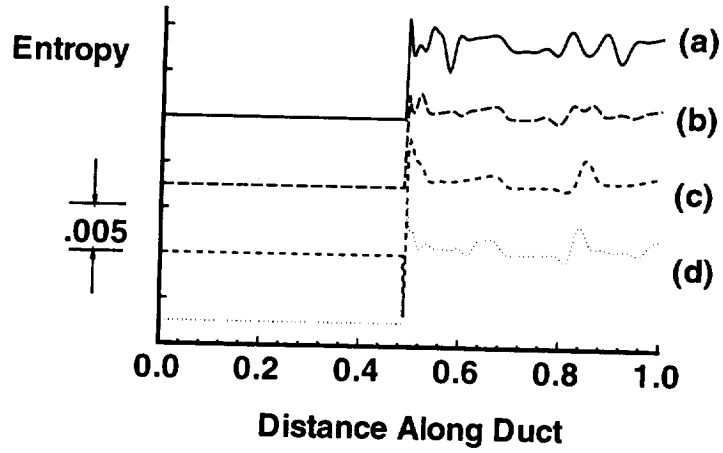

Figure 3.8: Entropy as a Function of Duct Distance for Various Combinations of Biasing and Threshold Parameters. Case(a): Biasing on, Threshold on; Case(b): Biasing on, Threshold off; Case(c): Biasing off, Threshold off; Case(d) Biasing off, Threshold on. 256 Cells.

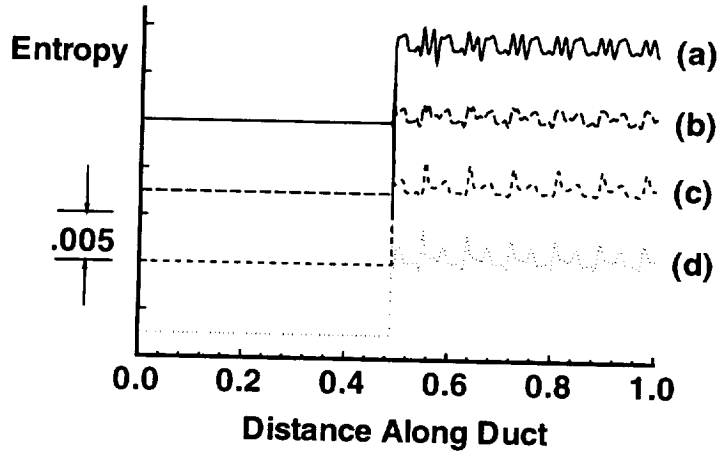

Figure 3.9: Entropy as a Function of Duct Distance for Various Combinations of Biasing and Threshold Parameters. Case(a): Biasing on, Threshold on; Case(b): Biasing on, Threshold off; Case(c): Biasing off, Threshold off; Case(d) Biasing off, Threshold on. 1024 Cells.

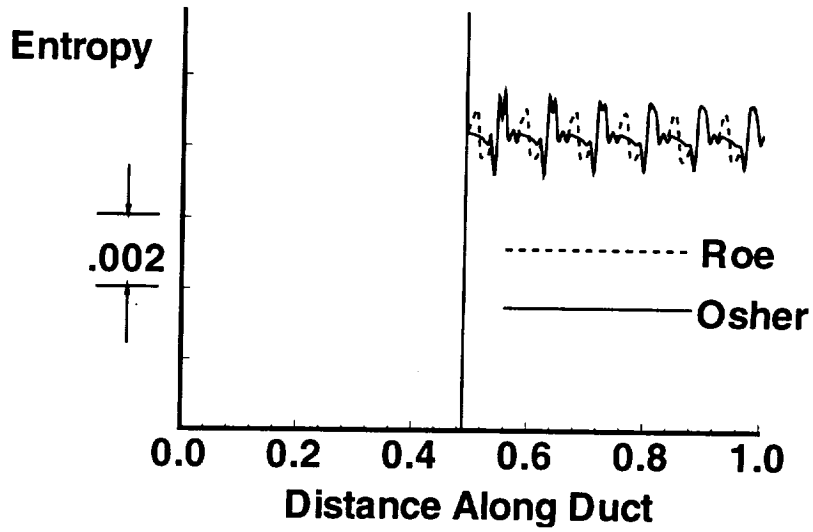

Figure 3.10: Entropy as a function of Distance Along Duct Length for Roe and Osher Flux Solvers. Biasing on, Threshold off.

entropy. The result is shown only for case (b) because other cases provided similar results. The effect of the Osher solver on the spurious entropy is to remove one of the peaks (seen in the Roe solver results) in the entropy wave each oscillation wavelength.

This section has illustrated numerical difficulties in computing slowly moving shocks. Although changes in flux computation, algorithmic parameters, and Courant number were made in an effort to remove these spurious entropy waves, they persisted.

Calculations of supersonic jet noise will often have shocks moving slowly relative to the grid. Although the results presented thus far have shown that spurious entropy exists in calculations with slowly moving shocks, it has also been noted that spurious pressure waves are very small in amplitude.

3.3.4 Summary

The computation of slowly moving shock waves produces spurious, numerical entropy. The spurious entropy is a function of the algorithm used in the calculation, and, as seen by the modifications made to the ENO scheme, even slight changes in a basic algorithm can produce marked changes in the structure of the spurious entropy. It is interesting to note that this phenomenon has been observed by the authors in implementing the MacCormack scheme, ENO schemes, and a matrix dissipation Runge-Kutta scheme, and by others using flux vector splitting schemes [4], flux-difference splitting schemes with Gudonov, Roe and Osher flux solvers [2], and PPM methods [1]. Spurious entropy normalized by the entropy jump across the shock decreases with increasing shock strength and increasing shock velocity, but is insensitive to Courant number. The amplitude of spurious entropy perturbations is relatively unaffected by the type of flux solver used, but the Osher solver reduces the number of peaks in the spurious entropy wave form.

Because the amplitude of the spurious entropy wave is a function of the shock speed relative to the grid, the obvious method of eliminating the spurious wave is to move the computational grid with the shock during the calculation. Although this is not difficult in one-dimensional problems, it is considered unreasonable for the multi-dimensional problems of practical interest, and was not implemented during the course of this research. Another approach to reducing the spurious entropy is to increase the dissipation of the algorithm, as suggested by Woodward and Collela. This was not implemented, because the added dissipation would affect the acoustic waves as well as the entropy. Acoustic pressure waves seem to be less sensitive to numerical errors generated by slowly moving shocks.

3.4 Economics of Higher-Order Schemes

The desired accuracy in a computational solution determines whether it is more economical to use a second order scheme with many grid points or a high-order scheme with fewer grid points. Figure 3.11 illustrates how the cost of implementing these algorithms, as measured by CPU seconds per time step, varies as a function of the solution error. This figure is constructed in the following manner. The quasi-one dimensional Euler equations are solved for the nozzle problem described in detail in Chapter 4. Grid refinement studies for the 2nd, 3rd, and 4th order ENO algorithms are performed on a Cray-2 computer. For each successively refined spatial discretization, the error in Mach number is computed for a steady isentropic flow in a converging-diverging nozzle. In addition, CPU time per time step is measured for the solution on each mesh. The relationships of error and CPU time as functions of grid spacing are then combined to construct the figure. The symbols on Figure 3.11 represent numerical results from the grid refinement studies. The lines are extrapolations of the numerical results over the error range of interest. Because the temporal and spatial accuracy properties are equivalent for these algorithms, the trends presented in Figure 3.11 will be similar whether the accuracy computations are performed on steady or unsteady flows. The error in Figure 3.11 is measured in the L_1 norm, defined by:

$$\frac{\sum_{n=1}^{N} |M(x_n) - \hat{M}(x_n)|}{N} \tag{3.25}$$

where $M(x)$ is the exact value, $\hat{M}(x)$ is the numerical approximation, and N is the number of discrete values in the numerical solution.

Figure 3.11 shows that when an error of order 10^{-1} is acceptable, the second

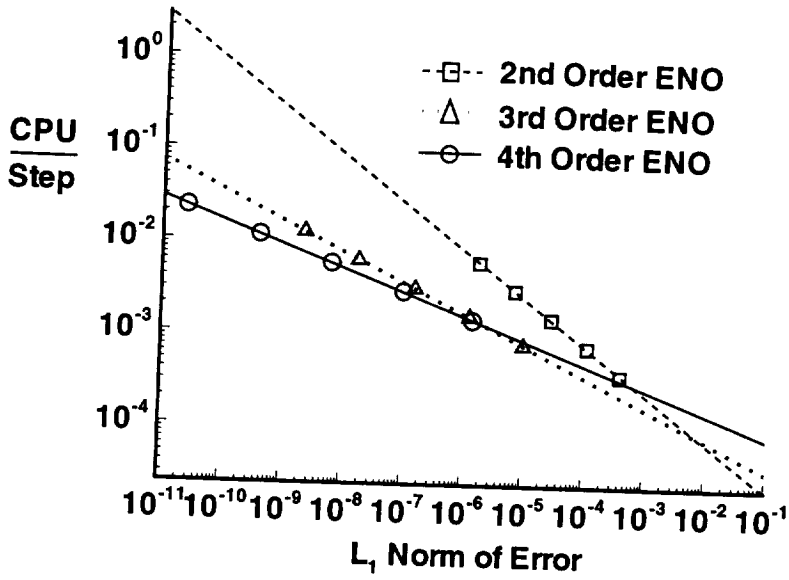

Figure 3.11: Computational Time per Time Step as as Function of L_1 Error for 2nd, 3rd, and 4th Order ENO Schemes.

order scheme is more efficient than the fourth order scheme by almost an order of magnitude. If, on the other hand, an error on the order of only 10^{-6} is acceptable, then the higher order schemes are an order of magnitude more efficient. It is interesting to note that continually increasing the order of accuracy in a scheme does not necessarily result in a significant reduction in CPU time, even at very low acceptable levels of error. Figure 3.11 shows that for the ENO scheme, most of the benefit is realized in moving from second to third order in the range of error norms considered.

It should be noted that the results of Figure 3.11 are particular to the quasi-one dimensional ENO algorithms used in this study. Figure 3.11 will not apply to the implementation of all schemes, because the relative cost of obtaining high-order accuracy for different algorithms will vary. However, the procedure for determining

the relationship of computer cost as a function of acceptable error for different algorithms will be the same.

3.5 Extracting Acoustics from Aerodynamic Flow

3.5.1 Acoustics Defined

In order to be able to extract acoustics from an aerodynamic flow, it is important to define the characteristics of the acoustic waves. For the purposes of this paper, acoustic waves have the following characteristics:

(1). Acoustic waves propagate to the far field at the sum of the local velocity and sound speeds.

(2). Acoustic waves are isentropic.

(3). Acoustic waves are small amplitude.

(4). Acoustic waves maintain constant power. Thus, the decay in pressure of acoustic waves corresponds to geometric spreading losses. This implies that acoustic pressure decays proportional to $\frac{1}{r}$ in three dimensional flows and $\frac{1}{\sqrt{r}}$ in two dimensional flows; there is no decay in pressure amplitude in one-dimension. (Note that these decay properties are valid when wave steepening is negligible. The spreading characteristics of nonlinear waves are discussed in Whitham's text[24].)

These characteristics of acoustic waves can be readily measured in the far field where the amplitudes of the acoustic disturbances dominate those of the "hydrodynamic" (non-propagating) disturbances; however, the application of these definitions near the source become more difficult. In fact, separating the acoustic disturbances from the hydrodynamic disturbances in the acoustic near field is not

considered to be possible because these quantities do not exist independently [23]. Both hydrodynamic and acoustic disturbances are heard by a near field observer, but because the hydrodynamic disturbances decay more rapidly with distance from the source than the acoustic disturbances, only the acoustic disturbances impact the far field.

3.5.2 Requirements for Acoustic Calculations

The characteristics of acoustic disturbances determine the requirements of the direct numerical simulations used:

(1). Highly-accurate. The small amplitude of the acoustic waves relative to the underlying mean flow and the large distances the acoustic waves travel require that the numerical scheme used is high-order accurate and/or uses a grid fine enough to sufficiently resolve the acoustic waves. The disparity of length and time scales typically of importance in acoustics makes accuracy a real issue, since small scales are often important and cannot afford to be filtered from the computational solution. In addition, boundary conditions must be accurately imposed.

(2). Large computational domain. Because acoustic disturbances are defined as the propagating portion of the unsteady pressure field, calculation of acoustics requires a large computational domain. The size of the computational domain must be large enough that the pressure field can be measured at least one acoustic wavelength away from the source. Acoustic wavelengths are often much larger than the source(s) which generate the sound.

(3). Long time solution. Long time calculations are necessary to compute at least one period of the far field sound if the acoustic signal is periodic. For non-periodic signals, seven to ten cycles of the lowest frequency are required for reasonably accu-

rate spectral estimates. (For a good description of accuracy in spectral estimates, see Hardin's text [25].)

Bibliography

[1] P. Woodward and P. Collela, "The Numerical Simulation of Two-Dimensional Fluid Flow Through Shocks," Review Article, Journal of Computational Physics, Vol. 54, pp. 115-173, 1984.

[2] Thomas W. Roberts, "The Behavior of Flux Difference Splitting Schemes Near Slowly Moving Shocks," Journal of Computational Physics, Vol. 90, pp. 141-160, 1990.

[3] Kristine R. Meadows, David A. Caughey, and Jay Casper, "Computing Unsteady Shock Waves for Aeroacoustic Applications," AIAA Journal, Volume 32, Number 7, pp. 1360-1366, July 1994.

[4] Dana R. Lindquist and Michael B. Giles, "On the Validity of Linearized Unsteady Euler Equations with Shock Capturing," AIAA paper 91-1598-CP, presented at the AIAA 10th Computational Fluid Dynamics Conference, June 24-26, Honolulu, Hawaii, 1991.

[5] P. Jorgenson and E. Turkel, "Central Difference TVD and TVB Schemes for Time Dependent and Steady State Problems," AIAA Paper 92-0053, 30th Aerospace Sciences Meeting, Reno, Nevada, January 1992.

[6] D. A. Caughey, "Implicit Multigrid Euler Solutions with Symmetric Total-Variation-Diminishing Dissipation," Proceedings of the AIAA 11th Computational Fluid Dynamics Conference, Orlando, Florida, July 6-9, 1993, pp.676-684.

[7] A. Harten, B. Enquist, S. Osher, and S. Chakravarthy, "Uniformly High Order Accuracy Essentially Non-oscillatory Schemes III," J. Computational Physics, Vol. 71, pp.231-323, 1987.

[8] C. Shu and S. Osher, "Efficient Implementation of Essentially Non-Oscillatory Shock-Capturing Schemes," Journal of Computational Physics, Vol. 77, No. 2, pp. 439-471, 1988.

[9] A.M. Rogerson and E. Meiberg, "A Numerical Study of the convergence Properties of ENO Schemes," Journal of Scientific Computing, Vol. 5, No. 2, pp. 151-167, 1990.

[10] Jay Casper, Chi-Wang Shu, and H.L. Atkins, "A Comparison of Two Formulations for High-Order Accurate Essentially Non-Oscillatory Schemes," AIAA 93-3338, presented at the 11th Computational Fluid Dynamics Conference, Orlando, FL, July 6-9, 1993.

[11] C. Shu, "Numerical Experiments on the Accuracy of ENO and Modified ENO Schemes," Journal of Scientific Computing, Vol. 5, No. 2, pp. 127-150, 1990.

[12] H.L. Atkins, "High-Order ENO Methods for the Unsteady Compressible Navier-Stokes Equations," AIAA 91-1557, AIAA 10th Computational Fluid Dynamics Conference, June 24-26, 1991.

[13] P.L. Roe, "Approximate Riemann Solvers, Parameter Vectors, and Difference Schemes," Journal of Computational Physics, Vol. 43, pp.357-372, 1981.

[14] S. Osher and F. Solomon, "Upwind Difference Schemes for hyperbolic Systems of Conservation Laws," Mathematics of Computation, Vol. 38, pp.339-374, 1982.

[15] H. Atkins and Jay Casper, "Non-reflective Boundary Conditions for High Order Methods," AIAA 93-0152, presented at the AIAA 31st Aerospace Sciences Meeting, Reno, NV, Jan. 1993.

[16] Jay Casper and Kristine R. Meadows, "Using High-Order Accurate Essentially Non-Oscillatory Schemes for Aeroacoustic Applications," AIAA-95-0163, presented at AIAA 33rd Aerospace Sciences Meeting & Exhibit, Reno, NV, Jan. 9-12, 1995.

[17] Jay C. Hardin, and D. Stuart Pope, "A New Technique for Aerodynamic Noise Calculations," DGLR/AIAA 14th Aeroacoustics Conference, AIAA Paper 92-02-076,1992.

[18] Douglas Martin Nark, "A Computational Aeroacoustics Approach to Sound Generation by Baffled Pistons", Masters Thesis, The George Washington University, 1992.

[19] Willie Ross Watson, "A Time Domain Numerical Theory for Studying Steady-State Acoustic Disturbances in Flow", Doctoral Dissertation, The George Washington University, 1991.

[20] A. Jameson, "A Steady-State Solution of the Euler Equations for Transonic Flow," Transonic, Shock, and Multi-Dimensional Flows: Advances in Scientific Computing, R. Meyer, Ed., Academic Press, pp. 37-70, 1982.

[21] Dale A. Anderson, John C. Tannehill, and Richard H. Pletcher, Computational Fluid Mechanics and Heat Transfer, Hemisphere Publishing, New York, 1984.

[22] Charles Hirsch, Numerical Computation of Internal and External Flows, Volume 2, John Wiley and Sons, New York, 1990.

[23] P.E. Doak, "On the Interdependence Between Acoustic and Turbulent Fluctuating Motions in a Moving Fluid," Journal of Sound and Vibration, Vol. 19, No. 2, pp. 211-225, 1971.

[24] G.B. Whitham, Linear and Nonlinear Waves, John Wiley and Sons, New York, 1974.

[25] Jay C. Hardin, Introduction to Time Series Analysis, NASA Reference Publication 1145, March 1986.

Chapter 4

Interaction of Sound with a Shock Wave

4.1 Introduction

In this chapter the interaction of a sound wave with a shock is considered. This study is meaningful because it models the planar oscillation of a shock wave, and shock waves in real aerodynamic flows are inherently unsteady.

In the first three sections, shock capturing formulations of the MacCormack and ENO schemes are applied to the governing equations of fluid dynamics for time dependent, shocked flow through a nozzle. The emphasis of these computations is to predict numerically the amplification of sound by a shock and to compare the solutions provided by the different algorithms. Validation of numerical results is always important, but is particularly important for these calculations because, although high-order schemes ensure high-order accuracy in smooth regions of the solution, they necessarily reduce to first order at the shock. Hence, accuracy is

lost in the vicinity of the most important region of the solution: the sound source. Since a linear theory exists for this problem, numerical results are validated for the case of small amplitude acoustic waves incident on the shock. Much of the content in the first three sections was originally published by the author [1], but is included here for completeness, with permission from the publisher.

Section 4.4 includes an analysis of the disturbance energy associated with a sound wave passing through a shock. This analysis provides insight into the source of disturbance energy generated at the shock.

4.2 Analysis

4.2.1 Linear Theory

Within the context of linear theory, only entropy and acoustic waves may exist in a quasi-one dimensional flow [2]. In a fully linear flow, these waves are independent. However, when the flow field contains nonlinear features such as shock waves, the nonlinearity acts as a coupling mechanism between the linear waves. Thus, the presence of shock waves in a flow field makes it possible for a sound wave incident upon a shock to suddenly change its amplitude and generate an entropy wave.

The physical explanation for this phenomenon is as follows. Entropy is generated across the shock. For a steady flow, this change in entropy is independent of time. However, when a sound wave impinges upon the shock, the shock begins to oscillate, the change in entropy is no longer constant, and a periodic entropy wave is generated which convects downstream at the local flow velocity. In addition, the impinging sound wave is amplified.

Linearized analyses of the interaction of small disturbances with shock waves

have been made independently by Blokhintsev [3], Burgers [4], Moore [5] and Powell [6]. Landau and Lifschitz [7] report that the ratio of transmitted to incident sound waves determined by linear theory is:

$$\frac{\delta p_2}{\delta p_1} = \frac{(M_1+1)}{(M_2+1)} * \frac{2(\gamma-1)M_1M_2^2(M_1^2-1)-(M_1+1)[(\gamma-1)M_1^2+2]}{2(\gamma-1)M_2^2(M_1^2-1)-(M_2+1)[(\gamma-1)M_1^2+2]} \quad (4.1)$$

where M_1 is the Mach number upstream of the shock (henceforth called the pre-shock Mach number) , M_2 is the Mach number downstream of the shock, and γ is the ratio of specific heats of the fluid. Equation 4.1 as well as a similar expression for the ratio of static pressures, $\frac{p_2}{p_1}$ are plotted on Figure 4.1 for the ratio of specific heats, $\gamma = 1.4$. Note that Equation 4.1 predicts an amplification of the acoustic signal as it propagates through the shock wave for all pre-shock Mach numbers. This is not surprising, since the mean flow pressure also increases across a shock, but it is interesting that the ratio of the perturbation pressures, $\frac{\delta p_2}{\delta p_1}$, is not the same as that for static pressures, $\frac{p_2}{p_1}$.

4.2.2 Riemann Analysis

The results of the previous section are based on linear theory in which disturbance amplitudes are assumed to be small. To determine the range for which the linear result is valid, one may compute the ratio of disturbance pressures across the shock by considering the iterative solution to the Riemann problem. The Riemann analysis is performed by considering the space-time diagram illustrated in Figure 4.2. Initially a steady shock wave separates states 1 and 4. At some time Δt, a disturbance is introduced upstream of the shock which moves the shock and produces acoustic and entropy waves downstream. Knowing the initial states 1 and 4, and the incident perturbation amplitude, and utilizing the facts that acoustic waves

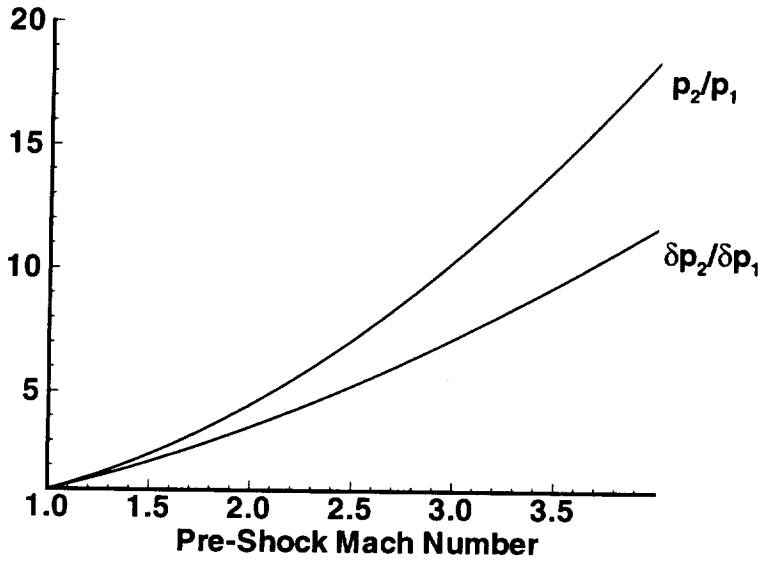

Figure 4.1: Ratios of Static and Perturbation Pressures as Functions of Pre-Shock Mach Number.

are isentropic and entropy waves introduce no pressure perturbation, the ratio of the perturbed states 2 and 1 may be found by numerical iteration. For an incident sound wave of pressure perturbation $\delta p_1 = \epsilon p_1 \sin \omega t$, the ratio $\frac{\delta p_2}{\delta p_1}$ is of interest and is compared with the linear theory result in Figure 4.3 for several perturbation amplitudes and shows excellent agreement for perturbation amplitudes less than $\epsilon = 10^{-1}$. (Results for $\epsilon \leq 10^{-2}$ are visually indistinguishable from the Blokhintsev line.) Even for perturbation amplitudes on the order of $\epsilon = 1.0$, there is only a 10 per cent difference between the solutions at $M = 3$.

Combining the expression for $\frac{\delta p_2}{\delta p_1}$ with the Rankine-Hugoniot shock jump relations, one may calculate similar expressions for the fluctuations in density and entropy downstream, as well as the shock velocity. These relations are plotted in Figures 4.4 and 4.5. Figure 4.4 shows the relationship between the ratios of pertur-

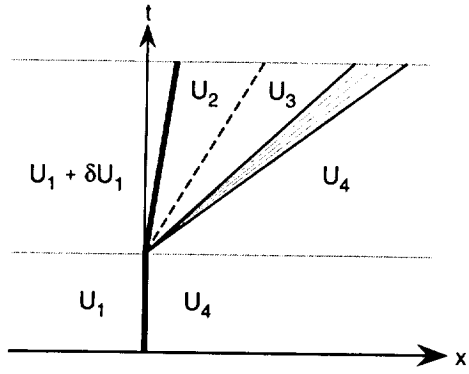

Figure 4.2: Diagram of the quasi-steady Riemann problem analysis for sound-shock interaction. Bold line represents shock. Dashed line represents entropy wave. Lines between states 3 and 4 represent acoustic wave.

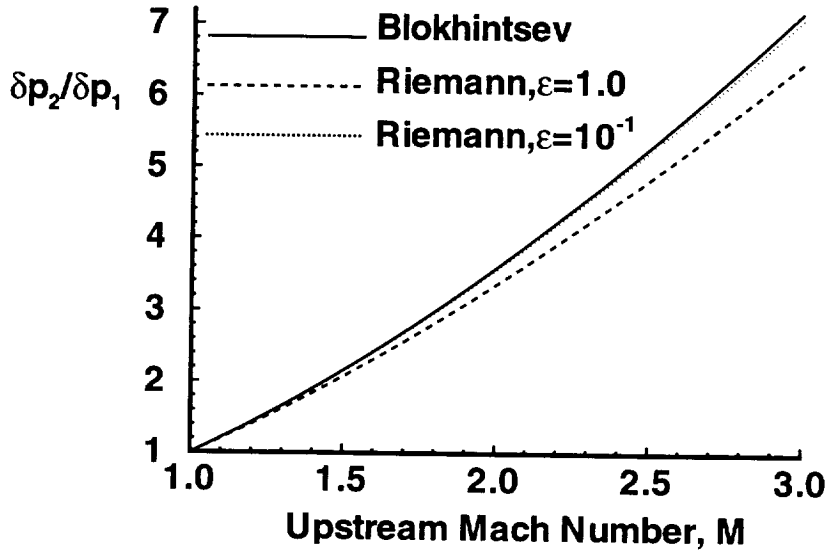

Figure 4.3: Pressure Perturbation as Function of Upstream Mach Number.

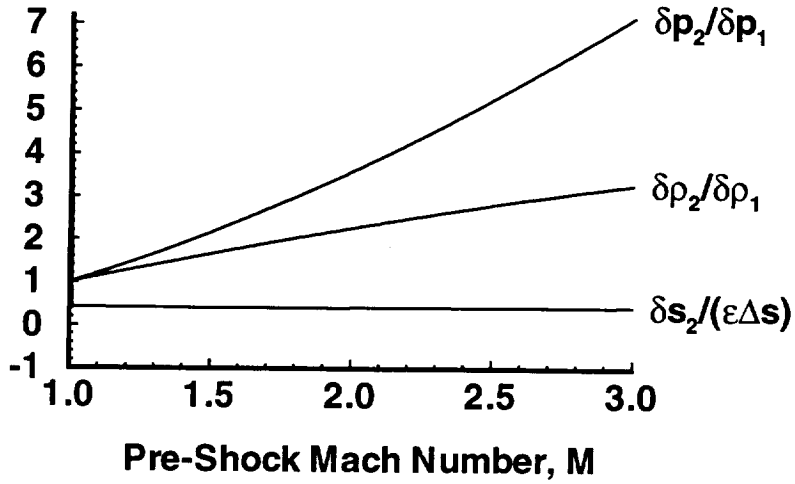

Figure 4.4: Perturbation Ratios as a Function of Upstream Mach Number.

bation pressure, entropy and density perturbations across the shock. These ratios were computed using a perturbation amplitude of $\epsilon = 10^{-3}$. This figure shows that the pressure fluctuation is most significant over a wide range of Mach numbers. The entropy fluctuations downstream of the shock are very small; the quantity $\frac{\delta s}{\Delta s}$ is on the order of ϵ, except near $M = 1$ where $\Delta s \rightarrow 0$. Figure 4.5 shows the difference between the upstream Mach number and the shock Mach number as a function of the upstream Mach number for several perturbation amplitudes. The linear theory results are presented in lines with no symbols, while the results obtained by using $\frac{\delta p_2}{\delta p_1}$ obtained by the Riemann analysis are presented with dots. As expected, the results obtained for small perturbations ($\epsilon \leq 10^{-1}$) are indistinguishable from the results of the Riemann analysis, while there is a significant difference in the results obtained for the large perturbation ($\epsilon = 1.0$). The shock motion increases with upstream Mach number and perturbation amplitude.

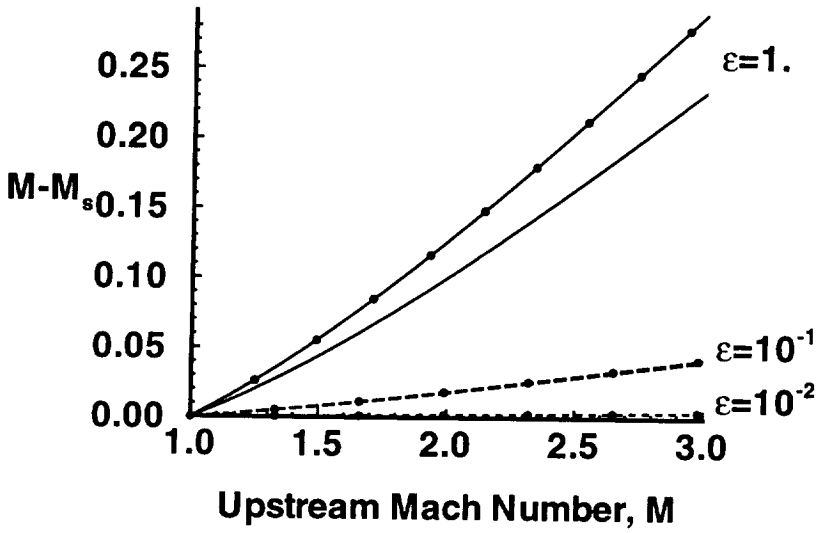

Figure 4.5: Shock Speed Number as a Function of Upstream Mach Number. Solid lines correspond to $\epsilon = 1.0$;Long dashed line corresponds to $\epsilon = 10^{-1}$; Dashed line corresponds to $\epsilon = 10^{-2}$. Dots on lines represent results obtained from Riemann analysis.

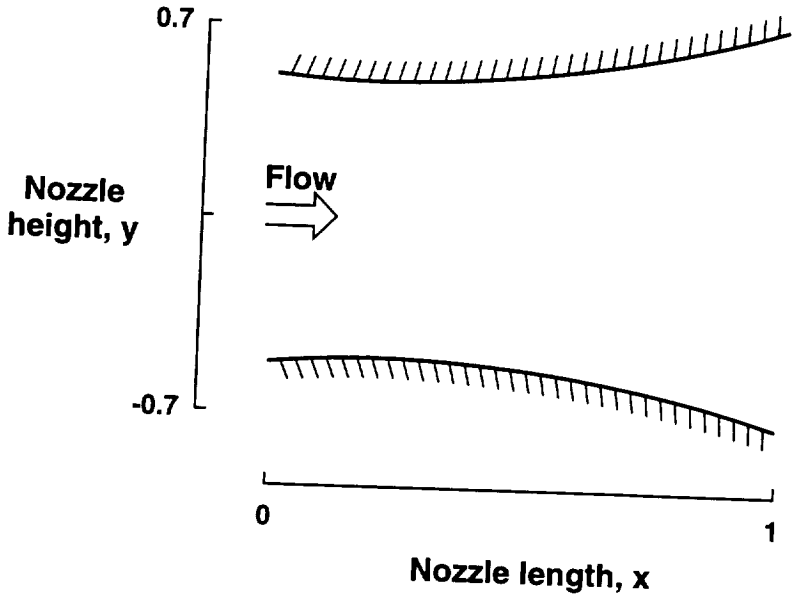

Figure 4.6: Nozzle Geometry for Mach Slope =1.

4.3 Model Problem

4.3.1 Governing Equations

The equations governing the unsteady quasi-one dimensional flow in a nozzle are:

$$\frac{\partial U}{\partial t} + \frac{\partial F}{\partial x} = Q \tag{4.2}$$

where U is the vector of conserved variables $[\rho, \ \rho u, \ \rho e]^T$, F is the flux vector, $[\rho uA, \ (\rho u^2 + p)A, \ (\rho e + p)uA]^T$, where A is the area of the nozzle, and Q is a source vector due to the area variation, $[0, \ p\frac{dA}{dx}, \ 0]^T$. Standard notation is used; ρ is density, u is velocity, e is total energy per unit mass, and p is pressure.

4.3.2 Nozzle Shape

Consider a nozzle which is converging-diverging, and designed for a linear Mach number distribution when flow is isentropic and fully expanded to produce super-

C-2

Table 4.1: Mach slopes and corresponding range of pre-shock Mach number.

Mach Slope α	Pre-Shock Mach No.
1	1.4 to 1.8
2	2.0 to 2.6

sonic velocity in the diverging section. The Mach number at the nozzle inlet is $M = .8$ and varies as a function of distance along the nozzle length:

$$M(x) = \alpha x + .8, \qquad 0 \leq x \leq 1 \tag{4.3}$$

where x is the distance along the nozzle, normalized by the nozzle length. Two Mach slopes are used to facilitate consideration of a range of practically significant pre-shock Mach numbers and keep the shock close to the center of the nozzle diffuser. The values of Mach slope, α, used in the calculations presented here and the corresponding pre-shock Mach numbers are presented in Table 4.1.

A sketch of a nozzle with a Mach slope of 1 is shown in Figure 4.6.

4.3.3 Governing Equations and Boundary Conditions

The unsteady, compressible, inviscid flow in a nozzle of varying cross sectional area is governed by the quasi-one dimensional Euler equations 4.2. These equations are solved in conservation form so that shocks are automatically captured. Total pressure and entropy are prescribed upstream of the shock at the nozzle inlet, and static pressure is prescribed downstream of the shock at the nozzle exit plane. Flow quantities are normalized by the upstream stagnation conditions and the nozzle length, L. Finite wave conditions developed by Atkins and Casper [8] are employed at the boundaries.

The first step in numerically modeling the interaction of a sound wave with a shock is to determine an accurate steady flow solution throughout the nozzle. To obtain sufficiently accurate unsteady results, the steady state residual is converged to several orders of magnitude smaller than the smallest perturbation amplitude to be investigated. Steady flows with residuals only one or two magnitudes smaller than the perturbation amplitude may introduce spurious entropy at the inflow boundary in the unsteady calculation.

To induce unsteady flow through the nozzle, the inflow boundary condition is perturbed sinusoidally and isentropically. The pressure perturbation is prescribed as :

$$\delta p = \epsilon \ p \ \sin \omega t \tag{4.4}$$

where ϵ and ω are the normalized amplitude and frequency of the perturbation, and p and t are the normalized pressure at the inflow boundary and time. The pressure perturbation introduces an acoustic wave at the nozzle inlet which propagates downstream at a velocity equal to the sum of the local velocity and sound speed. A range of perturbation amplitudes is selected so that linear as well as nonlinear waves can be investigated. The time dependent features of the flow are computed, and the effect of the shock on the sound wave is observed.

4.3.4 Algorithms

In order to admit discontinuous solutions, shock capturing formulations of the MacCormack and ENO algorithms described in Chapter 2 are employed for the computations. Therefore, shock fitting methods which explicitly invoke the Rankine-Hugoniot jump relations across a shock are not required.

4.4 Results

4.4.1 Unsteady Calculations

The results presented in this section are for the case of perturbation amplitude, $\epsilon = .01$, and a frequency, $\omega = 60$, which corresponds to an approximate wave number of 5.25. The calculations are performed on a grid of 128 cells, which corresponds to approximately twenty-four points per wavelength. The nozzle back pressure is prescribed so that a shock appears at $x = .6$ in the steady solution. For a nozzle with a Mach slope $\alpha = 1$, this corresponds to a pre-shock Mach number of 1.4.

Figure 4.7 shows the perturbation pressure, density, and velocity in the nozzle at a normalized time of π, and compares the results provided by the MacCormack and 2nd, 3rd, and 4th order ENO schemes. Perturbation quantities are determined by subtracting the mean flow quantities from their time dependent counterparts:

$$\begin{aligned} \delta p(x,t) &= p(x,t) - p(x,0) \\ \delta \rho(x,t) &= \rho(x,t) - \rho(x,0) \\ \delta u(x,t) &= u(x,t) - u(x,0) \end{aligned} \tag{4.5}$$

The following are observations of the numerical results: The MacCormack and 3rd and 4th order ENO schemes do an excellent job of predicting the perturbation pressure upstream of the shock, where the flow is smooth. The second order ENO scheme, which behaves similar to a TVD scheme because it has only second order interpolation, has a slight leading phase error. At the shock, the ENO schemes do a better job of capturing the shock in fewer cells. The flow solutions differ more significantly downstream of the shock. The phase shift error is amplified and the

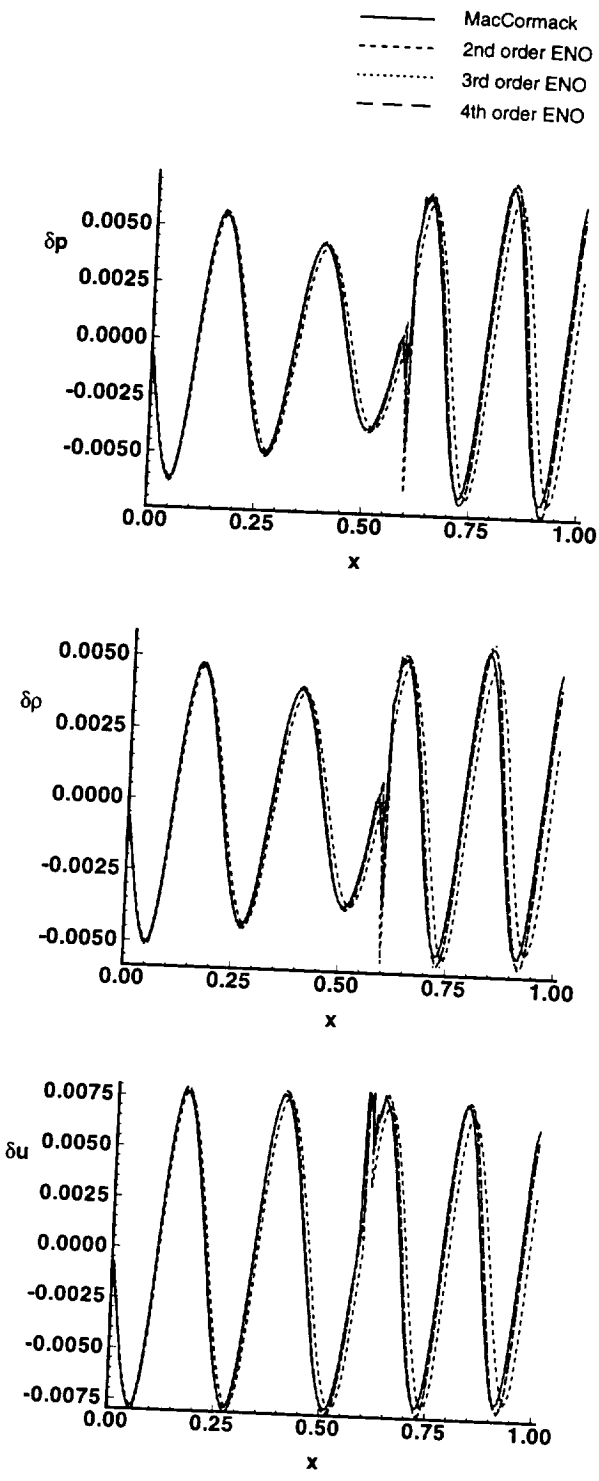

Figure 4.7: Pressure, Density and Velocity Perturbations Along Nozzle Length.

wave amplitude is dissipated in the 2nd order ENO results. The MacCormack solution is slightly damped relative to the 3rd and 4th order ENO solutions, and has spurious oscillations on portions of the perturbations close to the shock. The difference in the solution between the third and fourth order ENO schemes is not graphically perceptible on this scale. These results show that all the algorithms applied to this problem do a good job of computing the perturbation quantities in the nozzle. The 3rd and 4th order ENO schemes provide the best solutions because they have no oscillations at the shock and less damping downstream. The cost of running high-order ENO is higher than second order ENO or MacCormack, however, and the economics of high-order schemes is discussed in Section 2.4.

4.4.2 Effect of Mach Number

Sound amplification by a shock wave is highly dependent upon the pre-shock Mach number. To illustrate this numerically, Figures 4.8 and 4.9 show a sequence of pressure perturbations moving through the nozzle for pre-shock Mach numbers of 1.58 and 2.36. A small amplitude perturbation of $\epsilon = 10^{-5}$ is introduced at the inflow boundary. The perturbation is seen to maintain its sinusoidal shape throughout the nozzle. The amplitude decreases as the flow expands in the nozzle upstream of the shock. At the shock, it is amplified as the flow is compressed, and continues to increase gradually as the flow is compressed further. It is clear that the amplification of the sound wave is much more significant at the higher Mach number.

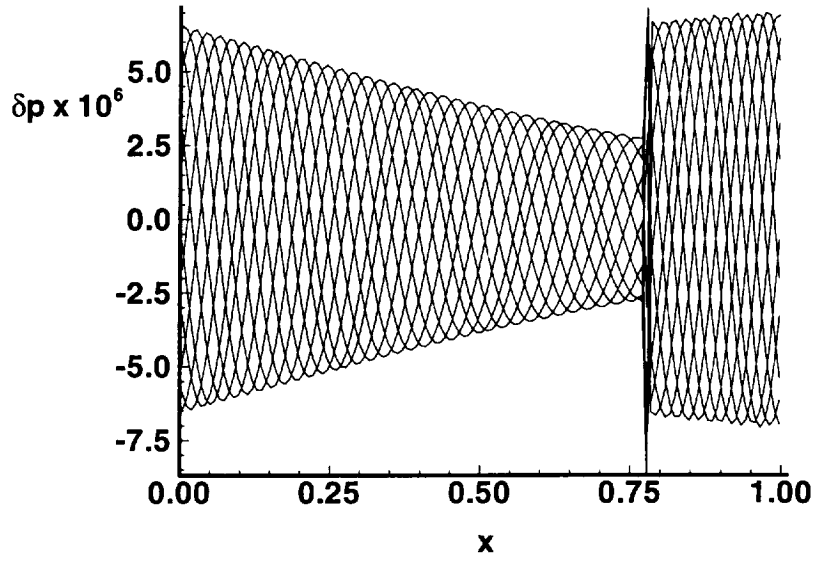

Figure 4.8: Several Snapshots in Time of Pressure Perturbation Along Nozzle. $\epsilon = 10^{-5}$, $M_1 = 1.58$.

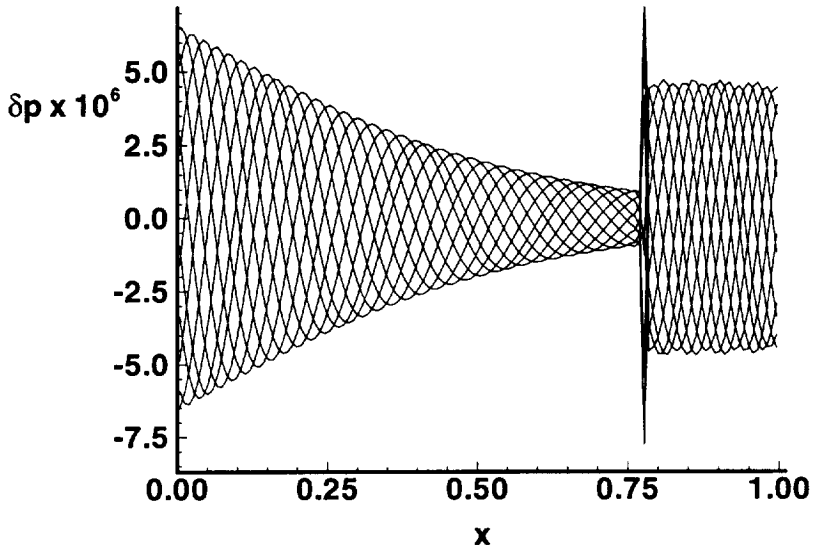

Figure 4.9: Several Snapshots in Time of Pressure Perturbation Along Nozzle. $\epsilon = 10^{-5}$, $M_1 = 2.36$.

Table 4.2: Pre-shock Mach number and minimum cells per wavelength for the calculations presented in this paper.

Pre-Shock Mach No.	Minimum Cells/Wavelength
1.4	26.92
1.58	26.18
1.7	25.75
2.0	23.52
2.36	22.50
2.6	22.13

4.4.3 Comparison of Numerical Results with Linear Theory

To quantify the effect of Mach number on the perturbation amplification and validate the computations, the numerically determined pressure perturbation amplitude ratio is compared in Figure 5 with the linear theory over a range of Mach numbers, and for two perturbation amplitudes: $\epsilon = 10^{-5}$ and $\epsilon = 10^{-2}$. The first amplitude is small enough to be well within the validity of the linear theory. The second amplitude approaches the limit of linear theory validity, particularly for the lower Mach numbers where the shock is weak and may undergo large excursions. The normalized acoustic perturbation wavenumber at the inflow boundary is set to 4. Results for Mach numbers between 1.4 and 2.6 are presented here. The computations have from 22 to 27 cells per wavelength, depending on the particular cases being calculated. Table 4.2 below lists the cells per wavelength for the cases presented in this paper.

Figure 4.10 compares the numerical results with linear theory. The 3rd order ENO scheme and linear theory match extremely well for the very small amplitude

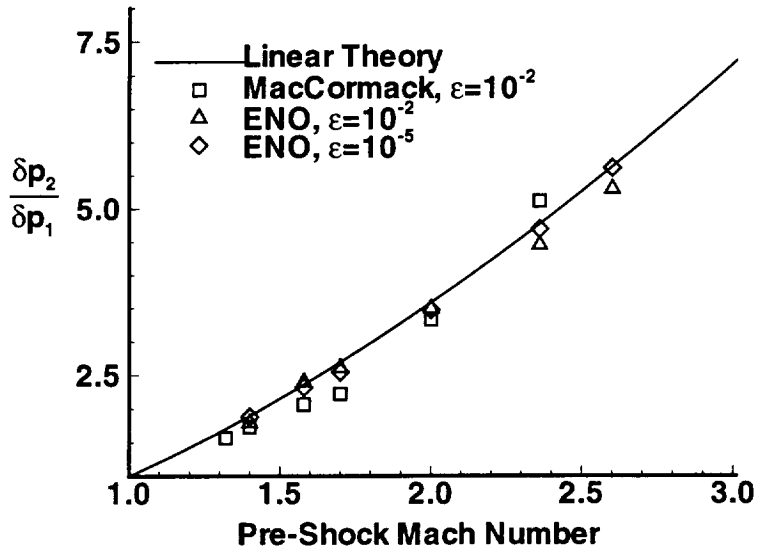

Figure 4.10: Pressure Perturbation Ratio as a Function of Pre-Shock Mach Number.

perturbation, $\epsilon = 10^{-5}$. The differences between numerical solutions and linear theory become more pronounced at the higher perturbation amplitude, $\epsilon = 10^{-2}$. Some discrepancy between the linear theory and numerical results is not surprising since nonlinearities may become important at this perturbation amplitude. Because the shock in the MacCormack solution is spread over several cells, determination of the ratio $\frac{\delta p_2}{\delta p_1}$ is more difficult, particularly when the shock is located close to the end of the nozzle. This is why no MacCormack result is shown for $M = 2.6$.

4.4.4 Energy Analysis

The previous sections have shown that according to linear theory and numerical computation, sound pressure is amplified as a sound wave passes through a shock.

This section will address the issue of whether or not acoustic energy is generated in the interaction process.

To answer this question, consider Myers' energy corollary [9]. Myers' energy corollary is an exact equation governing the transport of energy associated with an arbitrary flow field. This corollary allows for a description of the acoustic energy in general situations where the linear description of energy is inadequate. Clearly, with the highly nonlinear flow field associated with sound-shock interaction, such an approach is warranted here.

For a one-dimensional flow in which viscous effects are negligible, Myers' corollary reduces to:

$$\frac{\partial E}{\partial t} + \frac{\partial W}{\partial x} = -D \tag{4.6}$$

where the disturbance energy density is defined

$$\frac{E}{A} = \frac{1}{2}\rho(u^2 - u_0^2) + \rho_0 u_0 \cdot (u_0 - u) - \rho T_0(s - s_0) - (p - p_0) + \rho(h - h_0) \tag{4.7}$$

where A is the cross sectional area of the duct, T is the absolute temperature, h is the enthalpy, s is entropy, ρ is density, p is pressure, u is velocity. The subscript $_0$ represents the undisturbed state. The disturbance energy flux is

$$\frac{W}{A} = (\rho u - \rho_0 u_0)[h - h_0 - T_0(s - s_0)] + \rho_0 u_0 (T - T_0)(s - s_0) \tag{4.8}$$

and the disturbance energy source is

$$\frac{D}{A} = -(\rho u - \rho_0 u_0)(s - s_0) \cdot \nabla T_0 - (s - s_0)\rho_0 u_0 \cdot \nabla(T - T_0) \tag{4.9}$$

For the one-dimensional sound-shock interaction, only acoustic and entropy modes are present (vorticity requires three dimensions). Thus, the energy density

can be divided into two types of energy, acoustic and entropy, as:

$$E_a = \frac{1}{2}\rho(u^2 - u_0^2) + \rho_0 u_0(u_0 - u) - (p - p_0) + \rho \left.\frac{\partial h}{\partial p}\right|_s (p - p_0) \tag{4.10}$$

and

$$E_s = \rho \left[\left.\frac{\partial h}{\partial s}\right|_p (s - s_0) - T_0(s - s_0) \right] \tag{4.11}$$

where

$$\left.\frac{\partial h}{\partial s}\right|_p = \frac{1}{\gamma - 1} p^{\frac{\gamma-1}{\gamma}} s^{\frac{1-\gamma}{\gamma}} \tag{4.12}$$

and

$$\left.\frac{\partial h}{\partial p}\right|_s = p^{\frac{-1}{\gamma}} s^{\frac{1}{\gamma}} \tag{4.13}$$

for an ideal gas.

It is instructive to examine the energy components and energy source terms in space time to see how these quantities change during the sound-shock interaction process. These quantities presented in Eqns. 4.10, 4.11 and 4.9 are shown in Figures 4.11 -4.13 for the case where the Mach number upstream of the shock, $M_1 = 3$, the acoustic disturbance amplitude, $\epsilon = .1$, and 512 cells are distributed along the duct length. For these calculations, the shock is initially at $x = .4$. The sound disturbance enters the duct at $t = 0$ at the duct inlet and propagates downstream. At a time of $t \approx 0.13$ the sound wave hits the shock. After the interaction, Figure 4.11 shows that acoustic energy is present downstream. The amplitude of the sound energy downstream of the shock is higher than the energy upstream, indicating that acoustic energy is generated by the sound-shock interaction process. It is comforting to note that the slope of the path of the sound wave in space-time increases after interaction with the shock. The inverse of the slopes before and after the shock corresponds to the quantities $u_1 + c_1$ and $u_2 + c_2$, respectively,

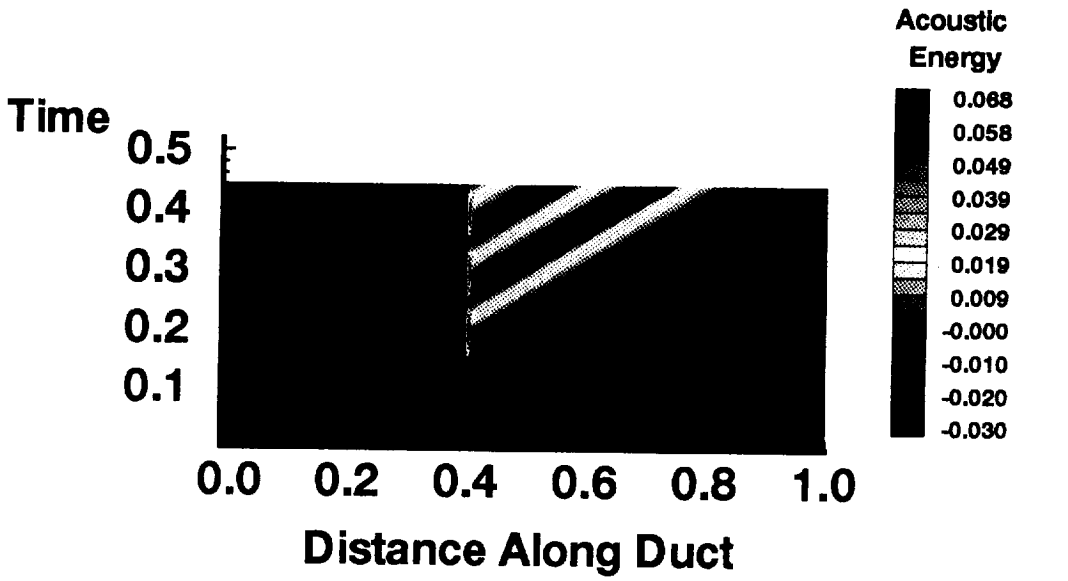

Figure 4.11: Disturbance acoustic energy as a function of space time. Pre-shock Mach number is 3, disturbance acoustic amplitude = 0.1, 512 cells distributed along duct length.

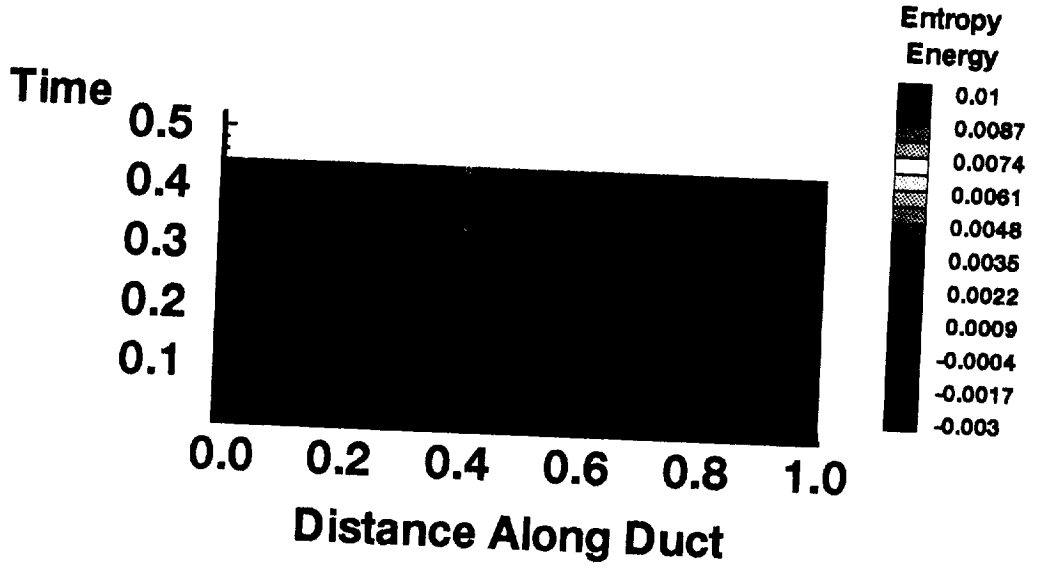

Figure 4.12: Disturbance entropy energy as a function of space time. Pre-shock Mach number is 3, disturbance acoustic amplitude = 0.1, 512 cells distributed along duct length.

where the subscripts 1 and 2 refer to the states upstream and downstream of the shock.

Figure 4.12 shows the component of entropy energy in space-time. Clearly, because the sound wave is by definition isentropic, there is no disturbance entropy upstream of the shock. After the sound wave hits the shock at $t \approx 0.13$, however, entropy energy appears downstream. Thus, entropy energy is generated during sound-shock interaction. The inverse slope of the path of the disturbance entropy corresponds to the downstream convection velocity, as expected. Figure 4.13 is interesting because it portrays the variation in the source term of Eqn. 4.9, and provides insight into the nature of the generation of disturbance acoustic and en-

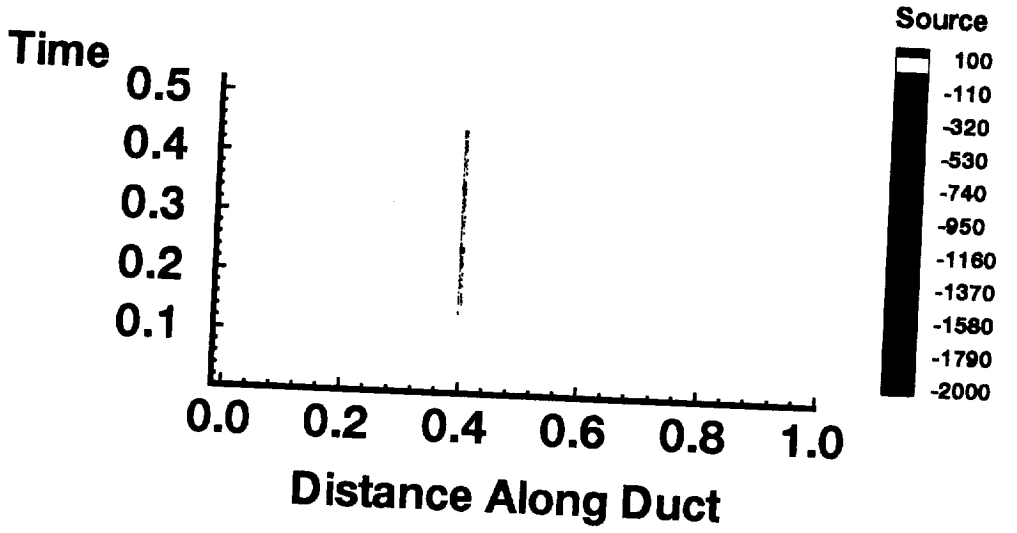

Figure 4.13: Disturbance energy source as a function of space time. Pre-shock Mach number is 3, disturbance acoustic amplitude = 0.1, 512 cells distributed along duct length.

tropy energy downstream of the shock. The source term is zero except along the shock wave for $t > 0.13$. Thus, the shock wave is the source of the disturbance energies downstream. Inspection of Eqn. 4.9 indicates that the source of disturbance energy is the transfer of energy from the mean flow. This transfer can occur in the presence of a temperature gradient with fluctuations in entropy and momentum, and with fluctuation of entropy and temperature. Note that the source term is zero when the fluctuation in the entropy is zero. This implies that the disturbance energy source is related to the shock motion.

4.5 Concluding Remarks

This chapter describes a numerical investigation of sound amplification by a shock wave. The MacCormack and 2nd, 3rd, and 4th order ENO schemes are employed to compute the time dependent shocked flow field in a converging-diverging nozzle. The flow is disturbed by introducing a sound wave at the inflow boundary. All of the schemes are shown to do a good job in predicting the perturbation amplitude and phase speed in the nozzle, especially in the supersonic, smooth portion of the flow. The high-order ENO schemes provide the best overall results because the flow around the shock does not contain spurious oscillations and the flow downstream of the shock shows little dissipation.

The numerical results are compared to the linear theory. Linear theory validates the numerical solution for small perturbation amplitudes. Numerical results for the larger perturbation amplitude also compare well to the linear theory, indicating that the linear theory has a wide range of applicability in predicting sound amplification by a shock.

Analysis of the equation governing the perturbation energy shows that disturbance energy is generated at the shock. The source term for this energy goes to zero as the entropy fluctuation goes to zero. This indicates the importance of shock motion on the generation of disturbance energy.

Bibliography

[1] Meadows, Kristine R., Casper, Jay, and Caughey, David A., "A Numerical Investigation of Sound Amplification by a Shock Wave," FED-Vol. 147, Computational Aero-and Hydro-Acoustics, R. Mankbadi, A. Lyrintzis, and O. Baysal, eds., ASME Book No. H00787, pp. 47-52, 1993.

[2] Chu, Boa-Teh, and Kovasznay, Leslie S.G., "Non-linear Interactions in a Viscous Heat Conducting Compressible Gas," *Journal of Fluid Mechanics*, Oct.-Mar., pp. 494-514, 1958.

[3] Blokhintsev, D., "Sound Receiver in Motion", *Comptes Rendus (Doklady) De L'Academe Des Sciences De L'URSS*, Volume XLVII, No. 1, 1945.

[4] Burgers, J.M., "On the Transmission of Sound Waves Through a Shock Wave", *Koninklijke Nederlandische Akademie van Wetenschappen,* Volume XLIX, No. 3, 1946.

[5] Moore, Franklin K., "Passage of Flow Disturbances Through a Duct Containing Screens, Shocks, or Contractions," *Proceedings of 3rd Midwestern Conference on Fluid Mechanics, University of Minnesota*, pp.193-217, 1953.

[6] Powell, Alan, "One-dimensional Treatment of Weak Disturbances of a Shock-wave", *Aeronautical Research Council Current Papers*, C.P. No. 441, 1959.

[7] L.D. Landau and E.M. Lifschitz, *Fluid Mechanics*, Pergamon Press, New York, 1959.

[8] Atkins, H. and Casper, Jay, "Non-reflective Boundary Conditions for High Order Methods," AIAA paper 93-0152 to be presented at the AIAA 31st Aerospace Sciences Meeting, Reno, NV, Jan. 1993.

[9] Myers, Michael K., "Transport of energy by disturbances in arbitrary steady flows," Journal of Fluid Mechanics, Vol. 226, 1991, pp.383-400.

Chapter 5

Interaction of a Vortex Ring with a Shock Wave

5.1 Introduction

In this chapter the interaction of a vortex ring with a normal shock wave is considered. The study of this interaction is meaningful because it models a fundamental mechanism of sound generation in supersonic jets: the interaction of turbulence with shock waves.

Early research on shock vortex interaction focused primarily on experimental studies ([1], [2], [3]) and the development of predictive linear theories ([4], [5], [6]) that were compared with experimental results. Ribner suggested that the study of the interaction of a vorticity wave with a shock would provide useful information regarding the sound generated by turbulence in supersonic jet flows [4]. Ribner studied the problem analytically and developed a linear theory which described sound generated by vortex-shock interaction ([4], [6]). At about the same time,

Moore studied the interactions of a variety of plane wave disturbances with shocks in an unsteady reference frame [5].

Pao and Salas were the first to study the interaction of a shock wave and a vortex numerically [7]. This study investigated the interaction of a columnar vortex with a normal shock wave by solving the Euler equations using MacCormack's scheme with a shock-fitting numerical technique. Salas, Zang, and Hussaini [8], Hussaini, et.al. [9], and Kopriva et. al [10] applied spectral methods with shock fitting methods to the same problem. The use of spectral methods provided increased accuracy of the solution, but were limited to weak shock-vortex interaction cases. Meadows, Kumar and Hussaini [11] studied the interaction of a columnar vortex with a shock wave using a shock capturing scheme. Shock-capturing proved to be beneficial because strong shock-vortex interaction cases which result in the formation of secondary shocks, could be studied readily. The authors noted that in order to provide a quantitatively accurate representation of the acoustic wave, improved downstream boundary conditions and higher-order numerical schemes were required. Casper [12] then investigated the shock-vortex interaction problem with a high-order ENO scheme and found that higher accuracy greatly improved the resolution of the acoustic wave downstream of the shock.

The work cited above has been for columnar vortex-shock interactions. This study is believed to be the first for the interaction of a vortex ring with a shock wave. The interaction of a vortex ring with a shock more closely models the interaction of turbulence within the shear layer with shock waves present in the plumes of imperfectly expanded axisymmetric supersonic jets.

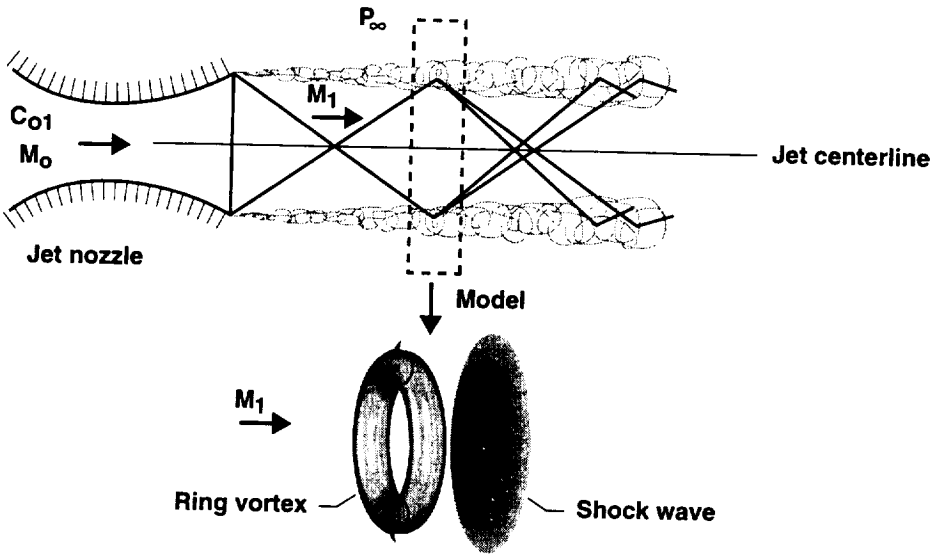

Figure 5.1: Vortex Ring - Shock Interaction.

5.2 Model

5.2.1 Overview

The calculations presented in this section are designed to model the interaction of a vortical structure within the supersonic portion of the shear layer with a shock wave. The core size is small relative to the size of the ring in these calculations, primarily because of numerical considerations. Because the shear layer in a jet spreads with increasing distance from the nozzle exit plane, a vortex ring with a small core models the interaction of disturbances in the shock cell closest to the nozzle lip. When results are presented in dimensional units, the variables are dimensionalized with ambient stagnation sound speed and atmospheric pressure; thus, the calculations performed most closely model disturbances interacting with the first shock cell of an overexpanded nozzle, illustrated in Figure 5.1.

The strength of the vortex is chosen to correspond to the observed strengths of

turbulent fluctuations in the jet shear layer. Experimental observations indicate that an appropriate level of velocity disturbance is on the order of three percent of the mean flow velocity [22]. The vortex strength chosen for the majority of the calculations presented here ($M_1 = 1.5$) has a velocity perturbation (defined as the ratio of the vortex core velocity to the upstream mean flow velocity) of 6.8%.

Although imperfectly expanded jet flows typically contain systems of oblique shocks, this model uses the interaction of a ring vortex with a normal shock wave. This is a reasonable approximation because the oblique shocks tend to curve upstream with increasing distance from the jet centerline and are approximately normal upon termination in the shear layer [22].

The sense of the vortex rotation is taken to be counterclockwise for the majority of the calculations because the velocity decreases with increasing distance from the jet axis, resulting in vorticity of a positive sense. Some results are shown for the case of a clockwise rotating vortex in Section 5.5.

5.2.2 Geometry

The geometric model of the interaction of a ring vortex with a shock wave used in the computations is illustrated in Figure 5.2. A vortex ring is introduced upstream of the shock wave. The vortex ring is characterized by its strength, Γ, its core radius, r_c, and the distance from the axis of symmetry to the vortex filament, r_0. The shock is characterized by the Mach number of the flow upstream of the shock, M_1.

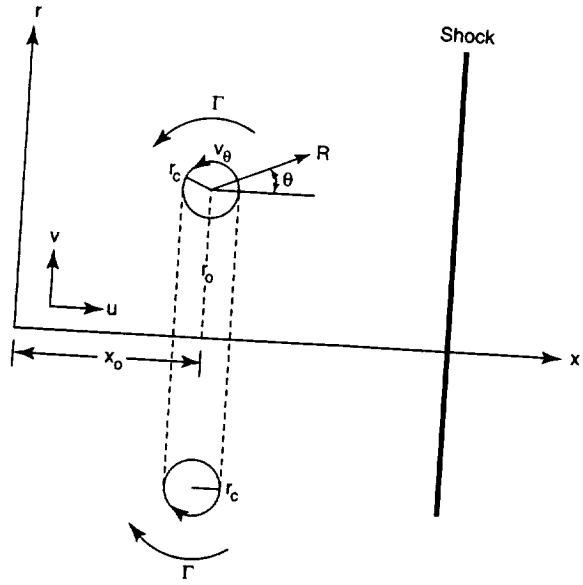

Figure 5.2: Vortex Ring - Shock Interaction.

5.2.3 Governing Equations

The equations which govern the interaction of a vortex ring with a shock wave, neglecting viscous effects, are the Euler equations of gas dynamics in axisymmetric coordinates:

$$\frac{\partial rQ}{\partial t} + \frac{\partial rF}{\partial x} + \frac{\partial rG}{\partial r} = H \tag{5.1}$$

where

$$Q = \{\rho, \rho u, \rho v, \rho e\}^T \tag{5.2}$$

$$F = \{\rho u, \rho u^2 + p, \rho uv, (\rho e + p)u\}^T \tag{5.3}$$

$$G = \{\rho v, \rho vu, \rho v^2 + p, (\rho e + p)v\}^T \tag{5.4}$$

$$H = \{0, 0, p, 0\}^T \tag{5.5}$$

and standard notation is used for the flow variables. Thus, ρ is density, u and v are the velocity components in the axial and radial directions, e is total energy per unit mass, p is pressure, x is the axial position, and r is the radial distance from the axis of symmetry.

5.2.4 Boundary Conditions

Conditions are prescribed at the inflow and outflow computational boundaries to establish a shock with the specified strength at $x = 7$. The boundary condition along the axis of symmetry is prescribed by requiring that the fluxes across the axis are zero. The method of prescribing the boundary conditions is described in [13].

5.2.5 Solution Procedure

The calculation is performed in two steps. First, a steady, shocked flow is established with the flow parallel to the axis of symmetry. Next, a vortex ring is introduced to the flow field 7 core radii upstream of the shock at $T = 0$. All flow variables are normalized with respect to the static pressure and density upstream of the shock, and the size of the vortex core radius. The vortex ring then convects downstream, passing through the shock wave. After this interaction, significant changes occur downstream of the shock wave. Sound, vorticity, and entropy are generated as the vortex interacts with the shock wave. The primary focus of this work is on the acoustic waves generated by the interaction.

5.2.6 Vortex Model

A model of the ring vortex is required to introduce appropriate perturbations in velocity and pressure to the flowfield as an *initial condition.* The vortex is introduced at the initial time $t = 0$, and at subsequent times the Euler equations determine the entire flow field - including the vortex. At all subsequent time steps the Euler equations are satisfied to a level of error corresponding to the truncation error of the ENO algorithm, which is third order accurate in space and time.

The initial condition prescribed for the vortex is the classical toroidal vortex of Lamb [14], augmented with a solid body core. The derivation of the velocity and pressure equations is provided in Appendix B.

Limits of the Vortex Ring Model

The cross section of the vortex ring core is approximately circular when the vortex filament is 170 core radii away from the axis of symmetry [16]. When the vortex core radius increases relative to the ring radius, the degree of circularity decreases, until the vortex becomes Hill's vortex [16], and the streamlines become oblong and flatten close to the axis of symmetry. To closely approximate the vortex ring with a circular core, the vortex filament is located 125 core radii away from the axis of symmetry unless otherwise noted. The small size of the vortex core radius relative to the ring radius reasonably approximates the size of a turbulent structure within the supersonic portion of the shear layer near the first shock cell.

5.2.7 Vortex Parameter Modeling

The parameters of the vortex ring which model the physical jet turbulence/shock interaction will be described here. The first parameter of interest is the vortex

strength. The circulation is typically considered to be a measure of the vortex strength. For the vortex ring, the circulation is related to the geometrical parameters and induced velocity, V, according to [16]

$$\Gamma = \frac{4V\pi r_0}{\ln \frac{8r_0}{r_c} - \frac{1}{4}}. \tag{5.6}$$

The next parameter of interest is the ratio of the core radius to the ring radius, $\frac{r_c}{r_0}$. The core radius models the size of the disturbance in the supersonic portion of the mixing layer interacting with the shock wave, while the ring radius models the radial distance between the jet axis of symmetry and the inner boundary of the turbulent mixing layer. Obviously, this ratio is a function of distance downstream from the jet exit plane.

5.2.8 Vortex Preservation Study

An important feature of this calculation is the accurate representation of the source of the sound generation: the interaction of a vortex with the shock. To ensure that the vortex is adequately resolved in the calculation, the time history of the minimum pressure within the vortex is tracked. A series of computations is performed where the vortex ring convects over grids of various resolutions. It was found that while convecting on a uniform mesh with 10 cells per core diameter, the minimum pressure varies by a maximum of 0.035% over the time it takes the vortex to travel 7 core radii, which is the initial distance of the vortex from the shock. This level of numerical error is considered to be acceptable, and so this grid resolution was held fixed for all the computations.

5.2.9 Computational Grid

As mentioned in the previous section, it was found that a grid having 10 cells per vortex core diameter was sufficient to adequately resolve the vortex in the computation. This grid resolution is used in the fine uniform grid in the region $-6 \leq x \leq 85$ and $72 \leq r \leq 178$, where $\Delta x = \Delta r = 0.2$. However, it is computationally prohibitive to use a uniform mesh with such fine resolution throughout the entire computational domain. The computational domain is required to be large enough such that at least one wavelength of the acoustic disturbance is contained in the calculation. This allows accurate measurements to be made in the acoustic far field so that computations to determine the acoustic energy level can be made. In addition, the computational domain must also be large enough that once the acoustic wave has passed a far field observer point, the wave has time to go through one period of its oscillation without being contaminated by errors introduced by the boundaries. Thus, in the calculations shown here, the computational grid is uniform over the range of the acoustic source interaction and sound wave propagation through at least one acoustic wavelength. The grid is then stretched to the boundaries using a hyberbolic sine function. The grid contains 481 cells in the axial direction and 556 cells in the radial direction. Every 15th cell of the grid is shown in Figure 5.3.

It is important to note that this grid resolves the generated acoustic waves. Preliminary test calculations performed over Mach number range $1.1 \leq M \leq 1.7$ cover an acoustic peak-to-valley wavelength range of $2.5 \leq \lambda \leq 3.0$. Thus, the minimum resolution of the acoustic wave is 12.5 points per peak-to-valley wavelength. The actual number of points per wavelength is at least twice this

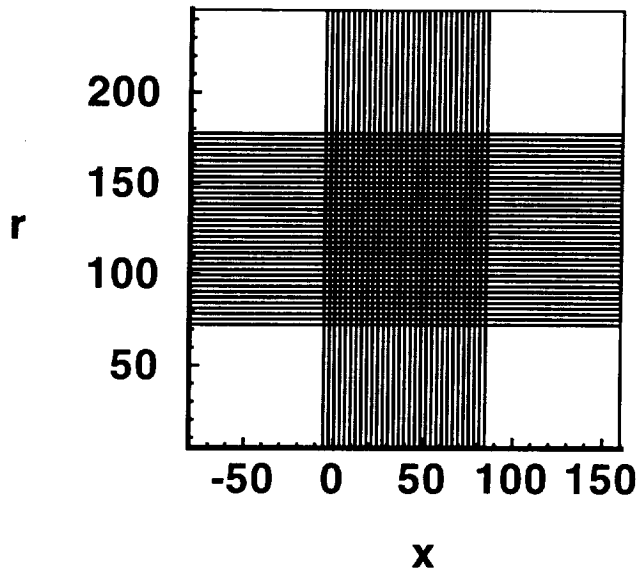

Figure 5.3: Standard grid used in calculations. Only every 15th cell is shown.

number. Thus, the acoustic wave is well resolved.

It is also important to note that there is another length scale of possible interest in this problem, which is not well resolved on this grid. During the interaction of the vortex with the shock, the shock wave begins to move. For typically small vortex strengths, the shock displacement is small. In fact, for many of the calculations performed during the course of this research, the shock moves through the distance of only one cell. Because further grid refinement proved to be prohibitively expensive and one-dimensional calculations of sound-shock interaction provided results which matched linear theory well without resolving the shock motion, the grid was not refined further.

5.3 Typical Interaction-Counterclockwise Vortex

5.3.1 Overview

A typical interaction of a counter-clockwise (CCW) rotating vortex with a shock wave is is described in this section. In the calculations for this case, the Mach number upstream of the shock is $M = 1.5$, and the vortex strength is $\Gamma = .75$. In the contour plots shown in this chapter, contours are shown for a part of the computational domain near the interaction point of the vortex core and the shock wave. Because of the axisymmetry, only a single cross-section of the solution will be shown in the results which follow. All the results presented are within the uniform grid region of the computational grid so that effects of grid stretching are not present in the results. The contours are computed on a grid which is five times as coarse as the computational grid. Note that the contour range is kept constant for each plot so that relative values of the perturbation quantities at different time levels can be compared. In these calculations, a unit of time is defined as $T = r_c/u_1$ where u_1 is the upstream flow speed; thus T represents the time it takes the vortex core to move 1 radius in the flow upstream of the shock.

Contour plots of the flow variables are shown for three selected times: $T = 0$, $T = 8$, and $T = 50$. At time $T = 0$, the vortex is upstream of the shock. At $T = 8$ the most upstream edge of the vortex core is approximately aligned with the shock; and at $T = 50$, the vortex is approximately 30 core radii downstream of the shock.

5.3.2 Pressure

Figure 5.4 shows the change in pressure from the mean state. The only perturbation in pressure at $T = 0$ is the decrease in pressure at the vortex core. As the vortex begins to interact with the shock, additional pressure perturbations are generated downstream of the shock. At $T = 8$ high amplitude pressure disturbances are seen just downstream of the shock. As time passes, these pressure disturbances travel downstream more rapidly than the vortex. Figure 5.5 shows a plot of the position of the peak pressure (in radii from the vortex filament) as a function of time (in periods). The plot shows a linearly increasing change in the position of the pressure disturbance as a function of time, which means that the pressure disturbance is traveling at a constant speed relative to the vortex. The slope of this curve is found to be $\frac{\Delta R}{\Delta T} = 0.77$ core radii per period, the sound speed downstream of the shock. (The velocity 0.77 core radii per period is equivalent to a velocity normalized by the sound speed upstream of the shock of 1.15. The ratio of the sound speeds across the shock is 1.15 for an upstream Mach number of 1.5.) Thus, the pressure disturbances are traveling at the sound velocity relative to the mean flow, satisfying one of the defining features of acoustic waves.

The structure of the acoustic wave is readily apparent at $T = 50$ in Figure 5.4. As predicted in linear theory, the sound wave is quadrupole in nature: the acoustic wavefront is comprised of alternate compression-rarefaction-compression-rarefaction fronts.

Pressure perturbations along radii extending from the vortex center at 10 degree increments are shown in Figure 5.6. This figure quantifies the change in amplitude as a function of the angle from the horizontal, and shows that the peak-to-peak

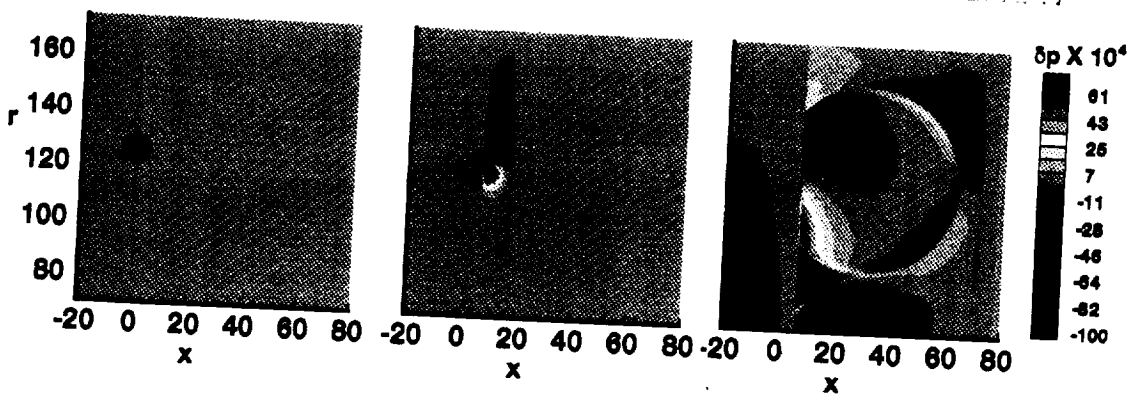

Figure 5.4: Contours of pressure perturbation downstream of the shock at $T = 0$, $T = 8$, and $T = 50$.

pressure amplitude is maximum at $\theta = 50$ and $\theta = -55$ degrees. From this figure, the valley-to-peak measure of the wavelength of the pressure disturbances is seen to be $\lambda \approx 2.8$.

Figure 5.7 shows a carpet plot of the pressure levels downstream of the shock at $T = 50$. The image is processed with Fast [24] and is shown at an angle to clarify the detailed features of the flow field. Note the resolution of the cylindrical acoustic wave, and the complex system of pressure waves between the shock and the cylindrical acoustic wave front.

Figure 5.8 shows the product of the square root of the distance the acoustic wave has traveled (relative to the vortex core) and the peak pressure amplitude along a line extending from the vortex core at 60 degrees from the horizontal passing through the vortex filament as a function of distance from the vortex filament. The product varies significantly at small distances from the core, which is synonymous with early time and proximity to the source, but flattens to an almost constant level at larger distances. This shows that in the far field of these

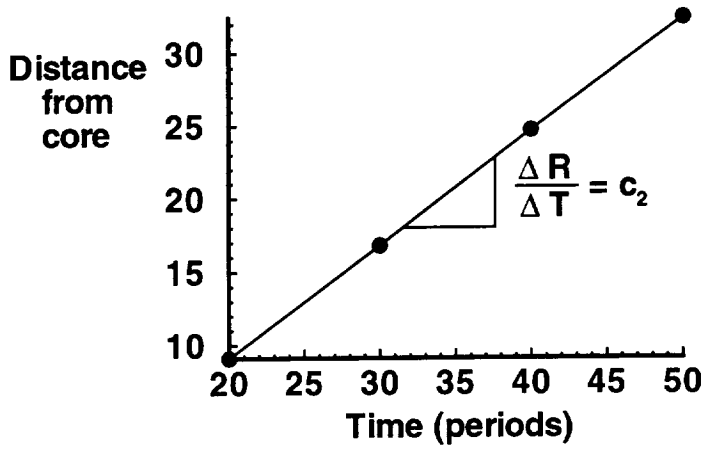

Figure 5.5: Position of the peak pressure perturbation (in core radii from the vortex filament) as a function of time (in periods). The slope of the curve is the sound speed downstream of the shock.

calculations, the sound pressure decays as $\frac{1}{\sqrt{r}}$, which is characteristic of geometrical spreading in two dimensions, commonly known as cylindrical spreading. Although these calculations are performed in an axisymmetric coordinate system which, in general, should allow for three dimensional geometrical spreading of the sound, the presence of the shock wave prohibits the spreading upstream. In realistic flows, where viscosity plays a role in the fluid dynamics, shock waves are finite in extent. In these flows, cylindrical spreading would occur close to the shock wave, while spherical spreading (with p decaying as $\frac{1}{r}$) would occur in the far field. Hardin [23] has shown that in cylindrical coordinates, the sound decay rate is a function of the source size to the distance from the source to the observer. Later it will be shown that the interaction of the vortex ring and shock wave produces a disturbance which travels along the shock, thereby increasing the size of the potential noise

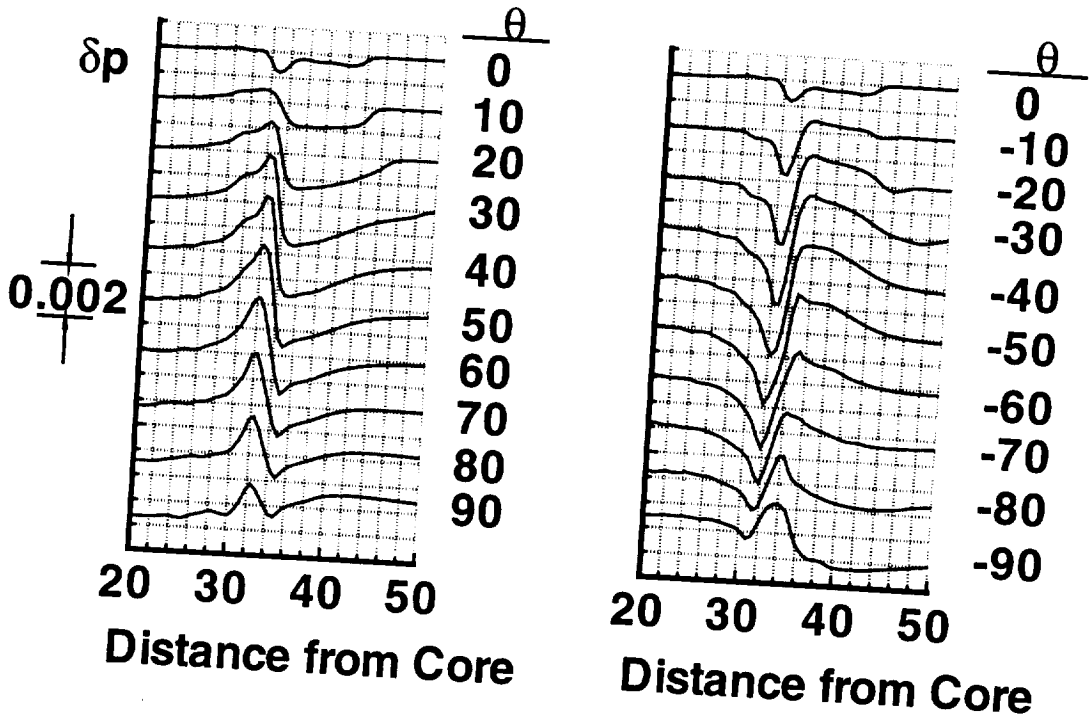

Figure 5.6: Pressure perturbations along radii extending from the vortex core at $x = 30$. Radii are separated by 10 degree increments.

source with increasing time. Thus, the generation and spreading of sound in this interaction is a complicated process, indeed.

An interesting feature apparent in the pressure field resulting from the ring vortex-shock interaction is apparent in the flow field downstream of the shock and below the vortex filament. The ring vortex-shock interaction produces not only the acoustic quadrupole, but also a cusp-shaped pressure wave which connects the portion of the acoustic wave immediately below the vortex filament and the shock wave. This feature was not found in columnar vortex-shock interaction studies ([7], [8], [9], [10], [11], and [12]), and appears to be sensitive to the introduction of the initial condition. Because of computational cost, the vortex is introduced

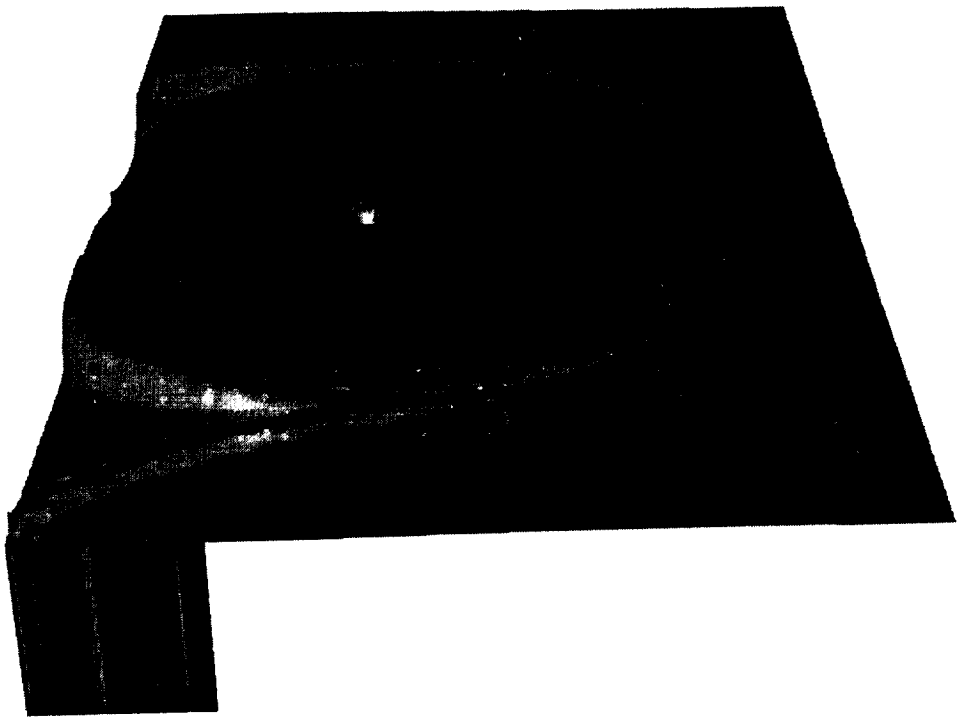

Figure 5.7: Pressure perturbations downstream of the shock at $T = 50$.

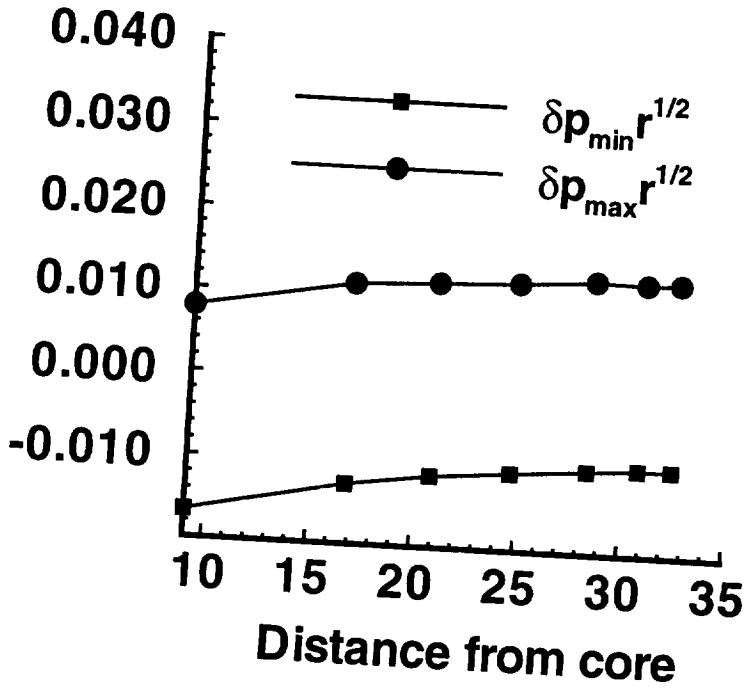

Figure 5.8: Decay rate of the acoustic pressure. The product of the square-root of distance traveled and the peak pressure magnitude is shown to asymptote to a constant value, indicating that the acoustic wave spreads cylindrically.

seven core radii upstream of the shock for most of the calculations presented in this paper. However, to test the effect of the initial distance between the vortex and the shock wave, Δx_1, on the flow field downstream of the shock, a single calculation is presented where the vortex is initially twenty-three core radii upstream of the shock. Figure 5.9 shows the solution downstream of the shock at times $T = 50$ and $T = 66$ for initial shock locations of $x = 7$ and $x = 23$, respectively. In both of these solutions the vortex has traveled approximately 23 core radii after its filament has passed through the shock wave. The cylindrical portion of the pressure field is similar for both initial conditions; however, there are differences in the downstream flow-field. Most notably, the cusp-shaped pressure structure is much larger for the longer time solution ($\Delta x_1 = 23$), indicating that it originates at the beginning of the computation. Further study of this feature is required to quantify the effect of axisymmetry and the initial condition on its structure, and to determine whether it is numerical or physical in nature.

5.3.3 Density

Figure 5.11 shows the change in density of the flow field. At time $T = 0$ the only change in density is associated with the vortex. As the vortex core begins to interact with the shock, density waves appear downstream of the shock. The interesting character of the density waves becomes clear in the final figure of the time sequence. Two types of density perturbations are evident in the figure. Density disturbances associated with the acoustic wave propagate in a nearly circular pattern downstream of the shock. This is to be expected, because acoustic waves are by definition isentropic and there is a clear relationship between the density and pressure ($s = constant = \frac{p}{\rho^\gamma}$). In addition, there are also density disturbances

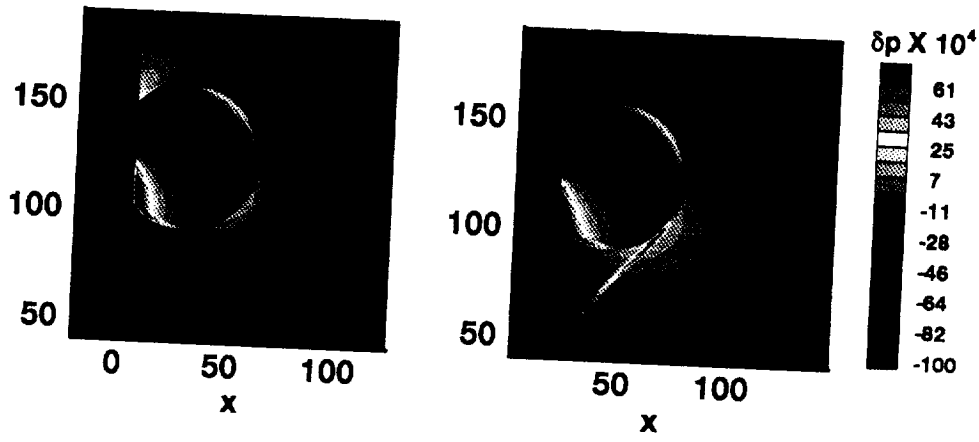

Figure 5.9: Pressure contours downstream for a time $T = 50$ (left figure) and $T = 66$ (right figure). The vortex is located at approximately twenty-three core radii downstream of the shock for both cases. The difference in the solutions is a result of the initial placement of the vortex relative to the shock. In the figure on the left, the vortex is initially seven core radii away from the shock. In the figure on the right, the vortex is initially twenty three core radii away from the shock.

of a convective nature. These density disturbances look like spokes reaching out from the vortex core and terminating at the shock. These disturbances are associated with the entropy waves associated with changes in the shock strength. As the vortex interacts with the shock, the shock wave begins to move. As the shock moves, the change in entropy across the shock is no longer constant, and an entropy wave is generated which convects downstream at the local flow velocity. For the counter clockwise rotating vortex, the portion of the shock above the vortex filament initially moves upstream and the portion of the shock below the filament moves downstream. As time increases, disturbances move away from the interaction point, and their motion along the shock wave creates entropy perturbations which convect downstream at the local flow velocity. These disturbances show a strong resemblance to the features visualized by Naumann and Hermanns [3] in their experiment and described as contact surfaces.

Figure 5.10 shows a digitized version of a Mach-Zehnder interferogram from [3] which illustrates the sound wave and contact surface visualized in the experiment. In the experiment, the interaction is produced as follows. A sharp edged profile is placed in a shock tube. A diaphragm (located to the left of the airfoil) is broken and a weak disturbance travels through the tube and over the trailing edge, producing a starting vortex. Another diaphragm (located at the right of the airfoil) is broken and a shock wave travels towards the vortex. The results of the interaction are shown in Figure 5.10. Because the interaction observed in this experiment is strong, the motion of the shock wave is pronounced and the acoustic wavefront is asymmetrical. The contact surfaces form a curved funnel-shaped structure between the shock wave and the vortex.

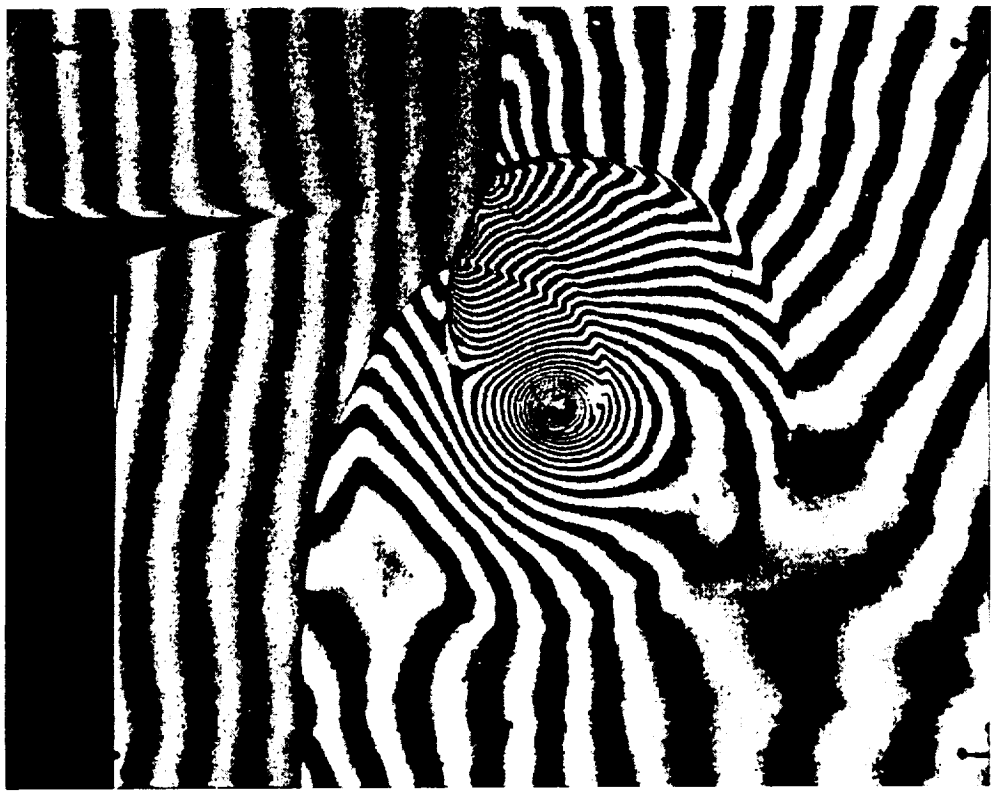

Figure 5.10: Mach-Zehnder interferogram of sound wave and contact surfaces generated shock-vortex interaction. (From [3])

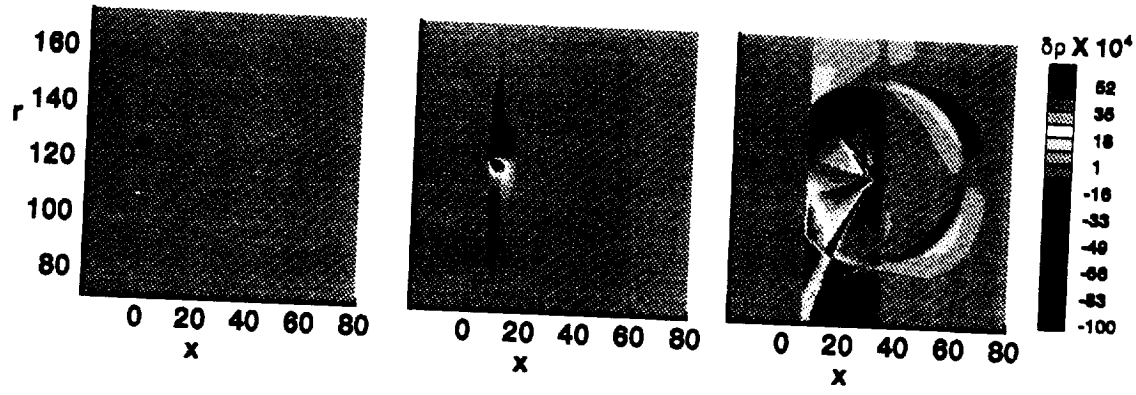

Figure 5.11: Contours of density perturbation downstream of the shock at $T = 0, T = 8$, and $T = 50$.

Figure 5.12 shows a carpet plot of the density at $T = 50$. The sound wave and complex nature of the contact surfaces are clearly visible.

Experiments provide evidence for the physical nature of the contact surfaces observed in these computations. However, earlier analysis in Chapter 3 demonstrated that the computation of slowly moving shock waves produces error which manifests itself primarily in entropy. Therefore, caution must be exercised in the interpretation of the strength of these disturbances. Further analysis is required before the nature of these contact surfaces is validated.

5.3.4 Vorticity

Figure 5.13 shows the change in vorticity. At the initial time, the only vorticity is a circular spike at the vortex core, so this contour plot is not shown. As the vortex interacts with the shock at $T = 8$, vorticity appears downstream. At $T = 50$, the character of the vorticity becomes clearer. The vorticity patterns, like the convective density disturbances, look like the spokes of a wheel radiating from

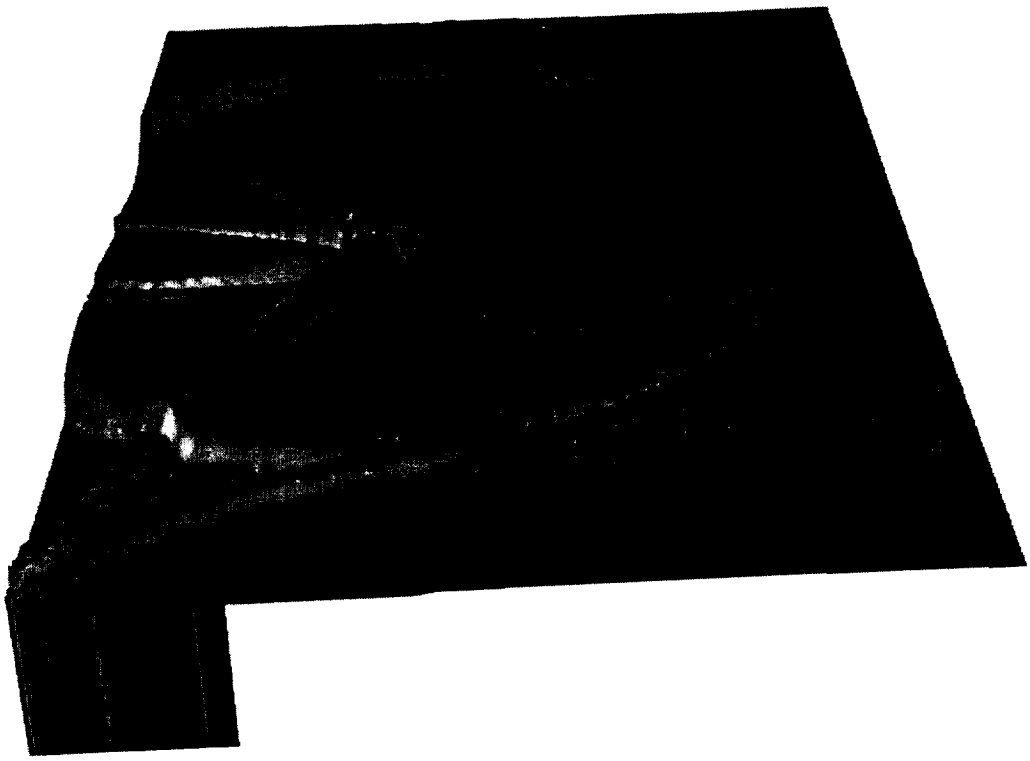

Figure 5.12: Contours of density perturbation downstream of the shock at $T = 50$.

Figure 5.13: Contours of vorticity perturbation downstream of the shock at $T = 8$ and $T = 50$.

the vortex core and terminating at the shock. Zooming in on a region in the immediate vicinity of the vortex core at $T = 50$ (Figure 5.14), it is clear that the lines of constant vorticity are oblong in shape.

5.3.5 Velocity

Figures 5.15 and 5.17 show the changes in the axial and radial components of velocity. Except for small changes in amplitude, the velocity field shows no significant variation as a result of the interaction on this scale. There are, however, very interesting features similar to those observed in the density perturbations when the contour range is decreased. Figure 5.16 shows the change in the axial component of velocity on a smaller contour range. The vortex, acoustic wave, and entropy disturbances are all readily distinguished on this scale.

5.3.6 Entropy

Figure 5.18 shows the change in entropy, defined as $\delta s = s_0 \frac{p}{\rho^\gamma} - s_0$. At the initial time, there is no fluctuation in entropy, since the initial vortex is isentropic.

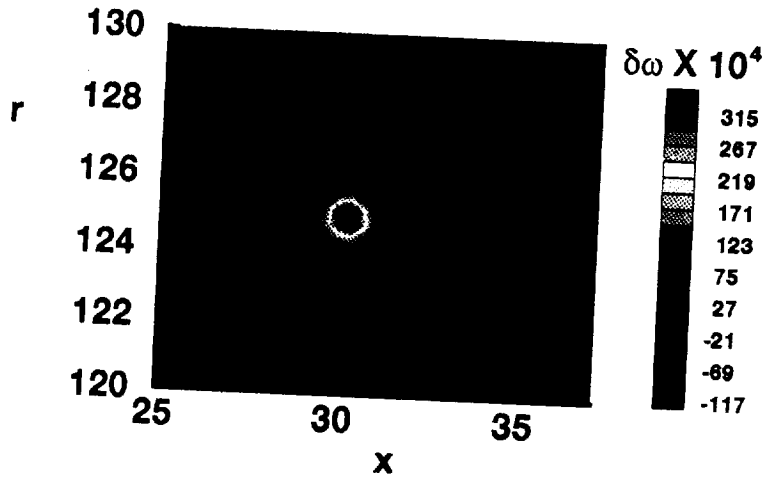

Figure 5.14: Contours of vorticity perturbation in the region immediately surrounding the vortex filament at $T = 50$.

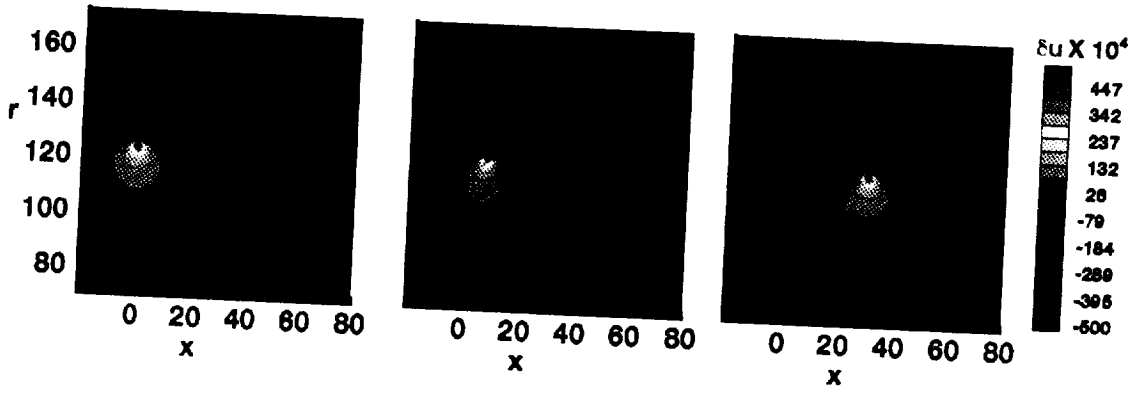

Figure 5.15: Contours of axial velocity perturbation at $T = 0$, $T = 8$, and $T = 50$.

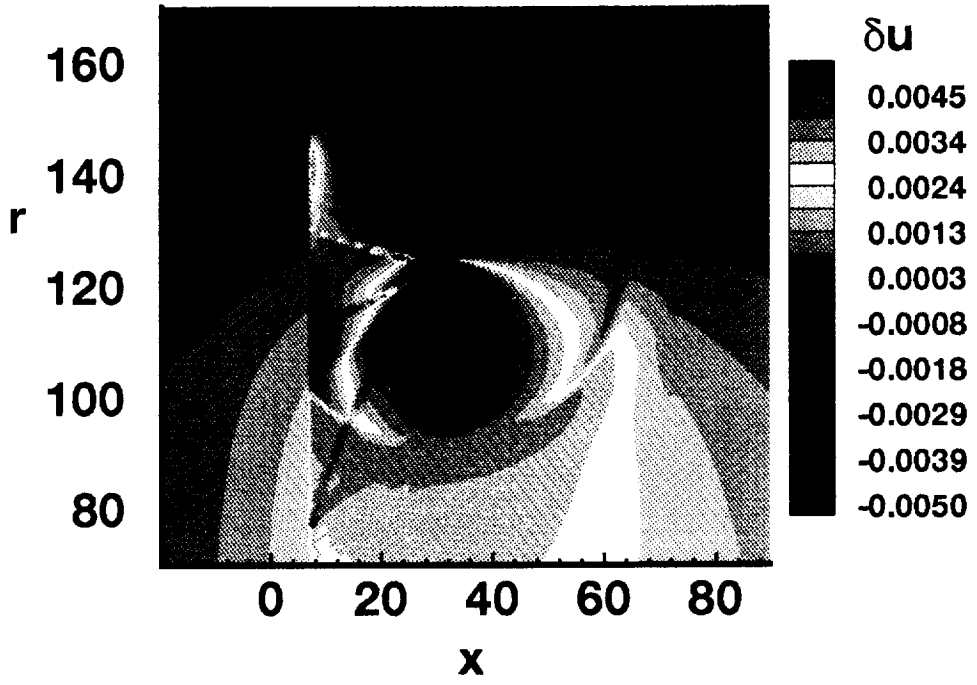

Figure 5.16: Contours of axial velocity perturbation at $T = 50$. The range of the contour levels has been reduced to show the interesting velocity features.

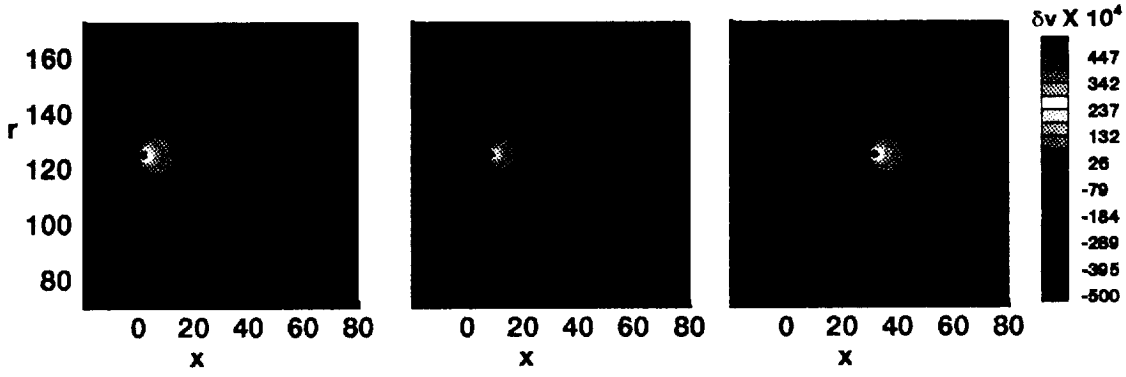

Figure 5.17: Contours of radial velocity perturbation downstream of the shock at $T = 0$, $T = 8$, and $T = 50$.

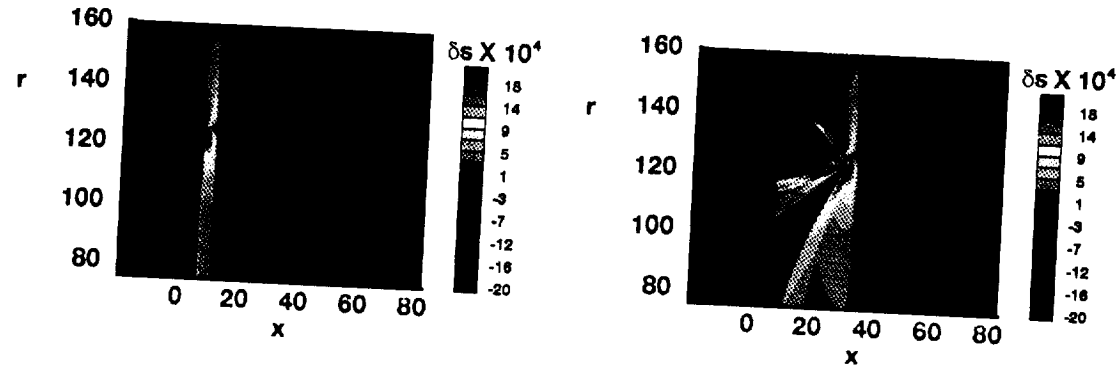

Figure 5.18: Contours of entropy perturbation at $T = 8$ and and $T = 50$.

Therefore, the contour plot at $T = 0$ is not shown. However, as the vortex core interacts with the shock wave, entropy appears downstream. Note that the entropy perturbations correspond to the convective fluctuations in density and vorticity as seen in Figures 5.11 and 5.13.

5.3.7 Discussion

Figures 5.4 through 5.18 illustrate interesting flow features which result from the interaction of a ring vortex and a shock wave. After observing the perturbations in the flow quantities, it is clear that an acoustic wave and contact surfaces result from this interaction. The acoustic wave has the property that it is isentropic, and travels at the sound speed relative to the moving fluid. The contact surfaces do not support a pressure disturbance but do support differences in flow velocity, density, entropy, and vorticity. The disturbances are the result of the interaction. What is it about the interaction which creates these disturbances? From a mathematical perspective, the shock wave is the feature which allows for the coupling of the linear modes (acoustic, entropy, and vorticity). Crocco's Theorem provides the relationship between the flow vorticity and entropy, and from this theorem it can be

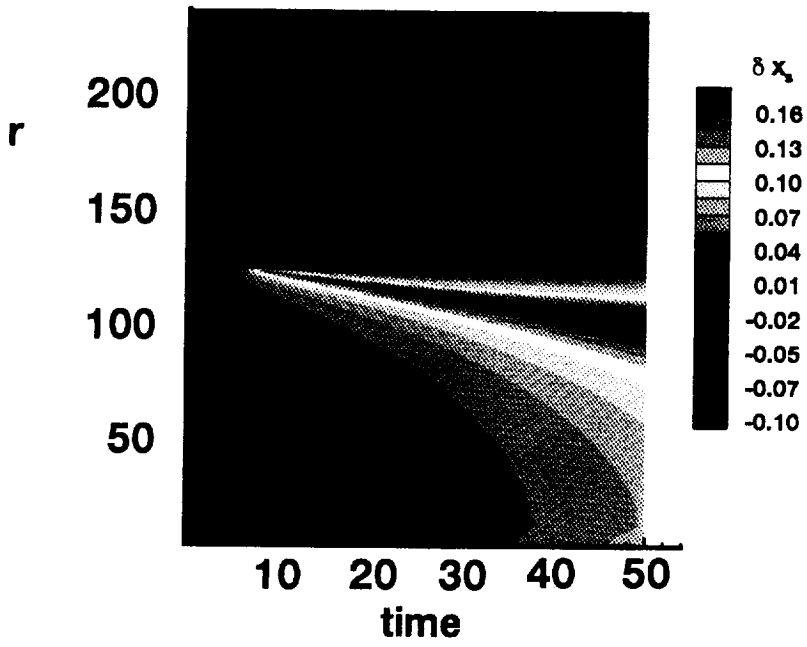

Figure 5.19: Shock displacement as a function of space-time.

shown that vorticity can be generated in the presence of a curved shock. Because the evidence points to the importance of the shock wave in the generation of the acoustic, vortical, and entropy disturbances, a closer observation of the shock dynamics will be made in the next section.

5.3.8 Shock Dynamics

Figure 5.19 shows a space time diagram of the shock displacement. For times $T = 0$ through $T = 6$ the shock position remains nearly fixed as the vortex convects supersonically towards it. Once the vortex core begins to strongly interact with the shock at $T = 6$, the shock motion becomes significant. Figure 5.19 illustrates the nature of the shock displacement as a function of time. A small disturbance on the shock is initiated at $T \approx 6$. The disturbance proceeds to travel both away from and towards the axis of symmetry. The speeds of these waves is approximately the

same in both directions, but the disturbance reaches a local maximum away from the axis of symmetry, but continues to grow towards the axis of symmetry.

Figure 5.20 is included to clarify the details of the shock displacement at various times. This figure shows the axial displacement of the shock as a function of radial position along the shock for $T = 1$, $T = 6$, $T = 10$, $T = 20$, $T = 30$, $T = 40$, and $T = 50$. At $T = 10$, the shock wave has maximum displacement magnitudes of 0.1 and 0.14 in the upstream and downstream directions, respectively. At this early time, the displacement of the shock is limited to a small region around $r = 125$, the radial position of the vortex filament. As time progresses, the maximum shock displacement occurs farther away from the interaction point. The maximum upstream displacement occurs at a time of $T \approx 10$. However, the displacement in the downstream direction continues to increase, even after 50 periods. If one considers the motion of the maximum shock displacements along the shock wave, it is apparent that these disturbances travel away from the vortex-shock interaction point at a particular velocity. By careful examination of the results presented in Figure 5.19, this velocity is found to be ≈ 0.54 core radii per period (which corresponds to a normalized velocity of $\approx .68$). This speed is well below both the upstream and downstream sound speeds (1.0 and 1.15, respectively).

It is interesting that the shock wave displacement continues to increase in the direction towards the center of the ring, while it maximizes and then decreases in the direction away from the ring's axis of symmetry.

Figures 5.19 and 5.20 show the asymmetry in the shock position relative to an axis passing through the vortex filament position at $r = 125$. The portion of the shock closest to the axis of symmetry continues to move downstream over the

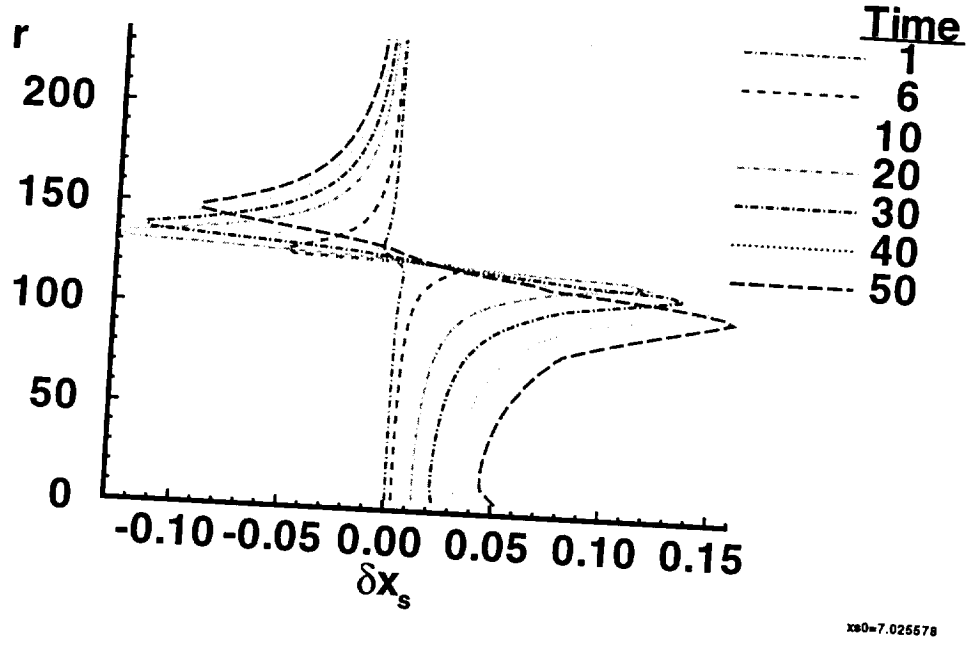

Figure 5.20: Shock displacement as a function of radial distance (on the vertical axis) for $T = 1$, $T = 6$, and $T = 10$ through $T = 50$ in time increments of 10. Positive displacement refers to downstream shock displacement.

time of the calculation. The maximum shock displacement is greater downstream ($\Delta x_s = 0.16$) than upstream ($\Delta x_s = -0.1$).

Figure 5.21 shows the displacement of the shock and the perturbation in density and pressure immediately downstream of the shock (at $x = 7.02$) at $T = 50$. This figure shows that there is a correlation between the disturbances downstream of the shock and the shock displacement. The shock displacement leads the disturbances in pressure and density. The maximum and minimum of the shock displacement correspond to the large jumps in density at $r = 100$ and $r = 150$. The changes in slope of the δx_s vs r curve located at $r = 70$, $r = 120$, and $r = 130$ also correspond to significant high frequency changes in density. This type of fluctuation in pressure occurs only at $r = 70$. Thus, by comparing this figure with the contour plots of Figures 5.4 and 5.11, the spoke-like disturbances in density and vorticity can be related directly to the shock motion and curvature.

5.3.9 Frequency Analysis

In order to obtain information regarding the frequency content of the solution, the Fourier transform is used to transform the time dependent information obtained from the numerical calculation to the frequency domain:

$$P(\omega) = \int_{-\infty}^{+\infty} \delta p(t) e^{-i\omega t} dt \tag{5.7}$$

where δp is the perturbation pressure defined as the difference between the pressure and the mean pressure ($\delta p = p - p_0$), and ω is the cyclic frequency.

This integral is written in discrete form:

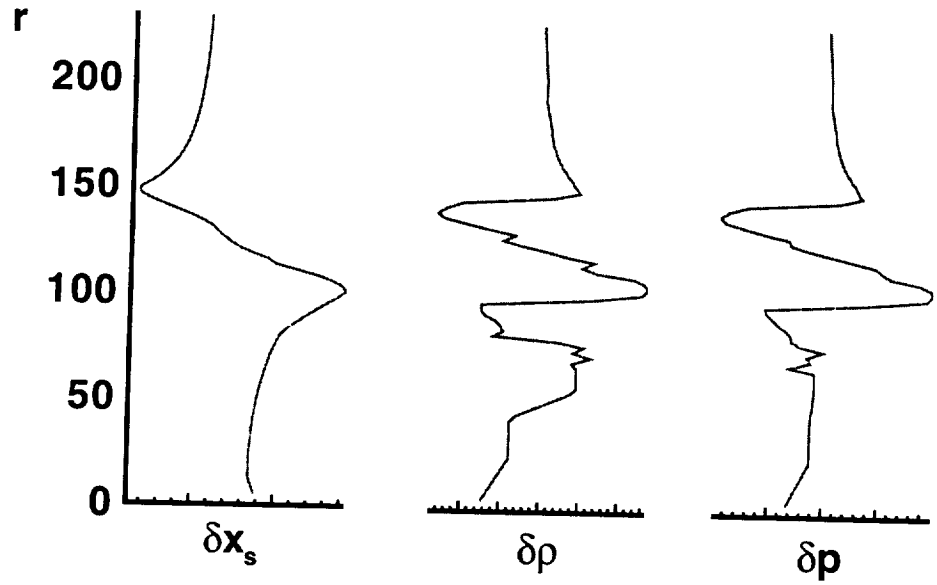

Figure 5.21: Shock displacement and density and pressure perturbations as functions of radial distance (on the vertical axis) for $T = 50$. The density and pressure perturbations are obtained slightly downstream of the shock ($x = 7.02$).

$$P \approx \Delta t \sum_{n=0}^{N-1} p(n\Delta t) e^{-i\omega n \Delta t} \tag{5.8}$$

where Δt is the discrete time interval of the discrete pressure time history, $p(n\Delta t)$, N is the number of points in the time history. The summation Equation 5.8 is computed using the Fast Fourier Transform (FFT) approach. In order to efficiently use the FFT, N must be a power of 2.

In this numerical simulation, solutions were saved at every period (defined previously as $T = \frac{r_c}{u_1}$). Thus, there are 50 discrete representations of pressure in the time history available for analysis at each point in the computational domain. In order to effectively use the FFT approach, the time history at each point at which the spectrum is to be computed is padded with zeros so that the number of discrete values in the time history is a power of two. Padding the time history with zeros does not affect the highest frequency which can be resolved in a discrete approximation to the Fourier transform (the so-called Nyquist frequency), since the Nyquist frequency ω_c is a function only of the temporal increment in the time history, $\omega_c = \frac{\pi}{\Delta t}$. However, padding the time history with zeros does increase the frequency resolution of the spectral estimate.

The increase in frequency resolution provided by zero padding is readily understood by an example [21]. Suppose the original time history T has b elements: $T(n\Delta t), \quad n = 0, 1, 2, ..b-1$. The original time history is then padded with an additional b elements, which are zero: $T(n\Delta t) = 0, \quad n = b, b+1, ...2b-1$. The discrete Fourier transform T_T is then

$$\begin{aligned} T_T(\omega_k) &= \frac{\Delta t}{2\pi} \sum_{n=0}^{2b-1} T(n\Delta t) e^{-i2\pi kn/2b} \\ &= \frac{\Delta t}{2\pi} \sum_{n=0}^{2b-1} T(n\Delta t) e^{-i\pi kn/b} \end{aligned} \tag{5.9}$$

Note that $\omega_k = \frac{\pi k}{b\Delta t}$, $k = 0, 1, 2, ...b$, and the frequency resolution is $\Delta\omega = \frac{\pi}{b\Delta t}$. Similarly, for the original time history without zero padding, $\omega_k = \frac{2\pi k}{b\Delta t}$, $k = 0, 1, 2, ...b/2$, and the frequency resolution is $\Delta\omega = \frac{2\pi}{b\Delta t}$. Thus, the zero padding has the effect of increasing the frequency resolution by a factor of two.

Although it would be sufficient to pad the 50 element time history with 14 zeros to obtain a 64 element time history, each time series was padded with 206 zeros for a total of 256 points in the time history. This provided better frequency resolution necessary for localization of the acoustic energy in the spectrum. The price paid for enhanced frequency resolution is a loss of accuracy. The reader is referred to [21] for details.

Typical sound pressure levels are presented in Figures 5.22 and 5.23. The frequencies on the horizontal axis are normalized by the upstream flow velocity and core radius, to obtain a Strouhal number. In these figures, the effect of the mean flow has been removed from the spectra by subtracting the time average of the pressure from each point in the time history. This removes the energy from the zero frequency bin. The sound pressure level is represented as decibels (dB), per convention. The decibel level is obtained by computing:

$$P(\omega)[dB] = 20log(\frac{P(\omega)}{p_{ref}}) \tag{5.10}$$

where $p_{ref} = 20\mu Pa$ is the conventional acoustic reference pressure.

Figures 5.22 through 5.24 show the sound pressure level at locations along a 45 degree line from the sound source point ($x = 7$, $y = 125$) at 6.08, 11.74 and 23.1 core radii away from the source point. The highest energy levels are in the low frequency range (Strouhal numbers less than 0.1). There are additional peaks at Strouhal numbers of $\approx 0.2, 0.4, 0.6$. The energy in the frequency band of about

0.22 becomes relatively more important than the low frequency energy as distance from the source point is increased. By observation of the time history from which the spectrum is computed, the period of the acoustic wave is determined to be approximately 21 periods. This corresponds to a Strouhal number of $\frac{\omega r_c}{u_1} = \frac{2\pi r_c}{T u_1} = \frac{2\pi(1.)}{(21)(1.5)} = 0.2$. Thus, the energy in the frequency range of 0.22 is associated with the acoustic energy of the signal. The large peaks near the Nyquist frequency (Strouhal No. $= \pi$) are probably due to aliasing. Hardin [20] has shown that for spectral estimates near the Nyquist frequency, ω_c, contributions from $-\omega_c$ can appear, even for a sufficiently sampled time history. Figure 5.25 shows the sound pressure level of the two frequencies 0.025 and 0.2 as a function of distance from the sound source point. The data are taken along a 45 degree line from the horizontal passing through the vortex core at $r = 125$. The data shows a rapid decay in the energy associated with the low frequency energy. The energy decays at about $6dB$ per doubling of distance away from the source. This implies a $\frac{1}{r^2}$ decay rate, which is consistent with the expected decay rate for a vortical pressure field.

The energy at the Strouhal number of 0.22 decays at a lower rate $\approx 3dB$ per doubling of distance, which implies a sound pressure level decay of $\frac{1}{r}$. Because the sound pressure level is a function of the square of the pressure, this result is consistent with the pressure decay rate of $\frac{1}{r^{1/2}}$ observed in Section 5.3.2., and implies cylindrical spreading of the acoustic energy.

5.3.10 Sound Intensity Level

The sound intensity is a vector quantity defined by:

$$\vec{I}(\vec{x}) = \frac{1}{T}\int_0^T \vec{W}\,dt \tag{5.11}$$

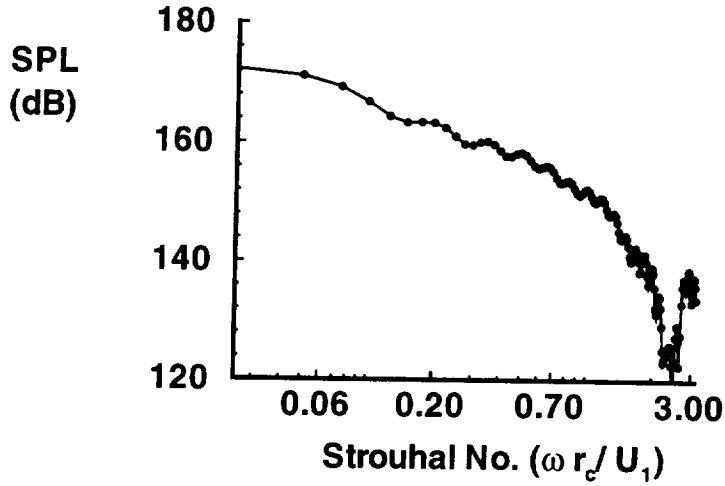

Figure 5.22: Sound pressure level (SPL) pressure as a function of dimensionless frequency. Distance from the source is 6.0811 core radii. Angle from horizontal is 45 degrees.

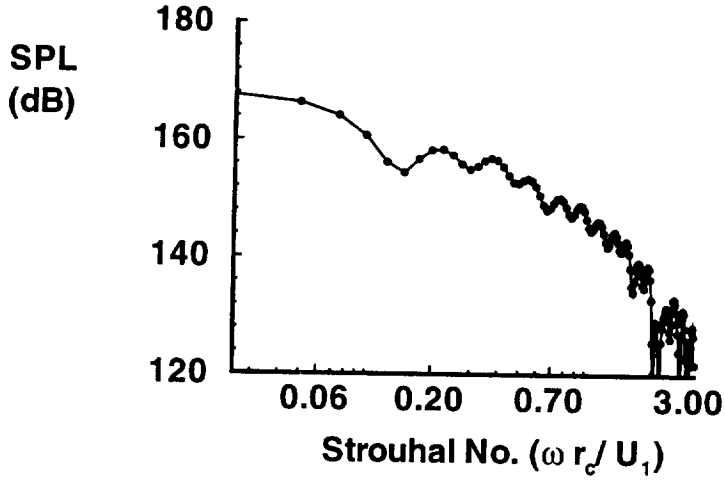

Figure 5.23: Sound pressure level (SPL) as a function of dimensionless frequency. Distance from the source is 11.74 core radii. Angle from horizontal is 45 degrees.

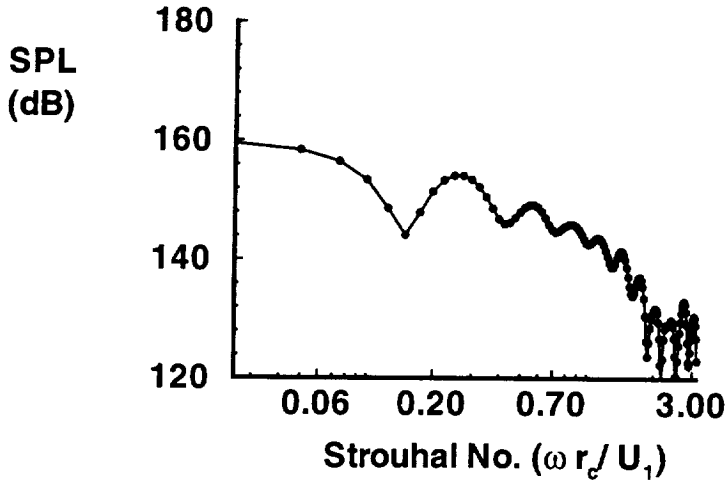

Figure 5.24: Sound pressure level (SPL) as a function of dimensionless frequency. Distance from the source is 23.1 core radii. Angle from horizontal is 45 degrees.

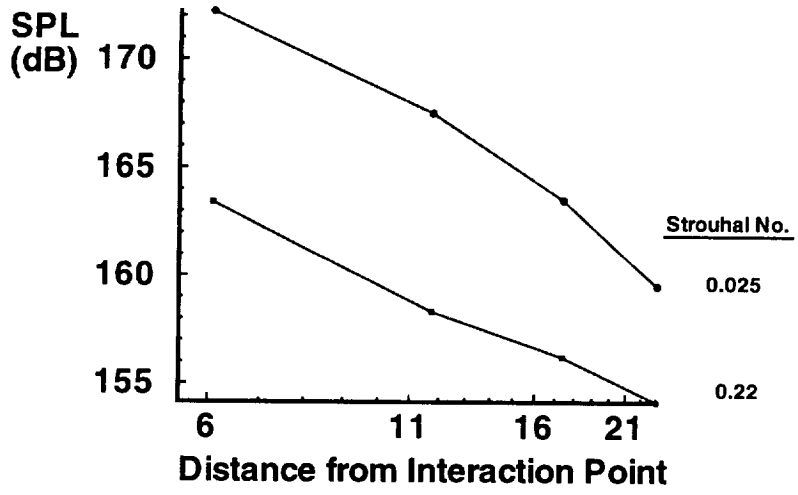

Figure 5.25: Sound pressure level (SPL) as a function of distance from the interaction point. This data is taken along a line at 45 degrees from the point where a horizontal line passing through the vortex filament (r=125) passes through the undisturbed shock.

where T is the period of a periodic disturbance or a sufficiently long time for nonperiodic bounded signals, and $\vec{W}$ is the instantaneous acoustic energy flux vector:

$$\vec{W} = \left(\delta p + \rho_0 \vec{U}_0 \cdot \vec{\delta u}\right)\left(\vec{\delta u} + \frac{\delta\rho}{\rho_0}\vec{U}_0\right)$$

where δp, δu, and $\delta\rho$ are disturbances in pressure, velocity, and density, defined:

$$\delta p = p - p_0$$

$$\delta u = u - u_0$$

$$\delta\rho = \rho - \rho_0$$

and the subscript 0 represents the mean flows state.

Note that in a quiescent medium (where $\vec{U}_0 = 0$), three of the terms in the instantaneous acoustic energy flux vector vanish, and the equation for sound intensity reduces to:

$$\vec{I}_c(\vec{x}) = \frac{1}{T}\int_0^T \delta p \delta\vec{u} dt \tag{5.12}$$

Because the early theoretical development of acoustics was developed for sound disturbances in a quiescent state, this definition will be called the "classical" definition of sound intensity, and it will be labeled with a subscript c to distinguish it from the definition of intensity presented in Equation 5.11. It will be shown later that it can be beneficial to consider the classical definition of sound intensity, even in the presence of mean flow.

In the calculations performed here, the acoustic signal is transient, which provides some difficulty in the interpretation of sound intensity. Because this is a problem which models the periodic convection of turbulent disturbances through

is not *sound* intensity, since most of the disturbances related to the vortex *convect*. The high intensity level shown in this region demonstrates the high correlation between the pressure and velocity disturbances in the vortex. (Some acoustical energy may be generated as the vortex changes shape after its interaction with the shock, but small scale vortical motions were not observed to be a significant sound source in these calculations. This is most clearly seen in Figure 5.7 which shows a carpet plot of pressure fluctuations downstream of the shock. The most significant structure is the ring which has already been identified with the interaction of vortex core with the shock wave. Much less significant pressure disturbances are seen in the center of this acoustic wave, but there are no waves visibly emanating from the vortex.)

The other region of high intensity is seen along the shock wave. The intensity plots show that sound is directed primarily in directions closely aligned with the shock wave, originating at the point of interaction and traveling both towards and away from the axis of symmetry. Both axial and radial components of intensity show high levels along the shock; the region is much narrower in the contour plot of the axial component. The high amplitude of these waves makes it difficult to classify them as acoustic in the classical sense, but because there is no convective velocity in the radial direction, these disturbances are clearly not convective.

A plot of the axial component of sound intensity using the classical definition is shown in Figure 5.27. (Because the mean flow is in the axial direction only, the radial component of classical sound intensity is the same as that shown in Figure 5.26.) The region of high intensity in the vicinity of $r = 125$ is due to the passage of the vortex along this path. Figure 5.27 shows that the intensity

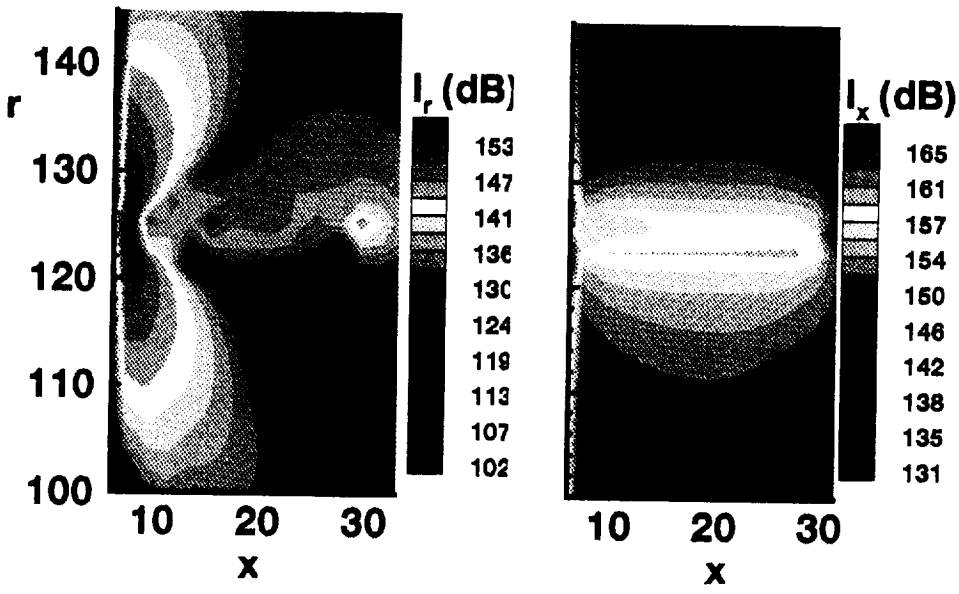

Figure 5.26: Sound Intensity Level. I_r is radial component. I_x is axial component.

has four lobes not related to the convection of the vortex. Two of these lobes are along the shock wave, similar to the results shown in Figure 5.26. However, two additional lobes are seen in this figure. These lobes originate at the point of vortex filament-shock interaction and point at angles of approximately 50 degrees and -55 degrees. The lobe directed at -55 degrees is narrower than the lobe directed at 50 degrees. It is interesting that these regions are not evident in the contours of the full description of the sound intensity (Figure 5.26), because the energy associated with the acoustics is overwhelmed by the contributions from the mean flow terms. The high intensity level along the lobes is significant because it corresponds to the location of the strongest region of the sound wave. (See Figure 5.6.) This indicates that it can be beneficial to consider the classical definition of sound intensity, even in the presence of a mean flow. It is legitimate to apply Equation 5.12 as long as

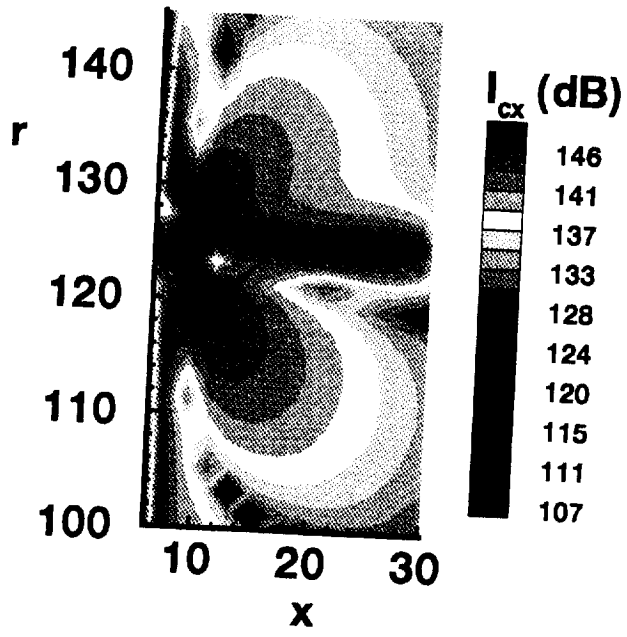

Figure 5.27: Sound Intensity Level. I_{cx} is the axial component of sound intensity level using the classical definition of sound intensity. Note that in this definition, the primary directivity of the sound wave is along the shock wave and downstream at angles of approximately ± 50 degrees.

it is not used to draw conclusions about acoustic energy conservation.

5.3.11 Effect of Mach Number on Directivity

In order to determine the effect of Mach number on the directivity of the pressure disturbances, a series of computations was performed where all flow parameters were held fixed except the upstream Mach number. The pre-shock Mach numbers studied were: M = 1.1, 1.3, 1.4, 1.5, and 1.7. These Mach numbers were chosen because they are within the range of practical interest. The sound intensity level was computed over this Mach number range. The directivity angles as a function of shock strength are plotted in Figure 5.28. The figure shows the angles of the four primary beaming directions. The change in lobe direction is most significant for the lobes closely aligned along the shock. As the Mach number increases, these lobe angles approach ± 90 degrees.

5.3.12 Effect of Flow Mach Number on Sound Pressure Level

Because of the complexities in defining and computing the sound intensity level for a transient signal in the presence of a mean flow, and because the human ear responds to pressure fluctuations, a study of the effect of flow Mach number on the sound pressure level is presented here. In this study, sound pressure level is computed for a point in the acoustic far field (defined to be one wavelength away from the source) at a distance of 23 core radii from the interaction point at an angle of $\theta = 50$ degrees. In these calculations, the sound pressure level is computed by:

$$SPL = 20Log\left[\frac{p_{rms}}{p_{ref}}\right] \tag{5.13}$$

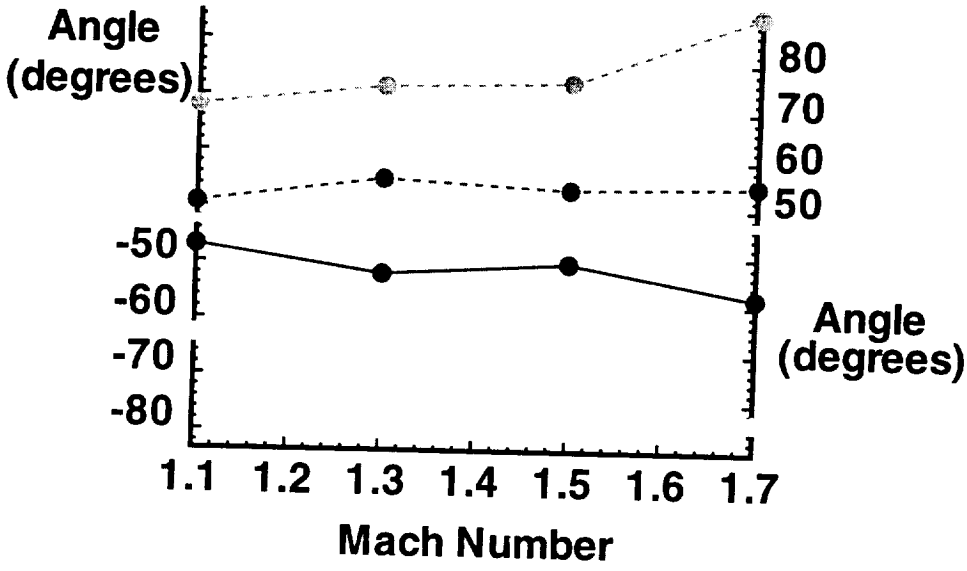

Figure 5.28: Directivity Angles as a Function of Upstream Mach Number. The upper curve corresponds to the intensity lobe closest to the shock above the vortex filament; the second curve from the top corresponds to the intensity lobe to the far right of the shock and above the filament; the third line from the top corresponds to the intensity lobe to the far right of the shock and below the vortex filament position, and the bottom curve corresponds to the intensity lobe closest to the shock and below the vortex filament.

where $p_{rms} = sqrt\frac{1}{T}\int_0^T pdt$, and where T is the period of the acoustic signal. Because this calculation is performed in the far field, the acoustic wave is readily distinguished from hydrodynamic disturbances. The result of this study is presented in Figure 5.29 which shows sound pressure level as a function of $\beta = \sqrt{M^2 - 1}$, for Mach numbers in the range $1.1 \leq M \leq 1.5$. In this figure, the solid line with small dots represents the sound pressure level obtained from the time histories provided by the ENO computations of the ring vortex - shock interaction. The large circles are the experimental measurements obtained by Seiner and Norum [19] for shock noise of an underexpanded supersonic jet, measured at a distance of 12 feet from the jet centerline (approximately 146 jet radii from the source). The dashed line shows the trend first observed by Harper-Bourne and Fisher [18] that the sound pressure level of shock noise in imperfectly expanded supersonic jets is proportional to β^4 over a large range of flow Mach numbers. The slope of the sound presure level versus β curve very nearly matches the slope of the experimental results for shock noise in supersonic jets. This is a significant result because it shows that this simple model for shock noise generation can predict the effect of Mach number on shock noise observed in experiment.

Although this model correctly reproduces the trend in sound intensity level as a function of shock strength, it does not reproduce the actual sound amplitude, even when differences in the distance between the sound source and measurement location are accounted for. This is not surprising since shock noise measured during an experiment is the result of many interactions of turbulent structures of a variety of sizes and strengths with a sequence of shock waves of decaying strength, and at varying angles to the flow; this calculation is the result of only a single interaction.

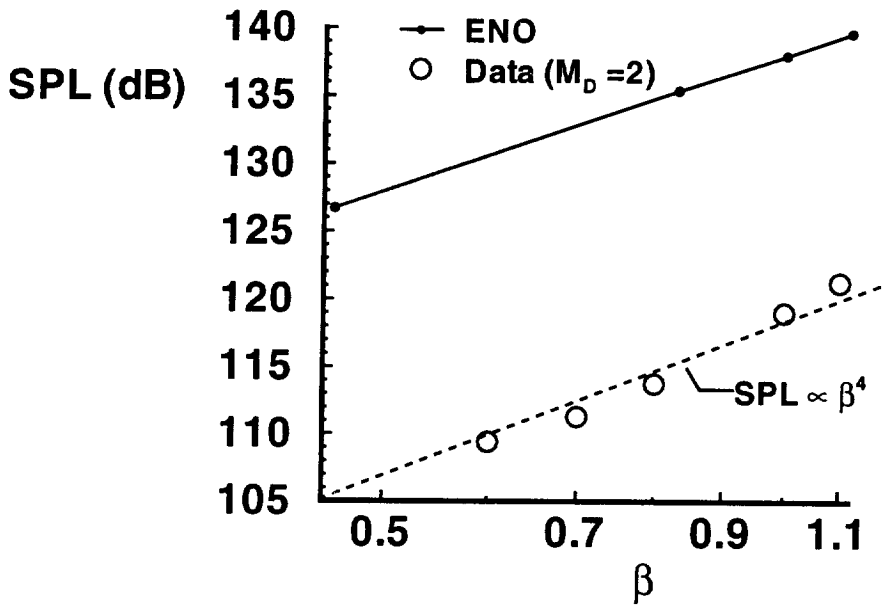

Figure 5.29: Sound pressure level (SPL) as a function β, where β is a measure of upstream Mach number.

5.4 Strong Interaction

The results presented in this section are for the interaction of a strong vortex with a shock wave. For all the results presented in this section, the upstream Mach number is 1.5 and the strength of the vortex is $\Gamma = 5.5$. Thus, this vortex is $7\frac{1}{3}$ times stronger than the vortex studied in the previous sections. When the vortex strength increases, the pressure disturbances generated downstream of the shock increase in magnitude, as illustrated by Figure 5.30 which shows contour plots of the pressure disturbances at $T = 50$. The actual range of the pressure disturbances are on the order of 1, but, for the plot, the range of contours was chosen to be from $-.01$ to .007 so that direct comparison with Figure 5.4 can be made. It is interesting to compare the results of Figure 5.30 with Figure 5.4. In both figures, a sound wave and a cusp-like pressure disturbance are apparent downstream of the shock. However, the sound wave is much stronger in the strong vortex-shock interaction case (Figure 5.30), and on this plot contour scale, additional pressure structures are visible downstream and below the vortex filament.

Figure 5.31 shows pressure perturbation along radii extending from the vortex center at 10 degree increments. This figure shows that the peak-to-peak pressure amplitude is a maximum at 55 degrees and -55 degrees, as in the case for $\Gamma = 0.75$. From this figure, the valley-to-peak measure of the wavelength is found to be ≈ 2.5. By comparison with Figure 5.6, it is clear that the disturbances for the strong vortex interaction case are almost an order of magnitude larger. For example, the amplitude of the peak disturbance at 50 degrees is 10.2 times larger for the strong interaction case ($\Gamma = 5.5$) than the weak interaction case ($\Gamma = .75$). Thus, the acoustic pressure p scales as the vortex strength Γ.

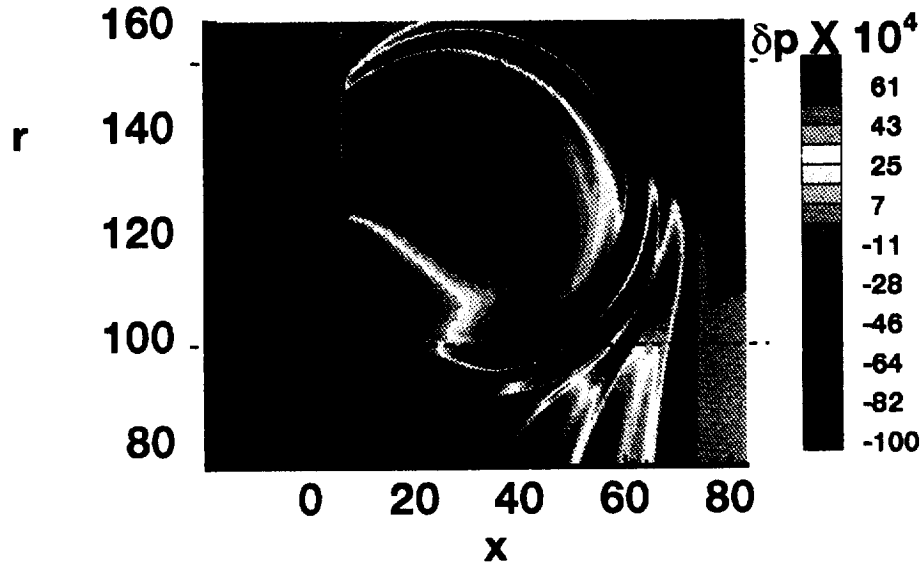

Figure 5.30: Contours of pressure perturbation downstream of the shock at $T = 50$. Vortex rotation is in a counter-clockwise sense. Vortex strength is $\Gamma = 5.5$.

It is interesting to note that the pressure disturbances immediately downstream of the shock form very steep gradients. These gradients may be considered to be shock waves, and have been referred to as "reflected shocks" [25]. Figure 5.32 shows the distribution of perturbation pressure as a function of distance from the initial shock position at locations above and below the vortex filament. It is clear that there are significant jumps in pressure downstream of the original shock wave, especially below the vortex filament. The formation of steep gradients downstream requires that the algorithm used in the calculation is robust.

Figure 5.33 shows contours of the density perturbations downstream of the shock. The same types of features present in the $\Gamma = .75$ case are present here, but the strength of these features is now enhanced.

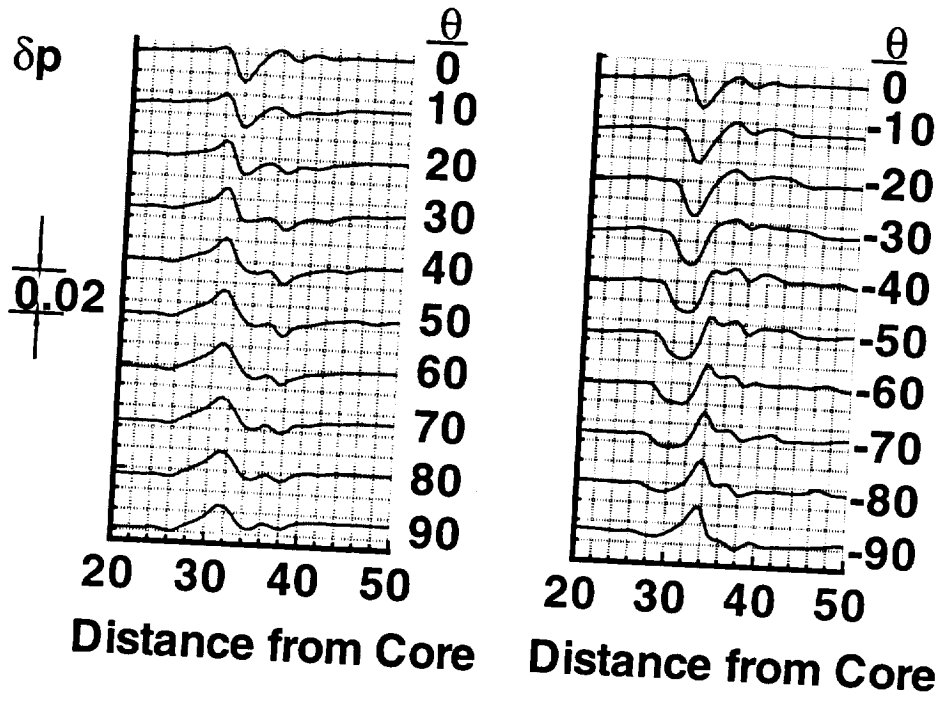

Figure 5.31: Pressure perturbations along radii extending from the vortex core at $x = 30$. Radii are separated by 10 degree increments. Vortex strength is $\Gamma = 5.5$.

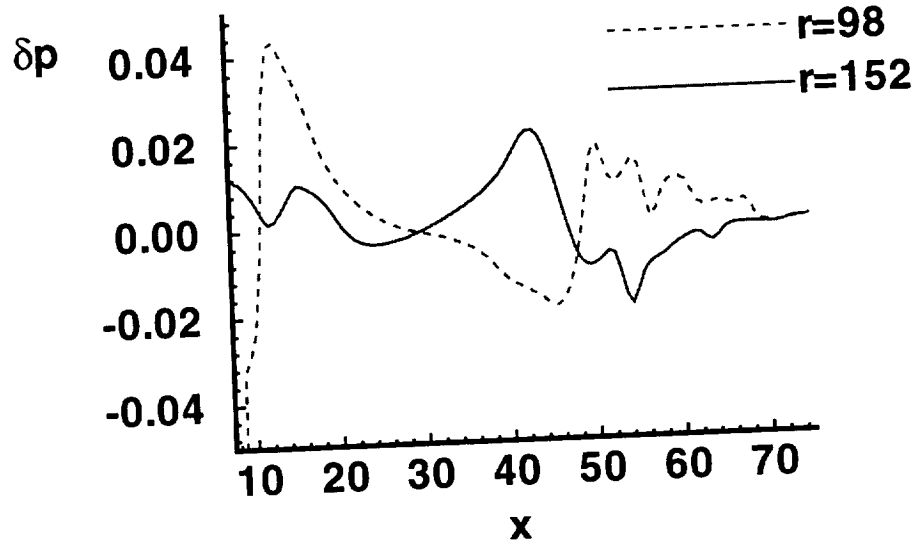

Figure 5.32: Pressure perturbations as functions of axial position at $T = 50$. Dashed curve represents pressure perturbation along the line $r = 98$, below the vortex filament. Solid curve represents pressure perturbation along the line $r = 158$, above the vortex filament.

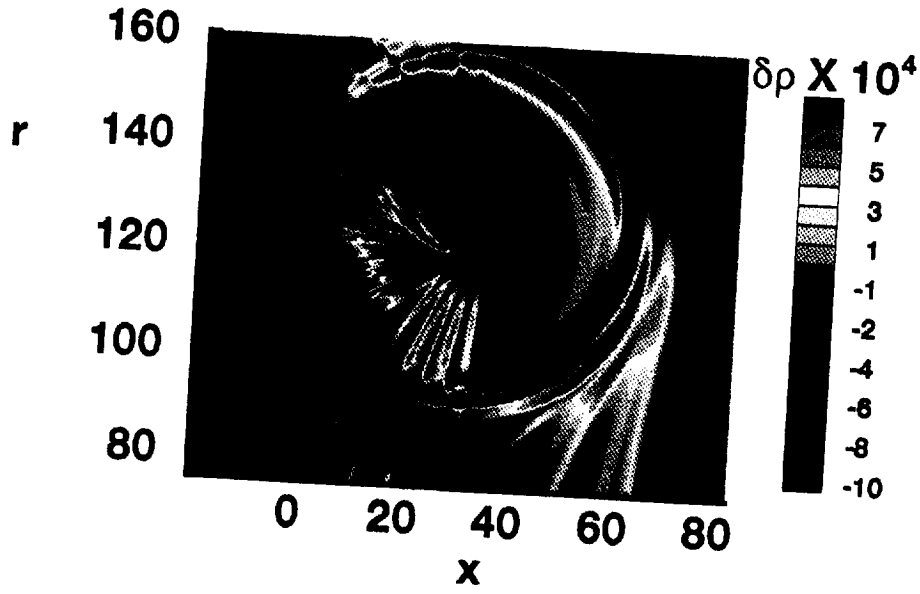

Figure 5.33: Contours of density perturbation downstream of the shock at $T = 50$. Vortex rotation is in a counter-clockwise sense. Vortex strength is $\Gamma = 5.5$.

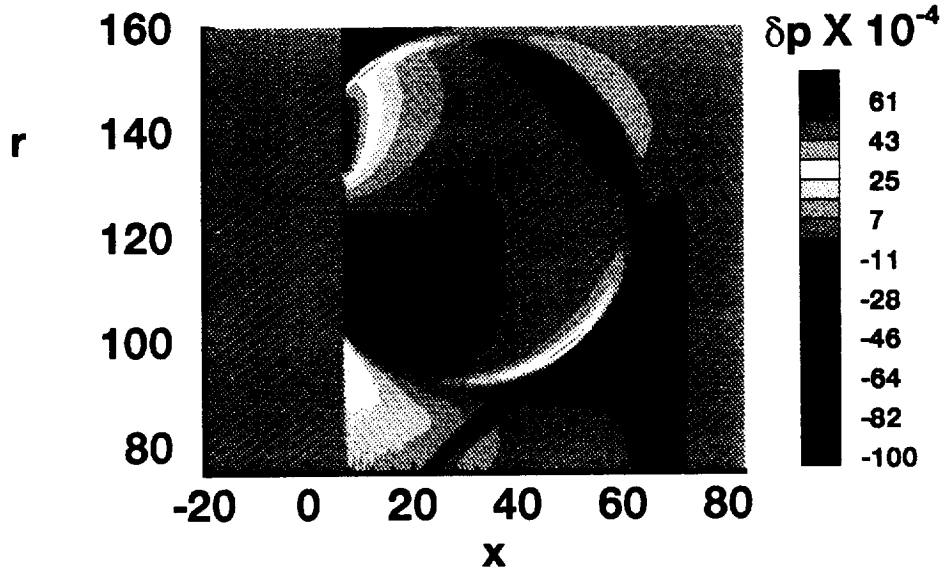

Figure 5.34: Contours of pressure perturbation downstream of the shock at $T = 50$. Vortex rotation is in a clockwise sense.

5.5 Typical Interaction-Clockwise Vortex

In this section, results are presented for the interaction of a clock-wise rotating vortex with a shock. This case is not representative of the physics of the interaction of vortices in the jet shear layer with shock waves, but is included for completeness. This type of interaction could model wake flow- shock interaction, such as the wake of a helicopter blade interacting with a shock on the subsequent blade.

Figure 5.34 shows contours of pressure for the case of vortex rotating in a clockwise sense with a shock wave. The strength of the vortex in this case is $\Gamma = -0.75$, and the Mach number upstream of the shock is $M = 1.5$.

Note that this case is directly analogous to the case presented in Section 5.3, except for the sign of the vortex circulation. Comparison of Figure 5.34 with Figure

5.4 shows that the contours of pressure perturbation are quite similar, except that the regions of compression (rarefaction) in Figure 5.34 are regions of rarefaction (compression) in Figure 5.4. The difference in the rotation sense of the vortex results in a different response of the shock wave, which in turn results in a difference in the sign of the pressure disturbance downstream. As shown in Figure 5.19, a CCW rotating vortex causes the shock to move upstream in the region above the vortex filament and downstream below the vortex filament. For the clockwise rotation, the shock wave moves downstream above the vortex filament and upstream below the vortex filament, as shown in 5.35. Figure 5.36 clearly shows that the shock displacement is significantly greater upstream than downstream.

The downstream pressure disturbances resulting from the CW and CCW vortices are not perfect images of each other about the vortex filament, the only difference being the sign of the disturbance. Clearly, the cusp-structure described in Section 5.3 connects the acoustic disturbance to a position on the shock near the axis of symmetry in both cases.

There is also asymmetry of the acoustic disturbances. Figure 5.37 shows the pressure perturbations along radii extending from the vortex core at $\pm 40, \pm 50$, and ± 60 degrees. The dashed lines represent results from the CCW vortex and the solid lines represent results from the clock-wise rotating vortex. For ease of comparison, the results have been plotted such that the pressure disturbance associated with the positive angle of the clockwise vortex is compared with the negative angle of the CCW rotating vortex. The results show good agreement between the pressure peak at the positive angle for the clockwise vortex and the negative angle for the CCW vortex. However, there is a significant difference in the maximum

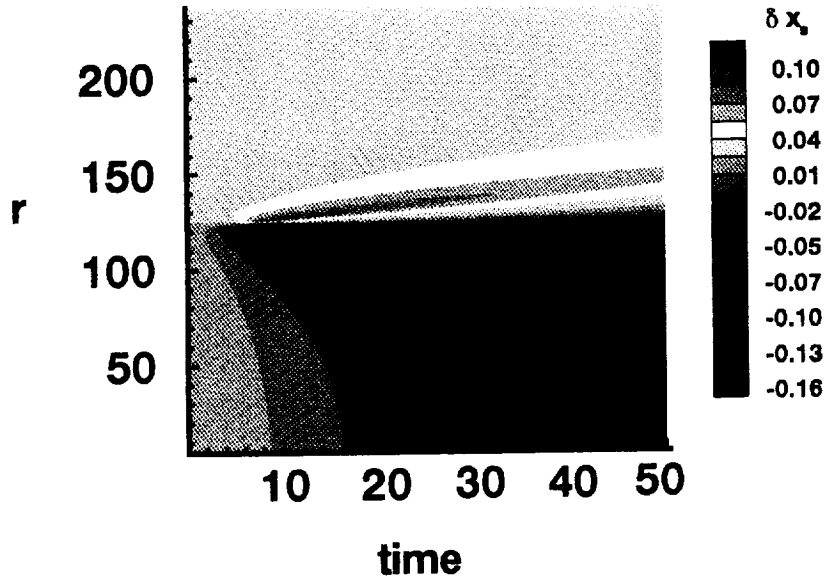

Figure 5.35: Shock displacement as a function of space-time.

pressure amplitude of the disturbances which correspond to the clockwise vortex at a negative angle and the CCW vortex at the positive angle. For these cases, the clockwise rotating vortex generates a larger pressure disturbance. The largest difference is seen to be 156 % for the sound disturbance traveling at ± 60 degrees from the horizontal.

5.6 Effect of Vortex Core Size

To show the effect of vortex core size relative to the vortex ring size, a study is included in which the ratio of the core radius to ring radius is $\frac{1}{250}$. Figure 5.38 shows the contours of change in pressure at $T = 50$ for this case. The range of pressure levels in the contour plot is kept the same as in Figure 5.4 for direct comparison. The strength and wavelength of the acoustic waves are essentially identical to

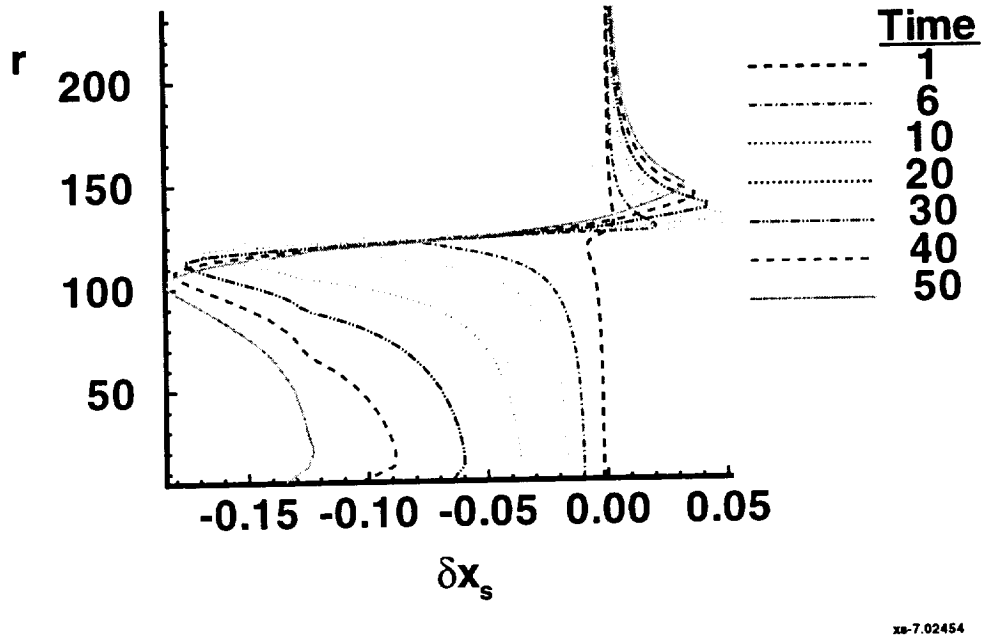

Figure 5.36: Shock displacement as a function of radial distance (on the vertical axis) for $T = 1$, $T = 6$, and $T = 10$ through $T = 50$ in increments of 10 for a clock-wise rotating vortex. core at $x = 30$, $y = 125$. Results are shown for radii at $\pm 40, \pm 50$ and ± 60 degrees. The solid lines represent solutions for the clock-wise rotating vortex. The dashed lines represent solutions for the CCW rotating vortex.

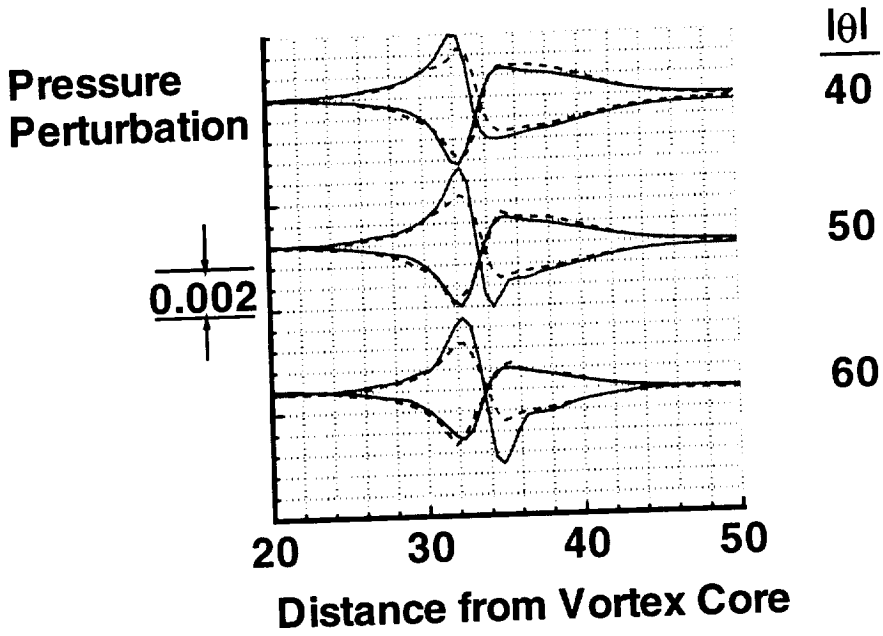

Figure 5.37: Pressure perturbations along radii extending from the vortex core at $x = 30$, $y = 125$. Results are shown for radii at $\pm 40, \pm 50$ and ± 60 degrees. The solid lines represent solutions for the clock-wise rotating vortex. The dashed lines represent solutions for the CCW rotating vortex.

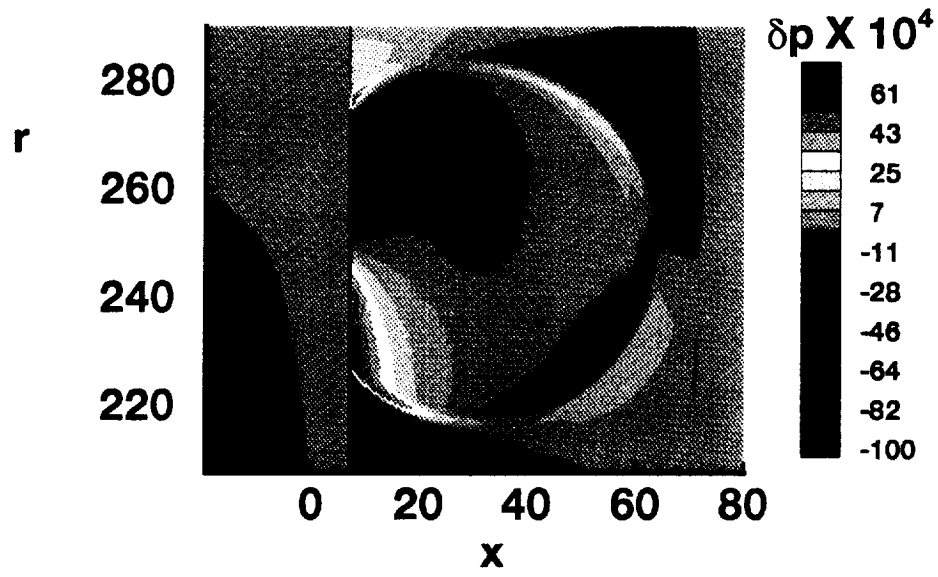

Figure 5.38: Contours of pressure perturbation for a case where the strength of the vortex is $\Gamma = 0.75$, the Mach number upstream of the shock is $M = 1.5$, and the ratio of the vortex core radius to the ring radius is $\frac{1}{250}$.

those in the case where the ratio of core radius to ring radius is $\frac{1}{125}$. The primary difference between the results is the fact that the cusp-like structure so apparent in the results of Figure 5.4 is no longer visible on the contour plot. This indicates that the presence of this wave may be related to axisymmetry. As the vortex ring becomes larger relative to the core size, the resultant wave structures more closely resemble those generated in a two-dimensional planar interaction which does not show the cusp-like structure.

5.7 Conclusions

In this chapter, the interaction of a ring vortex with a shock wave is presented as a simple model for a mechanism responsible for generating shock noise in imperfectly expanded supersonic jets. This model was inspired by the early works of Ribner [4] [6] and Moore [5] who considered two dimensional interactions of disturbances with shock waves in the context of linear theory, but differs from these pioneering studies because the interaction considered is axisymmetric, to more closely model the interaction of axisymmetric turbulent structures within axisymmetric jets, and the computational nature of the present study provides a tool for solving the nonlinear equations governing the fluid dynamics of this very complex interaction.

An effort was made in the design of these calculations to model the physical parameters of an imperfectly expanded jet. The size of the vortex core relative to the vortex ring radius was small because of numerical considerations, so flow parameters were chosen to model the interaction of a turbulent disturbance with a shock wave in the first shock cell. The magnitude of the vortex strength and the sense of the vortex rotation were chosen to be consistent with those observed in experiments. The range of Mach numbers studied was within the range for practical nozzles.

Observations of the evolution of perturbations in pressure, density, entropy, vorticity, and velocity downstream of the shock wave during an interaction are made. Observation of these flow quantities leads to the conclusion that sound, entropy, and vorticity are generated downstream of the shock wave during the interaction process. The sound wave is isentropic and propagates downstream at the sum of the convection and sound speeds. Contact surfaces are formed during

the interaction process. These disturbances do not support a difference in pressure, but do support differences in density, entropy, and vorticity. Both sound waves and contact surfaces have been observed in experimental studies of shock-vortex interaction. It is believed that these are the first calculations performed with enough resolution to show the presence of the contact surfaces downstream of the shock for these flows. Contact surfaces have been observed in experiments, which provides evidence for the physical nature of these disturbances, but, as discussed in Chapter 3, numerical error associated with moving shock waves may readily manifest itself in entropy, so further analysis is necessary in order to validate the strength of the computed contact disturbances.

The structure of the contact surfaces is related to the shock dynamics. The contact disturbances are observed to be generated by a wave which is initiated during the interaction and travels along the shock both towards and away from the center of the vortex ring. The motion of the shock corresponding to the wave traveling along its length generates entropy and vorticity disturbances. Pressure perturbations are also observed to originate at the locations of large shock motion.

Analysis of the data provides further insight into the physics of the interaction. A frequency analysis suggests that the sound wave generated in these computations decays as a cylindrical wave. This is due to the presence of the shock wave which acts as a barrier to sound spreading upstream of the shock. An analysis of sound intensity level provides insights into the directive nature of the sound wave. High intensity levels are observed close to the shock wave and in downstream directions at angles of approximately 50 and -55 degrees from a horizontal axis through the vortex filament for the case where the upstream Mach number is 1.5.

Additional studies of the interaction of a strong vortex with a shock wave validated the robustness of the numerical code used in this work. The interaction produced extremely high gradients in the flow downstream of the shock, and the computation maintained stability.

The sound generated by clockwise and counter-clockwise rotating vortices was compared. It was found that the structure of the alternating compression-rarefaction zones along the sound wave changed sign when the sense of the vortex rotation changed. (Regions of compression resulting from the clockwise vortex became regions of rarefaction for the counter clock-wise vortex, and vice verse.) It is also observed that the clockwise vortex generates disturbances which can be significantly larger in amplitude. The peak pressure perturbation resulting from the interaction of the clockwise rotating vortex with the shock produces pressure levels up to 156 % higher than the counter-clockwise rotating vortex.

A study of the effect of the ratio of core size to ring size is also performed. This study shows that the effects of axisymmetry are reduced when the core radius size is decreased relative to ring radius.

A study of the effect of flow Mach number on the sound pressure level provided a significant result. It was found that the sound pressure level increased with Mach number, and the rate of this increase corresponds closely to that observed in experimental data of shock noise of supersonic jets. This result implies that the interaction of a vortex ring with a shock wave is a dominant physical process in shock noise generation in supersonic jets.

Bibliography

[1] M.A. Hollingsworth and E.J. Richards, "A Schlieren Study of the Interaction Between a Vortex and a Shock Wave in a Shock Tube," Aeronautical Research Council Report 17985, Fluid Motion Subcommittee, 2323, London, 1955.

[2] M.A. Hollingsworth and E.J. Richards, "On the Sound Generated by the Interaction of a Vortex and a Shock Wave," Aeronautical Research Council Report 18257, Fluid Motion Subcommittee, 2371, London, 1956.

[3] A. Naumann and E. Hermanns, "On the Interaction Between a Shock Wave and a Vortex Field," AGARD -CP-131, 1973.

[4] H.S. Ribner, "Convection of a Pattern of Vorticity Through a Shock Wave," NACA report 1164, 1954.

[5] F.K. Moore, "Unsteady Oblique Interaction of a Shock Wave with a Plane Disturbance," NACA Report 1165, 1954.

[6] H.S. Ribner, "Shock-Turbulence Interaction and the Generation of Noise," NACA Report 1233, 1955.

[7] S.P. Pao and M.D. Salas, "A Numerical Study of Two-Dimensional Shock Vortex Interaction," AIAA paper AIAA-81-1205, presented at 14th Fluid and Plasma Dynamics Conference, June 1981.

[8] M.D. Salas, T.A. Zang, and M.Y. Hussaini, "Shock-Fitted Euler Solutions to Shock-Vortex Interaction," *Proceedings of the 8th International Conference on Numerical Methods in Fluid Dynamics*, edited by E. Drause, Springer-Verlag, NY, 1982, pp.461-467.

[9] M.Y. Hussaini, D.A. Kopriva, M.D. Salas, T.A. Zang, "Spectral Methods for the Euler Equations: Part II, Chebychev Method and Shock Fitting," *AIAA Journal*, Vol. 23, No. 2, 1985, pp.234-240.

[10] D.A. Kopriva, T.A. Zang, M.D. Salas, and M.Y. Hussaini, "Pseudospectral Solution of Two-Dimensional Gas Dynamic Problems," *Proceedings of the 5th GAMM-Conf. on Numerical Methods in Fluid Mechanics*, edited by M. Pandolfi and R. Piva, Vieweg and Son, Braunshweig , Germany, 1983, pp.185-192.

[11] K.R. Meadows, A. Kumar and M.Y. Hussaini, "Computational Study on the Interaction Between a Vortex and a Shock Wave," AIAA Journal, Volume 29, Number 2, Feb. 1991, pp. 174-179.

[12] Jay Casper, "A Finite-Volume Application of High-Order ENO Schemes to Two-Dimensional Boundary-Value Problems," AIAA paper AIAA 91-0631, 29th Aerospace Sciences Meeting, Jan. 1991.

[13] H. Atkins and Jay Casper, "Non-reflective Boundary Conditions for High-Order Methods," AIAA paper 93-0152, presented at AIAA 31st Aerospace Sciences Meeting, Reno, NV, 1993.

[14] Sir Horace Lamb, Hydrodynamics, Cambridge University Press, 1932, p. 237, 246.

[15] Milton Abramowitz and Irene S. Stegun, eds., Handbook of Mathematical Functions, 9^{th} printing, Dover Publications, Inc., New York, pp.591-592, Eqns. 17.3.36 & 17.3.34, 1970.

[16] James M. Robertson, Hydrodynamics in Theory and Application, Prentice-Hall, NJ, 1965.

[17] John M. Seiner, "Advances in High Speed Jet Aeroacoustics," AIAA paper AIAA-84-2275, AIAA/NASA 9th Aeroacoustics Conference, 1984.

[18] M. Harper-Bourne and M.J. Fisher, "The Noise from Shock Waves in Supersonic Jets," AGARD-CP-131, 1973.

[19] J.M.Seiner and T.D. Norum, "Aerodynamic Aspects of Shock Containing Jet Plumes," AIAA-80-0965, presented at AIAA 6th Aeroacoustics Conference, Hartford, CT, 1980.

[20] Jay C. Hardin, "An Additional Source of Uncertainty and Bias in Digital Spectral Estimates Near the Nyquist Frequency," Journal of Sound and Vibration, Vol. 110, No. 3, pp.533-537, 1986.

[21] Jay C. Hardin, Introduction to Time Series Analysis, NASA Reference Publication 1145, March 1986.

[22] J. M. Seiner, private communications.

[23] Jay C. Hardin and D.S. Pope, "High Reynold's Number Computational Aeroacoustics," presented at the First Joint CEAS/AIAA Aeroacoustics Conference, Munich, Germany, June 12-15, 1995.

[24] Pamela P. Walatka, Jean Clucas, R. Kevin McCabe, Todd Plessel, and Rick Potter, "Fast User Guide," NASA report RND-93-010, June 1993.

[25] Janet L. Ellzey, Michael R. Henneke, J. Michael Picone, Elaine S. Oran, "The interaction of a shock with a vortex: Shock distortion and the production of acoustic waves," Phys. Fluids, Vol. 1, January 1995, pp. 172-184.

Chapter 6

Conclusions

This research shows that computational methods can predict shock-generated sound. Although the direct computation of sound for realistic three-dimensional, time dependent aerodynamic flow is currently limited by computer time and memory constraints, if current advancements in computer hardware and software continue, these limitations will be removed in the near future. In the meantime, significant insight can be gained into the physics of sound generation in complicated flow fields by modeling fundamental elements of these flow fields. Understanding the sound generation is a first step towards the development of quieter aircraft, equipment and living spaces.

This research pioneers the application of a direct computational approach to the study of shock noise mechanisms. Direct simulation of sound generation in shocked flows is challenging because of the disparity in amplitudes between the acoustic waves and the shocks. These challenges are met by the implementation of a high-order accurate Essentially Non-Oscillatory (ENO) scheme which uses adaptive stenciling to maintain high-order accuracy in smooth regions of the flow

to minimize numerical dissipation of the acoustic waves while maintaining sufficient numerical dissipation at the shock for stability. Numerical issues and methods involved in the computation of flows with moving shocks are addressed at the begining of this thesis to provide motivation for the selection of the numerical scheme, the selection of the order-property of the scheme, and to provide a basis for discussion of numerical error later in the paper. A study of the economics of high-order schemes shows that the trade-off between the added cost of using higher-order algorithms depends on the level of accuracy required. An analysis performed for sound in a converging nozzle showed that for a numerical error on the order of 10^{-6}, the third-order accurate ENO scheme is the most cost-effective. Therefore, a third order ENO algorithm is used for most of the work presented here. A study of the numerical error associated with the computation of slowly moving shock waves shows that spurious numerical waves are produced downstream of the shock. The numerical error manifests itself primarily in entropy, and is a function of the algorithm used in the computation and the shock speed relative to the grid. As the shock speed relative to the grid increases, the entropy error decreases.

This thesis presents and describes the modeling of sound generating mechanisms in a supersonic jet. Experimental evidence is presented to illustrate that shock noise contributes significantly to the sound field of a supersonic jet. Two mechanisms of sound generation by shocked flows are investigated: shock motion and shock deformation. These physical processes are modeled by the interaction of sound disturbances with shock waves, and the interaction of vortical structures with shock waves. These models are relevant to the understanding of shock noise because they permit the consideration of shock oscillation and shock deformation in the

development of sound.

Shock motion is modeled by the interaction of a sound wave with a shock. Analysis of shock motion using Lighthill's equation shows that monopole, dipole, and quadrupole terms all have potential to contribute to the far field sound. At low supersonic Mach numbers, the monopole term dominates, followed by the dipole. The dipole term is highly directional.

Shock motion is modeled numerically by the interaction of a sound wave with a shock. During the interaction, the shock wave begins to move and the sound pressure is amplified as the wave passes through the shock. Computations of sound waves interacting with shocks in a converging diverging nozzle are performed. The results show that the amplitude of the transmitted pressure perturbation is greater than the incident pressure perturbation for all Mach numbers greater than one. The numerical approach is validated by comparison of the computed ratio of transmitted to incident sound pressures with linear theory. The comparison is good over the range of shock Mach numbers studied ($1.3 < M < 2.6$). An energy analysis is performed to determine if acoustic energy is generated in the sound-shock interaction. The analysis is based on an exact representation of the transport of energy in an arbitrary flow field, and shows that acoustic energy is indeed generated during the sound-shock interaction. The source term of this energy is shown to be confined to a region along the shock wave in space-time, and is a function of the changes in entropy, momentum, and temperature from the mean flow state.

Shock deformation is investigated by the simulation of a ring vortex interacting with a shock wave. This model has practical significance because it models the pas-

sage of a turbulent structure through a shock wave. Observations of the evolution of perturbations in pressure, density, entropy, vorticity and velocity downstream of the shock lead to the conclusion that acoustic waves and contact surfaces are generated by the interaction. That these two types of fluid structures are generated by the interaction is validated by experimental evidence. The structure of the contact surfaces is related to the shock dynamics. The contact surfaces are observed to be generated by disturbances which are initiated during the interaction and travel along the shock both towards and away from the center of the vortex ring. The motion and deformation of the shock generates entropy and vorticity, respectively.

Analysis of the numerical results demonstrates that the sound wave which results from the interaction of a vortex ring with a shock wave spreads cylindrically. This is due primarily to the presence of the shock wave which acts as a barrier to sound traveling upstream. Analysis of the sound intensity level over the region of the computation provides insight into the directivity of the sound. High intensity levels are seen along the shock wave and at angles of approximately 50 and -55 degrees from a horizontal axis through the vortex filament when the upstream Mach number is 1.5. The peak sound amplitude generated by a a clockwise rotating vortex was found to be as much as 156 percent higher than sound generated by the interaction of a counter-clockwise rotating vortex and shock wave. A significant result of this work is that the sound pressure level is shown to increase with shock strength. The relationship between the sound pressure level (SPL) and shock strength, defined by the parameter $\beta = \sqrt{M^2 - 1}$, is shown to be approximately $SPL \propto \beta^4$. This is consistent with experimental observations of shock noise in supersonic jets, and implies that the interaction of a vortex ring with a shock wave

is a dominant physical process in the physics of shock noise generation.

Appendix A

Derivation of Unsteady Shock Jump Relations

In this appendix, the shock jump relations for a moving shock are derived by using generalized functions. The results obtained here for the continuity and momentum equations are also provided in [1]. However, a derivation of the unsteady shock jump relation for the energy is not provided in [1].

It is important to begin by introducing the concept of a generalized function. Generalized functions will not be defined in a rigorous mathematical context here (see [1] and its references for details), but will be presented to show the connection between generalized and ordinary functions for clarity.

Conventionally, a function is defined as a table of ordered pairs $(x, f(x))$, where for each x, $f(x)$ is unique. This table may have an infinite number of ordered pairs. In an analogous fashion, in generalized function theory, the function $f(x)$ is defined by its action on a given space of ordinary functions called test function space:

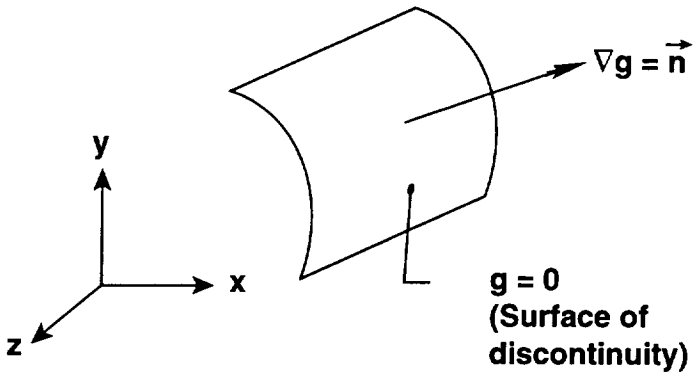

Figure A.1: Schematic of a discontinuous surface.

$$F[\phi] = \int_{-\infty}^{\infty} f(x)\phi(x)dx \tag{A.1}$$

where the function $\phi(x)$ is a test function which must satisfy certain properties given in [1]. The mapping described by Eqn. A.1 is called a functional. The function f is now identified by the new table $F[\phi], \phi \in$ test function space.

It can be shown that there are an infinite number of functions ϕ which satisfy the conditions prescribed on the space of test functions, so the table produced by Eqn. A.1 has an uncountably infinite number of elements. The space of test functions is so large that the functionals on this space generated by Eqn. A.1 contain not only ordinary functions, but additional functions. Thus, ordinary functions are a subset of the generalized functions. It can be shown from classical Lebesque integration theory that the Dirac delta function cannot be an ordinary function [1]. However, functions such as the Dirac function are included in the definition of generalized functions. Now that the concept of function space has been extended to include functions such as the Dirac delta, the extension of the definition of derivative is presented.

Let $f(x, y, z)$ be a piecewise smooth function with one surface of discontinuity. Denote this surface by $g = 0$. Such a surface is illustrated in Figure A.1. At this surface of discontinuity, there is a jump in the value of the function denoted by

$$\Delta f = f(g = 0^+) - f(g = 0^-) \tag{A.2}$$

Note that $g = 0^+$ is on the side of the surface into which ∇g points and that, following Farassat, $\nabla g = \vec{n}$.

The generalized divergence of a vector f, $\bar{\nabla} \cdot \vec{f}$, is related to the ordinary divergence, $\nabla \cdot \vec{f}$, and the jump across the surface normal, $\Delta \vec{f}$, by:

$$\begin{aligned} \bar{\nabla} \cdot \vec{f} &= \nabla \cdot \vec{f} + \nabla g \cdot \Delta \vec{f} \delta(g) \\ &= \nabla \cdot \vec{f} + \vec{n} \cdot \Delta \vec{f} \delta(g) \end{aligned} \tag{A.3}$$

The shock jump relations for a flow in which a discontinuity in the flow is moving may be derived by using the definition provided by Eqn. A.3, because the differential forms of the laws governing the conservation of mass, momentum, and energy are valid even when discontinuites exist within the region, as long as the derivatives are interpreted as generalized derivatives. The application of generalized derivatives to the conservation laws is most readily performed when the equations are in divergence form. Begin by considering the conservation of mass.

$$\frac{\bar{\partial} \rho}{\partial t} + \bar{\nabla} \cdot (\rho \vec{u}) = 0 \tag{A.4}$$

Applying the definition of the generalized derivative, Eqn. A.3,

$$\frac{\partial \rho}{\partial t} + \Delta[\rho]\frac{\partial g}{\partial t} + \nabla \cdot (\rho \vec{u}) + \Delta[\rho \vec{u}] \cdot \vec{n}\delta(g) = 0 \qquad \text{(A.5)}$$

The sum of the first and third terms define the ordinary continuity equation, thus this sum is zero. The term $\frac{\partial g}{\partial t}$ is equal to the negative of the velocity of the surface, $-v_n$.

Thus,

$$\Delta[\rho(u_n - v_n)] = 0 \qquad \text{(A.6)}$$

where $u_n = \vec{u} \cdot \vec{n}$ is the component of velocity normal to the surface g, and v_n is the velocity of the surface. If the states upstream and downstream of a shock are denoted by the subscripts of 1 and 2, respectively, and the shock is not moving, note that Eqn. A.6 reduces to the familar Rankine-Hugoniot relation for steady flows in one dimension: $\rho_2 u_2 = \rho_1 u_1$.

Consider now the conservation of momentum:

$$\frac{\bar{\partial}(\rho u_i)}{\partial t} + \frac{\bar{\partial}(\rho u_i u_j)}{\partial x_j} + \frac{\bar{\partial} p}{\partial x_i} = 0 \qquad \text{(A.7)}$$

Applying the definition of generalized derivatives,

$$\frac{\partial(\rho u_i)}{\partial t} + \frac{\partial(\rho u_i u_j)}{\partial x_j} + \frac{\partial p}{\partial x_i} + \left[\Delta(\rho u_i)\frac{\partial g}{\partial t} + \Delta \rho u_i u_j \frac{\partial g}{\partial x_j} + \Delta p \frac{\partial g}{\partial x_i}\right]\delta(g) = 0 \qquad \text{(A.8)}$$

But, since $\frac{\partial g}{\partial t} = -v_n$ and $\frac{\partial g}{\partial x_j} = n_j$, and noting that the sum of the first three terms is equivalent to the well known momentum equation for continuous flows, Eqn. A.8 reduces to:

$$\Delta[\rho u_i(u_n - v_n) + p n_i] = 0 \qquad \text{(A.9)}$$

It is again comforting to note that when the shock is not moving, this equation reduces to the familar Rankine-Hugoniot relation for steady, one-dimensional flow: $\rho_2 u_2^2 + p_2 = \rho_1 u_1^2 + p_1$.

Consider now the energy equation:

$$\frac{\bar{\partial} e}{\partial t} + \frac{\bar{\partial}(e+p)u_i}{\partial x_i} = 0 \tag{A.10}$$

where e is the total energy: $e = \rho h + \frac{1}{2}\rho u^2 - p = \rho H - p$. The total specific enthalpy is represented by the symbol H. Applying the definition of the generalized derivative,

$$\frac{\partial e}{\partial t} + \frac{\partial(e+p)u_i}{\partial x_i} + \left(\Delta[e]\frac{\partial g}{\partial t} + \Delta[(e+p)u_i]\frac{\partial g}{\partial x_i})\right)\delta(g) = 0 \tag{A.11}$$

Making the simplifications similar to those made for the continuity and momentum equations,

$$-\Delta[e]v_n + \Delta[(e+p)u_n] = 0 \tag{A.12}$$

$$-\Delta[\rho h + \frac{1}{2}\rho u^2 - p]v_n + \Delta[(\rho h + \frac{1}{2}\rho u^2)u_n] = 0 \tag{A.13}$$

$$\Delta[(\rho h + \frac{1}{2}\rho u^2)(u_n - v_n) + pv_n] = 0 \tag{A.14}$$

For steady, one-dimensional flow, Eqn. A.14 reduces to the familiar Rankine-Hugoniot relation: $h_2 + \frac{1}{2}\rho_2 u_2^2 = h_1 + \frac{1}{2}\rho_1 u_1^2$.

Bibliography

[1] Farassat, F., Lecture Notes, 1992. See also his recently published paper: "Introduction to Generalized Functions with Applications in Aerodynamics and Aeroacoustics," NASA Technical Paper 3428, 1994.

Appendix B

Equations for the Velocity and Pressure of a Ring Vortex

For the purposes of prescribing the initial condition for the numerical calculation, the vortex ring is assumed to be incompressible. The vortex moves relative to a fixed coordinate system at a velocity equal to the sum of the mean flow velocity, U, and the vortex translational velocity V. A cross-section of the vortex ring is illustrated in Figure B.1. The equations for the velocity and pressure in the fluid as a result of the presence of the vortex are derived for the purposes of prescribing an initial condition for a numerical calculation.

B.1 Velocity

B.1.1 Outside the Core

Lamb [1] provides the expression for the stream function, ψ, of a vortex ring:

$$\psi = -\frac{\Gamma r {r_0}^{1/2}}{2\pi}[(\frac{2}{K} - K)K(k) - \frac{2}{K}E(k)] \qquad \text{(B.1)}$$

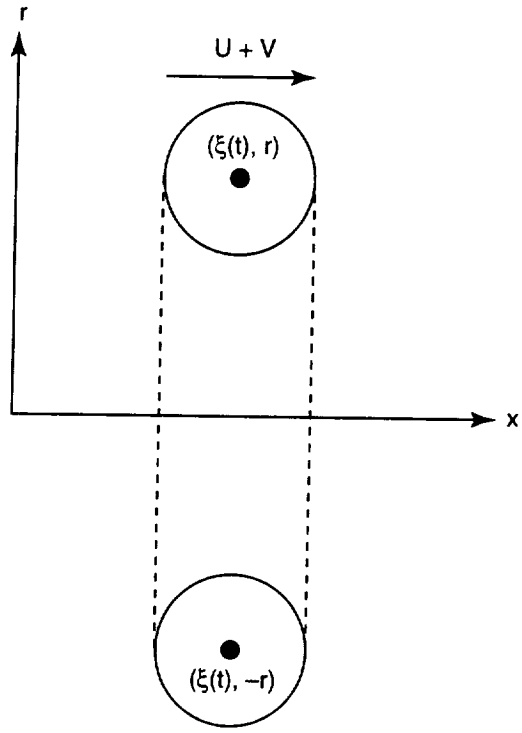

Figure B.1: Ring vortex moving at a velocity $U + V$ with respect to a fixed coordinate system (x, r).

where Γ is the circulation, r is the distance from the axis of symmetry, K and E are the complete elliptic integrals of the first and second kind,

$$K(m) = \int_0^{\frac{\pi}{2}} (1 - m \sin^2 \theta)^{-\frac{1}{2}} d\theta \tag{B.2}$$

and

$$E(m) = \int_0^{\frac{\pi}{2}} (1 - m \sin^2 \theta)^{\frac{1}{2}} d\theta, \tag{B.3}$$

and

$$k^2 = \frac{4 r r_0}{[(x - x_0)^2 + (r + r_0)^2]} \tag{B.4}$$

where r_0 and x_0 are the radial and axial positions of the vortex filament, respectively.

Given the stream function, the axial and radial velocity components, u and v , respectively, can be found:

$$u = -\frac{1}{r}\frac{\partial \psi}{\partial r} = \frac{\Gamma}{2\pi r_2}[K(k) + \frac{(r_0^2 - (x - x_0)^2 - r^2)}{r_1^2}E(k)] \tag{B.5}$$

and

$$v = \frac{1}{r}\frac{\partial \psi}{\partial x} = -\frac{\Gamma}{2\pi r_2}\frac{(x - x_0)}{r r_2}[K(k) - \frac{(r_0^2 + (x - x_0)^2 + r^2)}{r_1^2}E(k)] \tag{B.6}$$

where $r_1 = \sqrt{(r - r_0)^2 + (x - x_0)^2}$ and $r_2 = \sqrt{(r + r_0)^2 + (x - x_0)^2}$.

In the numerical implementation of these equations for the vortex velocity, the polynomial approximations to $K(k)$ and $E(k)$, which have an error bounded by 2×10^{-8} [2], are used.

B.1.2 Inside the Core

In order to avoid the mathematical singularity on the vortex filament and to better model the physics of a real, viscous vortex, the velocity distribution inside the vortex core is assumed to have a linear distribution of tangential velocity:

$$u = v_\theta \sin\theta \frac{R}{r_c} \tag{B.7}$$

and

$$v = v_\theta \cos\theta \frac{R}{r_c} \tag{B.8}$$

where v_θ is the tangential velocity at the core radius r_c and R and θ are the polar coordinates centered on the vortex filament. The tangential velocity v_θ is known by substituting $(x = x_0 + r_c, r = r_0)$ into Eqn. B.6. Note that this description of the core assumes that the core is circular. This is an approximation since the core is elliptical in shape for finit values of $\frac{r_c}{r_0}$.

B.2 Pressure

B.2.1 Outside the Core

The pressure field of this vortex is determined by momentum conservation. Consider the momentum equation for an irrotational flow:

$$-\frac{1}{\rho}\nabla p = \nabla\frac{q^2}{2} + \frac{\partial\vec{u}}{\partial t} \tag{B.9}$$

where p is pressure, q is the magnitude of the velocity vector, and $\vec{u}$ is the velocity vector $\{u, v\}^T$. Now, the velocity component in the axial direction is $u = U + u_v(x - \xi(t), r)$ where U is the mean flow velocity, u_v is the perturbation velocity induced by the vortex, and the coordinate ξ is fixed on the vortex filament position. The radial component of velocity, $v = v_v(x - \xi(t), r)$, where v_v is the velocity induced by the vortex.

The flow is not steady in the fixed reference frame, because the position of the vortex varies as a function of time: $\xi = x + (U + V)t$, where V is the vortex translational velocity. Evaluating the derivative $\frac{\partial u}{\partial t}$ one obtains

$$\begin{aligned}
\frac{\partial u}{\partial t} &= \frac{\partial u_v(x - \xi(t), y)}{\partial t} \\
&= \frac{\partial u_v}{\partial(x - \xi(t))}\frac{\partial(x - \xi(t))}{\partial t} \\
&= -\frac{\partial u_v}{\partial(x - \xi)}(U + V) \\
&= -\frac{\partial u_v}{\partial x}(U + V)
\end{aligned} \tag{B.10}$$

Similarly,

$$\frac{\partial v}{\partial t} = -\frac{\partial v}{\partial x}(U + V) \tag{B.11}$$

Note that for irrotational flow, $\frac{\partial v}{\partial x} = \frac{\partial u}{\partial r}$. Therefore, $\frac{\partial v_v}{\partial x} = \frac{\partial u_v}{\partial r}$ so that

$$\frac{\partial \vec{u}}{\partial t} = -\nabla u_v (U + V) \tag{B.12}$$

If density is assumed to be constant, the momentum equation can be written:

$$\nabla[\frac{p}{\rho} + \frac{q^2}{2} - (U + V)u_v] = 0 \tag{B.13}$$

where $q^2 = u^2 + v^2 = (U + u_v)^2 + v_v^2$. Substituting in for u, v, and evaluating the integral of Equation B.13 along a stream line which terminates in the mean flow state where the velocity induced by the vortex is zero, one obtains

$$p - p_0 = -\frac{\rho_0}{2}(u_v^2 + v_v^2) + \rho_0 V u_v \tag{B.14}$$

where the subscript 0 denotes the mean flow state.

B.2.2 Inside the Core

Equation B.14 is valid for the flow outside the vortex core, where the flow is irrotational. To obtain the pressure field inside the vortex core where the flow is rotational, consider the radial momentum equation:

$$dp = \frac{\rho v_\theta^2}{r} dr \tag{B.15}$$

Substituting for v_θ and integrating from the edge of the vortex core to r,

$$p(r) = p(r_c) + \frac{\rho_0}{2}\frac{v_\theta^2}{r_c^2}(r^2 - r_c^2) \tag{B.16}$$

assuming that $\rho = \rho_0$. The pressure $p(r_c)$, determined from Eqn. B.14 to ensure continuity of pressure across the vortex core interface is:

$$p(r_c) = p_0 - \frac{\rho_0}{2} v_\theta^2 \tag{B.17}$$

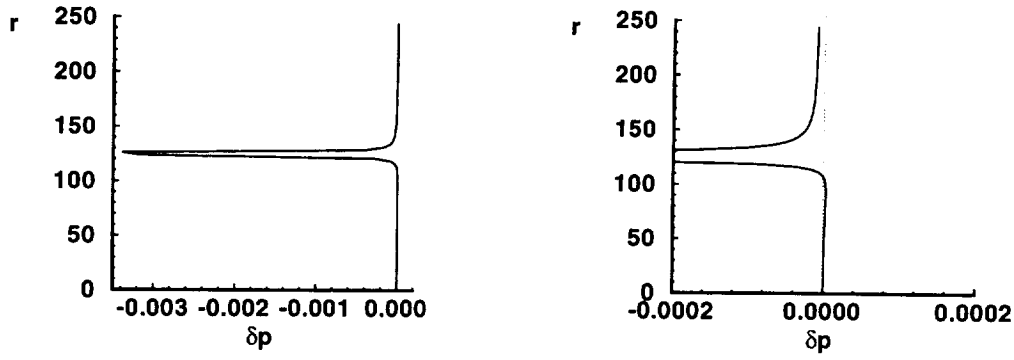

Figure B.2: Profile of the pressure distribution of a counter-clockwise rotating ring vortex of strength $\Gamma = 0.75$. The figure to the right shows the pressure distribution over a smaller range of pressure perturbation to highlight the asymmetry in the pressure profile above and below the filament.

The pressure profile of a counterclockwise vortex of strength $\Gamma = 0.75$ is provided in Figure B.2. Note the asymmetry in the pressure field relative to the vortex filament and the region of slightly positive pressure below the filament.

In the implementation of the vortex ring as an initial condition, the flow quantites are normalized with respect to the upstream static pressure and density, and the vortex core radius.

B.3 Remarks

Note that although the pressure and velocity are defined to be continuous at the rim of the vortex core, the derivatives of these quantities are not. Because the natural dissipation in the algorithm will automatically smooth these derivatives at the rim, discontinuities in derivatives at the rim are not a problem with this algorithm. Less robust schemes may have difficulty with this initial condition.

Bibliography

[1] Sir Horace Lamb, Hydrodynamics, Cambridge University Press, 1932, p. 237, 246.

[2] Milton Abramowitz and Irene S. Stegun, eds., Handbook of Mathematical Functions, 9^{th} printing, Dover Publications, Inc. , New York, pp.591-592, Eqns. 17.3.36 & 17.3.34, 1970.

End

Date

June 22, 1995